Three-dimensional calculation of non-uniform structures in low-density nuclear matter and neutron star by a relativistic mean field model

Minoru Okamoto

February 2014

Three-dimensional calculation of non-uniform structures in low-density nuclear matter and neutron star by a relativistic mean field model

Minoru Okamoto
Doctral Program in Physics

Submitted to the Graduate School of
Pure and Applied Sciences
in Partial Fulfillment of the Requirements
for the Degree of Doctor of Philosophy in
Science

at the
University of Tsukuba

Abstract

In low-density nuclear matter which is relevant to the crust region of neutron stars and collapsing stage of supernovae, non-uniform structures called "nuclear pasta" are expected. Such pasta structures may play important roles for, e.g. neutrino opacity during supernovae, cooling process of neutron stars and mechanical strength of the crust, etc besides the equation of state (EOS). So far, most works on nuclear pasta have used Wigner-Seitz cell approximation which assumes a geometrical symmetry of structures. But this brings about a strong constraint that uniform matter or typical pasta structures, i.e. droplet, rod, slab, tube, and bubble are the ground states of low-density nuclear matter. To investigate these structures without any assumption on the geometry, we performed three-dimensional calculation with a relativistic mean field model. This model with fields of mesons and baryons introduced in a Lorentz-invariant way is rather simple for numerical calculations, but realistic enough to reproduce the bulk properties of nuclear matter.

First, we explored the nuclear matter with fixed proton number-fraction $Y_p = 0.5$, 0.3 and 0.1. We have observed the typical nuclear pasta for all of three proton number-fraction case: with increase of density the favorable structure changes from nuclear droplet, rod, slab, tube, and to bubble. Near the saturation density $\rho_{\rm B} \approx \rho_0$, nuclear pasta dissolved to uniform matter. The appearance of the pasta structures lowers the energy, while the energy differences between various geometrical structures are very small. By the appearance of such non-uniform structure, the EOS of the system becomes significantly soft. In the case of $Y_p = 0.5$, the system sometimes settled on the local minimum on the way of searching for the ground state structure. In these points, some exotic structures appeared. Assuming the electron density distribution is uniform, we explore the charge screening effect of electron. Two type EOS as a whole show almost no dependence on the treatments of Coulomb interaction.

Secondly, we extended our calculations to cold catalyzed matter which corresponds to the neutron-star crust. In this case, with and increase of density, which ranges from well below to half of the normal nuclear density, we have observed that the ground state of matter shows two types of pasta structures, droplets and rods. For the crystalline configuration of droplets, near the transition density to rod, the fcc lattice is more favorable than the bcc lattice, which is different from the results of previous studies. We have discussed some reasons for the difference, but more elaborate studies are needed to clarify it. We found that the ground state of low-density nuclear matter changes its crystalline configuration from a bcc to an fcc lattice near half the normal nuclear density within the this model. This conclusion arises from including the smooth surface of nuclei and a self-consistent calculation of the Coulomb interaction.

For the effective utilization of three-dimensional data of catalyzed nuclear matter, we estimated realistic shear modulus of neutron star crust. To treat the deformation in the system with periodicity, we introduced "deformed" periodic boundary condition. To estimate the shear modulus, we performed two type calculations: semi-full calculation and full-calculation. In semi-full calculations, the shear modulus in low-density region $\rho_{\rm B} < 0.03{\rm fm}^{-3}$ is about 0.09 in the unit of Coulomb parameter. This value is reduced about 22% from the previous study. For the density region of $\rho_{\rm B} > 0.03{\rm fm}^{-3}$, we could not estimate the shear moduli

in the unit of Coulomb parameter with one coefficient parameter due to the finite volume of nuclei. In full calculations, while the density distribution of proton and neutron is modified in deformed boundary condition, the shapes of nuclei is mostly conserved. Then, the shear modulus of Coulomb part can be estimated in the unit of Coulomb parameter with one coefficient parameter. However, to conserve the beta-equilibrium, the additional effects of nuclear matter appear such as the change of proton fraction. Therefore, the shear modulus derived from the total energy could not be evaluate with the unit of Coulomb parameter in all density range of $\rho_{\rm B} > 0.03{\rm fm}^{-3}$ and slightly larger than that of Coulomb part.

The reappearances of "pasta" in high density region of neutron star have been expected after the disappearance in low-density region, such as "kaonic pasta" and "quark pasta". As an example, we explored the "kaonic pasta" structures in high density nuclear matter. Searching for the density region of $3 \sim 5\rho_0$, we obtained the "kaonic pasta" structures in $0.41 - 0.785$ fm^{-3}. As with low-density nuclear matter, with increase of density the favorable structure changes from droplet, rod, slab, tube, and to bubble. The appearance of "kaonic pasta" structures lowers the energy, while the energy differences between various geometrical structures are small.

Contents

Chapter 1

Introduction

In our daily lives, specific properties of nuclei in atoms are hidden and do not appear. In high density astronomical object such as neutron stars, however, they become important keys to understand these objects. Generally, the central densities of normal nuclei and the proton fraction are approximately constant regardless of the species. Namely, they are composed of almost the same number of proton and neutron and have the density which is around $\rho_0 \approx 0.16$ fm^{-3}, Since a nucleus is a system of fermions and the masses and potentials of proton and neutron are almost the same, the chemical potentials of both components reach equilibrium at the same density $\rho = \rho_0$, where nuclei have a minimal energy. All the basic features of normal nuclei we know is expressed as above.

In this chapter, first, we briefly review the characteristic of nuclei and nuclear matter. Secondly, the specific feature of neutron star is described. The recent problem in the observation of neutron star and the main theme of non-uniform structure in low-density nuclear matter called "pasta" structure is introduced and the brief review of study in neutron star crust related with low-density nuclear matter is also described. Then, the main purpose of this thesis is explained.

1.1 Properties of Nuclear Matter

In general, the infinite matter is an idealazation. To research its property, we have extrapolated from the finite system composed by the considerated infinite system. Accordingly, the properties of symmetryc nuclear matter are obtained by extrapolation of those of finite nuclei and discarding the Coulomb energy. The history of the notion goes back to Weizsacker and the liquid drop model of the nucleus. Here, we would refer only the ideas of the model, in which they seeks to characterize the energy of a nucelus by its atomic and proton numbers A and Z

The basic properties of nuclei or nuclear matter is that they are saturated systems. This property is derived from the short range part of the nuclear force, its strong repulsion at s short distance, and the Pauli principle [1–3]. In this situation, the central density of nuclei remains constant even if more nucleons are added to nuclei. Then, from this property, we could derive the relation between nuclear radius and atomic number as $R = r_0 A^{1/3}$ where $r_0 =$ constant and treat the energy density as approximately constant. Consequently, the volume energy of

a nucleus is described as $\epsilon_0 \times V$, where ϵ_0 is the energy density of symmetric nuclear matter at ρ_0 and V is the volume of the nucleus. The balance between Fermi energies of protons and neutrons, together with the symmetry potential, makes nuclei with $N \approx Z$ more tightly bound than others. This should be modified by the existence of the Coulomb repulsion which shifts the region of stable nuclei with large A to the region with a greater neutron fraction $(A - Z)/Z = N/Z$. The Coulomb energy would be proportional to square of the proton number and inverse of the radius. In addition to the above volume contributions, the surface energy arises because nucleons at the surface feel less attraction than inner nucleons. Surface energy would be proportional to the surface area.

From these considerations, the total mass of a nucleon could be described as

$$M(A,Z) = A\left[\frac{4}{3}\pi r_0^3\epsilon_0 + a_{\rm sym}\left(\frac{n-Z}{A}\right)^2\right] + 4\pi r_0^2 A^{2/3}\epsilon_{\rm surf} + \frac{3}{5}\frac{(Ze)^2}{r_0 A^{1/3}} \tag{1.1}$$

This formula is often refereed to as the Bethe-Weizsäcker's semi-empirical mass formula or the droplet model of nuclear masses. The total binding energy B is given by subtracting $(A - Z)m_n + Zm_p$ from Ep.([**?**]). For more precise consideration, many additional effects with unknown coefficients should be taken into account. It has been considered that these effects are contained by the fitted parameters in the more general formula to thousands of nuclear mass data [4]. We need not to dwell on this. In this formula, the remarkable point is that the binding energy per nucleon B/A is described as power series of $1/A$ with zeroth power. Therefore, in the large limit of A, only the volume term remains. Accordingly, the binding energy per nucleon of infinite, symmetric, nuclear matter could be obtained as

$$B/A \approx -16\text{MeV}. \tag{1.2}$$

From the relation between the nuclear radius and its atomic number, the nuclear radius parameter would be $r_0 = 1.16$ fm. This parameter is also obtained by an analysis of electron-nucleus scattering in terms of density distributions [5]. The saturated nuclear number density is related to r_0 by $\rho_0 = \left[(4\pi/3)r_0^3\right]^{-1}$=0.153 fm^{-3}. A condition equivalent to determining the saturation density is determining the Fermi momentum common to neutrons and protons in symmetric matter at saturation. Density and Fermi momentum are related by $\rho_0 = \frac{2k_F^3}{3\pi^2}$. Then, we obtain k_F=1.31 fm^{-1}. In terms of an equation of state (EOS), $\epsilon(\rho)$, the binding energy per nucleon B/A of nuclear matter at the ground state is expressed by baryon number density at saturation (saturation density) ρ_0 and the energy density ϵ at the saturation density as $B/A = \epsilon_0/\rho_0 - m$, where the subscript "0" denotes the values at the saturation density of nuclear matter and m = 938.93 MeV = 4.7582 fm^{-1} is the average of the neutron and proton masses. Thus, we obtain that the energy density at saturation: $\epsilon_0 = 141\text{MeV/fm}^3$. The binding energy per nucleon and nucleon number density at saturation will serve to fix two coupling constants of the theory. Any theoretical model of nuclear matter is required to fulfil the above conditions.

Stars must be electrically neutral. So there are electrons/muons as much as protons. Since electron is much lighter than nucleons, proton-fraction Y_p, i.e., lepton-fraction Y_l dependence of the electron kinetic energy is steep, while that of the nucleon energy is moderate. Therefore the total energy has a minimum at a small value of Y_p. In other words, neutral nuclear

matter with electron is highly isospin-asymmetric. On the other hand, the short-range nuclear force together with the Fermi energies of the protons and neutrons energetically prefer isopsin symmetric configurations. So the constraint of charge neutrality exacts the price of a high isospin energy. Theoretical model of nuclear matter should correctly reflect the isospin symmetry energy. From Eq.(1.1), the symmetry energy coefficient is related to the EOS $\epsilon(\rho)$ by

$$a_{\rm sym} = \frac{1}{2}\left(\frac{\partial^2(\epsilon/\rho)}{\partial t^2}\right)_{t=0}, \quad t \equiv \frac{\rho_n - \rho_p}{\rho}. \tag{1.3}$$

To evaluate these expressions, the energy density and number density must be expressed in terms of the neutron and proton Fermi momenta k_n and k_p. After evaluation of the above expression, they are then set equal to the common value k_F of symmetric matter.

The compression modulus K, which defines the curvature of the EOS of symmetric nuclear matter $\epsilon(\rho)/\rho$ at ρ_0, is another important physical ingredient. This modulus is often refereed to as incompressibility of nuclear matter. It reflects the high-density behavior of the EOS though not uniquely. The larger K is, the more steeply the pressure increases with density. This high-density behavior is generally referred to as the "stiffness" or "softness" of the EOS. The stiffness will directly influence the maximum mass of the neutron star sequence belonging to the EOS. Its value enters into analyses of astrophysical phenomena as well as of low- and high-energy heavy-ion reactions.

The compression modulus at saturation also appear in the mass formula, however, the dependence is rather weak. Since we cannot directly create and probe nuclear matter in ordinary laboratories, the only way to extract a value for K is by making contact with the phenomenology of the compressional modes in finite nuclei. The clearest example of compressional mode is the Isoscalar Giant Monopole Resonance (ISGMR), which is often called the nuclear "breathing mode", though its extraction from experiment contains ambiguities. J. P. Blaizot showed that a plausible definition of the finite nucleus incompressibility K_A is given by

$$E_{\rm ISGMR} = \sqrt{\frac{\hbar K_A}{m\left\langle r^2\right\rangle}}, \tag{1.4}$$

where $E_{\rm ISGMR}$ is single peak of excitation energy, m the nucleon mass, and $\left\langle r^2\right\rangle$ the mean square nuclear radius in graund state. Incompressivility K is included in the Weiszäcker-type formula for K_A,

$$K_A = K + K_{surf}A^{-1/3} + K_{sym}\alpha^2 + K_{Coul}\frac{Z^2}{A^{4/3}}, \tag{1.5}$$

where $\alpha = (N-Z)/A$. By fitting the experimental data, the compression modulus likely lies in the range 200 to 280 MeV [6–10]. The compression modulus is related to the EOS through

$$K = \left[k^2\frac{d^2}{dk^2}\left(\frac{\epsilon}{\rho}\right)_{k_F}\right] = 9\left[\rho^2\frac{d^2}{d\rho^2}\left(\frac{\epsilon}{\rho}\right)\right]. \tag{1.6}$$

Finally, the nucleon effective mass in matter is also relevant. It plays a role somewhat similar to the compression modulus as regards the high-density behavior of the EOS. This is so because the EOS contains, among other terms, a sum of $[k^2 + m^{*2}(k_f)]^{1/2}$ over those nucleon momentum states that lie below the Fermi momentum k_f as the considered density.

The quantity $m^*(k_f)$ is the effective nucleon mass in the medium and it depends on the Fermi momentum. Therefore, the above mentioned sum will clearly influence the "stiffness" of the EOS and hence, as with K, will have a direct bearing on the maximum mass that the EOS can support against gravity.

The effective mass at saturation density is not known precisely. According to the particular type of data and its analysis, the effective mass is defined in various ways. The value of the isoscalar component of the mean field can be derived from a non-relativistic analysis of scattering of neutrons from lead nuclei and is found to lie in the range $m_S^*/m = 0.74$ – 0.82. This is not the "Dirac effective mass" which appears in nuclear filed theory. It can be identified approximately as the Landau effective mass [9, 11] which in turn is related to the Dirac effective mass of nuclear field theory through

$$m_S^* \sim m_L^* = \left(\frac{k}{\partial \epsilon(k)/\partial k} \right)_{k_F} = \left(m^{*2} + k_F^2 \right)^{\frac{1}{2}} \tag{1.7}$$

where $m^* \equiv m^*(k_F)$ is the nucleon effective mass m^* at saturation density and k_F is the corresponding Fermi momentum. Consequently, the range expected for the Dirac effective mass at saturation density is $m^*/m \sim 0.7$ – 0.8.

1.2 Neutron stars

Neutron stars are highly compacted astral objects which are produced in supernova explosions, the resultant in the evolution of further massive stars. The mass of neutron star M is detected about $1 - 2 \times M_\odot$ where $M_\odot$ is the mass of the sun, while the radii of them are around 10-12km [12]. The matter they mainly contain neutrons is thus the densest one found in the universe to date. The average interior density is greater than that in an atomic nucleus ρ_0. As comparison, white dwarf stars have radii of several 10^3 kilometers, and the density in central region is in the range of $10^{-9} - 10^{-5}\rho_0$ whereas they have the slimier masses with neutron stars. Against collapse of gravitation, supporting in a neutron star is provided by the Fermi pressures of the neutrons and other components in the interior, in the same way that white dwarfs are supported by degenerated electron pressure. On the other hands, ordinary stars are supported by only thermal gas pressure.

1.2.1 Discovery and theory

The first suggestion of neutron stars is done by Baade and Zwicky in 1934 [13, 14], and considerable theoretical work about their properties was carried out prior to their actual observation, beginning with theoretical framework by Oppenheimer and Volkoff in 1939 [15]. It was only when the discovery by Bell and Hewish of radio pulsars in 1967 [16]. Radio pulsars are the stars whose radio emission appears to turn on and off and are identified as rotating neutron stars by Gold [17]. Then, the existence of neutron stars was established. Since then, neutron stars have become large laboratories for proving the fundamental physics such as relativistic theories of gravity and the properties of matter at extreme conditions. Neutron stars play an important role in astrophysics as the wide range of energetic compact sources from radio, X-ray, to gamma-ray [18,19]. The power of radio pulsar is rotation. Radio pulsars

are found in both isolated and binary star systems and observed by the emission of radiation in all frequencies from radio to gamma rays. Neutron stars are also found in the system of luminous X-ray binaries in which they accrete the atmospheric matter with each other star. About 1600 neutron stars until now have been detected as radio pulsars. Among them, about 125 ones are specified as millisecond pulsars whose rotation period is 1 – 10 milli-second. In X-ray binary system, about 250 neutron stars have been detected as accretion powered ones. About 50 of them are X-ray pulsars and almost same number produce intense X-ray bursts powered by thermonuclear flashes [20].

The energy source of neutron stars is their huge gravitation which is several 10 times as intensive as thermonuclear burning. The gravitational acceleration at the surface is about 10^{11} times that on Earth because of the compactness and high-density. The gravitational binding energy of a matter with mass m at the surface is about tenth part of mc^2. As comparison, binding energies of nuclei are about 1% of the rest energy of matter. In X-ray binary systems, the energy emitted from neutron stars largely are derived from the gravitational energy released by accreted matter from their companion star. Under the gravitational core collapses in supernova to form a neutron star, conservation of angular momentum requires that its rotation rate and rotational energy increase. Then, the source of the kinetic energy in rotation of the neutron star also are derived from the release of gravitational binding energy. Other neutron stars gradually release gravitational energy stored as magnetic and thermal energy.

Neutron stars are characterized by strong magnetization, with magnetic fields in surface ranging from 10^6G to 10^{15}G [21]. In comparison, the strongest power of magnetic field produced in the laboratory on the Earth is about 10^3G. The slowing down of rotation in pulsar implies magnetic fields of order 10^{11}G to 10^{15}G [22, 23]. The rapid rotation within such extreme condition is important in generating relativistic particles and radio emission. Accretion of plasma onto neutron stars in X-ray binary systems is connected with the magnetic poles by fields ranging from 10^8 to 10^{13}G.

The temperature in the inner core of proto-neutron stars is about 10^{11}K, and neutrino emission cools them to less than 10^{10}K until the first few days [24, 25]. Throughout most of its early life, the interior temperature is in the range $10^8 - 10^9$K and the surface temperature is tenth part of or less of the temperature of inner core. The hot surface typically radiates X-rays. X-ray satellites have detected X-ray emission from stars in the process of cooling but the process of emission and the size and structure of the emitting regions are not so far sufficiently comprehended to figure out accurately the surface temperatures and radii of neutron stars from these measurements.

The matters of the interior region in neutron stars have relatively low-temperature compared with their characteristical microscopic energies of excitation in the order of MeV. Moreover, r-processes in the early stage of proto-neutron stars remarkably rapidly come about compared with the cooling process of the stars that their components turn out to be the lowest states through the strong, electromagnetic and weak interactions.

1.2.2 Internal structure

In general, with increasing depth in the star, the density of matter increases. The atmosphere is compressed by gravity to less than 1cm height. Below the atmosphere is a crust region with typically ∼1km thickness, consisting of lattice of bare nuclei immersed in the sea of

degenerated electrons. The matter in the outer region of the crust is expected to be largely composed by Fe which is the termination of thermonuclear burning processes in star. With increasing the density, the Fermi energy of degenerated electron rises. Around the density 8×10^6g cm^{-3}, the energy of electron become high about 1Mev to be captured by Fe. This capture process make protons in nuclei neutrons via the weak interaction $e^- + p \rightarrow n + \nu$, which occurs in supernova for the formation of neutron star. The produced neutrino ν escapes from the proto-neutron star, which make the energy of the system lower state. With increasing density, the composition of matter becomes more neutron rich and rearranges into lattice of more and more neutron-rich nuclei. Finally, the nuclei reach such as Kr at the density $\rho_{\rm drip} = 4 \times 10^{11}$g cm^{-3} which called the neutron drip point. Since the electron would have to go into an already occupied state, the nuclei constituting the inner region of crust which might be unstable in the laboratory can not undergo beta decay via the inverse reaction $n \rightarrow p + e^- + \mu$ because of the Pauli exclusion principle. Beyond this density region, the matter becomes highly neutron rich as well as not all the neutrons can surround the nuclei and the space region becomes permeated by the sea of dripped neutrons besides the sea of electrons. Then, around the density $\sim \rho_0/2$, spherical nuclei become unstable and the structure of matter change through a sequence of rather unusual structures which are called "pasta" nuclei with the nuclei first becoming rod-like, slab, tube, and bubble with dripped neutrons filling the all space. Outstandingly, it is suggested that over half of the matter in the crust is in the form of these "pasta" structures [26]. Finally, at a density of about $\sim 0.6 - 1.0\rho_0$, the matter dissolves into a uniform liquid which are largely composed by neutrons with a few percent proton and electrons in the same ratio. The neutrons might be probably superfluid and the protons superconducting state.

The states of matter in the interior region of neutron star where is highly pressured are not well comprehended. With increasing density, heavier baryons could be stable. Several interesting phenomena might occur. One of them is that π-mesons are spontaneously produced and form Bose-Einstein condensed state with superfluid [27]. The matter may raise the analogous phenomena of kaon condensation. Such condensations cause the considerable enhancement of cooling process of neutron stars by neutrino emission [28–30]. At extremely high densities region of $> 4\rho_0$, where the nucleons are overlapping, it is expected that the dissolve of nuclear matter into quark matter in which the quarks become free to run. Quark matter most likely appears as droplets in the sea of nuclear matter at densities of order $4 - 5\rho_0$. A core of bulk quark matter, which would be present at higher densities, would also enhance neutron star cooling, but whether the transition to bulk quark matter is actually reached in neutron stars remains uncertain [31–34].

The structure of neutron stars, including their radii as a function of mass, and the range of masses for which they are stable, is determined by the equation of state of the matter they contain. A knowledge of the maximum mass $M_{\rm max}$ that a neutron star can have is important in distinguishing possible black holes from neutron stars by observations of their masses. The uncertainty in the present theoretical limit, $M_{\rm max} \sim 2.5 M_\odot$, calculated on the basis of physically plausible equations of state, reflects the uncertainty of the properties of matter at densities much greater than ρ_0.

1.2.3 "Pastas" in neutron star

As mentioned in previous subsection, the outer region of neutron star crust is composed of neutron-rich nuclei immersed in the sea of dripped neutron and degenerated electrons. With increasing the density, the larger volume of nuclei are, the more unstable nuclei are. In vacuum, the fission condition of isolated spherical nucleus is comprehended as Bohr-Wheeler condition [35]

$$E_{\rm Coul}^{(0)} < 2E_{\rm surf}^{(0)}, \tag{1.8}$$

where $E_{\rm Coul}^{(0)}$ and $E_{\rm surf}^{(0)}$ are the Coulomb and surface energies of the nucleus, respectively. The superscript (0) means that the situation is set in vacuum. This condition means that a spherical nucleus will become unstable to small quadupolar distortions if the Coulomb energy as repulsion force exceeds twice the surface energy as the force to glue together. According to this condition, nuclei become unstable to fission when the radius of a nucleus is roughly one half of the radius of a sphere whose volume is the average volume per nucleus. Then, if the the volume fraction of nuclei w is larger then one-eighth, the nuclei would be unstable [36]. Basically taking into account this fission instability, Baym, Bethe and Pethick [37] predicted that as the volume fraction exceeds 1/2, the crust will be formed of the spherical cavity in uniform nuclear matter. This model is called as "BBP" model. Although, in this model, the treatment of fission go from one extreme as nuclei to another as bubbles, for the simplicity, "BBP" is recently applied to the simulation nucleosynthesis in supernova [38]

Major change was brought by Ravenhall *et al.* in 1983 [26]. Ravenhall *et al.* have taken into account not only the three-dimensional structures such as nuclei and spherical cavity but also those of one and two dimensional ones. Specific feature in their study is the introduction of a dimensionality d. They searched for the parameters which give a minimum free energy, applying the average density and number-fraction of proton. With increasing the average density, the structure of nucleus changes from droplet to rod, slab, tube, bubble, and finally uniform. After that, this series of structures was called "pasta" structures shown in Fig.1.1. In the next year, Hashimoto *et al.*explored the "pasta" structures using liquid drop model with Wigner-Seitz approximation [39]. Then, they showed the same transition way of structure in nuclear matter suggested by Ravenhall *et al.*. From these studies, the equilibrium structure of nuclear clusters in neutron star crusts is comprehended as the balance of the total Coulomb energy and the surface energy of the nuclei according to

$$E_{\rm surf} = 2E_{\rm Coul} \tag{1.9}$$

where $E_{\rm suf}$ = is the surface energy and $E_{\rm Coul}$ is the Coulomb energy in nuclear matter.

These pasta phases have been studied by various nuclear models, such as compressible liquid drop models (CLDM) [39–41], quantum molecular dynamic (QMD) simulations [42–44], Hartree-Fock calculations [45–50], Thomas-Fermi approximation [51, 52] and the relativistic mean field (RMF) model [53–56]. Although there is the model dependence on the density region where "pasta" phase appear, they all suggest the same series of structures shown in Fig. 1.1. Some models predict that the droplet remain energetically favored throughout the whole inner crust [55, 58–61]. Iida *et al.* suggested that the differential coefficient of symmetry energy at ρ_0 denoted by L is related to the existence of "pasta". The larger the value of L is given, the narrower the pasta region is. Then, if L reach to about 100 MeV,

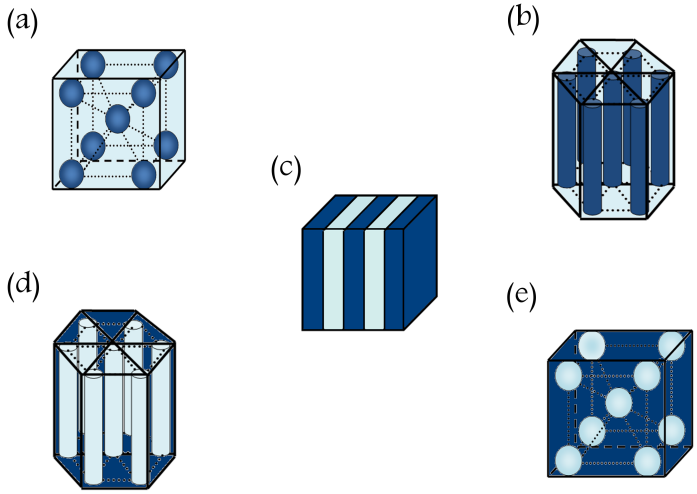

Figure 1.1: Sketch of the sequence of pasta phases in the bottom layers of ground-state crusts with an increasing nuclear volume fraction, based on the study of Oyamatsu *et al.*. (a) droplet, (b) rod, (c) slab, (d) tube, (e) bubble. Blue domains means nuclei (proton clusters) and cyan gas of nucleons.

"pasta" structure without droplet do not appear. It has also been suggested that the pinning of neutron superfluid vortexes in neutron star crusts might trigger the formation of rod-like clusters [62]. Nevertheless, the nuclear pastas may be destroyed by thermal fluctuations [42, 43, 50]. Remarkably, Watanabe *et al.* performed QMD simulations and observed the formation of rod-like and slab-like nuclei by cooling down hot uniform nuclear matter without any assumption on the geometry. They also found the appearance of intermediate sponge-like structures, which might be identified with the ordered, bi-continuous, double-diamond geometry observed in block co-polymers [63, 64].

The pasta phases appear in small range of densities near the crust-core interface with $\rho \sim 10^{14}$g cm^{-3}. However, they play the important role in the EOS of neutron star crust and carry the half of mass of crust region because of the filling up the densest region of crust [58]. The existence of nuclear pastas in hot dense matter affects the neutrino opacity, which is an important ingredient for understanding the gravitational core collapse of massive stars in supernova and the formation of neutron stars [44, 65]. As mentioned above, in the comprehension of the pulsar gliches, the dynamics of neutron superfluid vortexes is likely to be affected by the pasta phase such as the formation of rod structure. Besides, the presence of non-spherical clusters in the deep layers of the crust influences the subsequent cooling of the star, hence the thermal X-ray emission by allowing direct Urca processes [58, 66] and enhancing the heat capacity [67–69]. The elastic properties of the nuclear pastas can be calculated using the theory of liquid crystals [42, 43, 70]. The pasta phase could thus affect the elastic deformations of neutron stars, oscillations, precession and crust-quakes.

1.2.4 Purpose of the present study and outline of this paper

As mentioned above, most of the mass of neutron star concentrate around $\sim 1.4M_{\odot}$. Then, the mass of neutron star could not restrain the EOS of neutron star strongly. However, the discovery of two solar mass neutron star [71] fascinated many researchers who engage in particle, nuclear, astronomy, and recently even cold atom physics. For high compressed matter up to about 4-5 times of normal nuclear density ρ_0, many exotic phases have been speculated to exist: proton superconductivity, neutron superfluidity [27], meson condensations [30, 72–74], hyperon mixture [75–78],and quark matter [79, 80]. Existence of these phases are exactly related to the mass and radius of neutron star. The conflict of appearance of hyperon mixture and existence of two solar mass neutron star is the one of most important issues. Unfortunately, since the interactions of nucleon-hyperon, hyperon-hyeron, and three-body force among them are not exactly clarified, model dependence on the equation of state (EOS) of neutron star matter is not dispelled.

On the other hands, other problems also still remain for neutron stars. One of them is the existence of magnetars. Magnetars are thought to be neutron stars with incredibly strong magnetic fields which greatly exceed $\sim 5 \times 10^{13}$ G. In connection with strong magnetic field, soft gamma-ray repeaters are also thought to be magnetar. For several times, the gamma ray flare activities followed by long decay of much softer part than peak of flare called giant flares are observed. These flares activities are expected as starquake on neutron star crust. Recent analysis of detailed observations from several SGRs revealed that the decaying part of the spectrum exhibits a number of oscillations with frequencies in the range of a few tenths of Hz to a few hundred Hz [81, 82]. There are three events detected up to now which can be associated with crust oscillations of magnetars. The first event was detected already in 1979 from the source SGR 0526.66, the second in 1998 from SGR 1900+14, while the third and most energetic one was observed in December 2004 from the source SGR 1802.20. Analysis of the tail oscillations of SGR 1806.20 revealed the presence of oscillations at approximately 18, 26, 29, 92.5, 150, 626.5 and 1837 Hz, for SGR 1900+14 the detected frequencies were 28, 54, 84 and 155 Hz, while for the case of SGR 0526.66 there was only one frequency identified at 43.5 Hz. These oscillations are called quasi-periodic oscillations (QPOs). The QPOs are believed as the outcomes of the neutron star torsional oscillations which is easy to excite and strongly coupled to the external magnetosphere [83]. Then, the observations of QPOs in SGRs could be first evidences to detect the neutron star oscillations directly and detailed information on neutron-star crust can be extracted. To investigate the QPOs as torsional oscillation of neutron star crust, the physical input is needed. That is shear modulus. In present comprehension, the value of shear modulus is described as follow:

$$\mu = 0.118 \times \frac{n\,(Ze)^2}{a} \tag{1.10}$$

where μ is shear modulus, Z is the proton number of nuclei, a is the number density of nuclei and the a is lattice constant defined as $\frac{4\pi a^4}{3} = \frac{1}{n}$. From this equation, we can see that the shear modulus is strongly depend on the EOS of neutron star crust. Then, in date, the astrophysicist researching the QPOs attempt several EOS of neutron star crust to the shear modulus. On the other hand, it is suggested that proton fraction is related to the differential coefficient of symmetry energy of nuclear matter L. For its definition, L is related

to the pressure of pure neutron matter. Although the property of neutron star matter is slightly different from the one of pure neutron matter, the understanding of L leads to the restriction of the EOS of neutron star. If the QPOs is apprehended by the shear oscillation of neutron star crust, we can restrict the whole EOS of neutron star from information of neutron star crust. Therefore, to gain a deeper understanding of properties of neutron star crust is important.

For the study of pasta structures, since the seminal work of Negele and Vautherin, the Wigner-Seitz approximation has been widely applied to study the inner crust of neutron stars formed of nuclear clusters immersed in a neutron sea. The spherical Winger-Seitz approximation is a computationally very efficient method with the advantage of reducing the three-dimensional partial differential Equations to ordinary differential radial equations. This approximation is twofold. First of all, the momentum $\mathbf{k}$ dependence of Hamiltonian is neglected. Consequently the wave functions and the energies are independent of $\mathbf{k}$ and approximated by the solutions at $\mathbf{k=0}$. Only the band index of each single particle quantum state remains. Secondly, the Wigner-Seitz polyhedron is replaced by a sphere of equal volume. The equations are then usually solved with the Dirichlet-Neumann mixed boundary conditions which yield a nearly constant neutron density outside the cluster. The Wigner-Seitz approximation turns out to be useful if the boundary conditions play a minor role. For instance, bound states whose associated wave functions are vanishingly small outside the clusters are very well treated provided that the spatial extent of these states is smaller than the lattice spacing. This condition is fulfilled almost everywhere in the crust except in the bottom layers where the clusters nearly touch.

On the other hand, by virtue of the recent development in computational science, it becomes possible to calculate without any assumption about the geometry of non-uniform structures [46, 52]. In these studies, one imposes a periodic boundary condition in a small cubic cell, which includes only one period of structures. Although these studies yielded essentially the same results, i.e. typical pasta structures, it is hard to extract further information such as crystalline configuration of "pasta" and mechanical properties. For detailed studies of the properties of the neutron-star crust, it is desired to perform three-dimensional calculations in a periodic cubic cell with sufficiently large sizes. Then, to avoid the ambiguity from the symmetry and to explore the mechanical properties of nuclear matter, we performed dimensional calculations.

This thesis is organized as follows. In Chapter 2, we first introduce the relativistic mean field model Then, the technical method to solve the simultaneous differential equation derived from relativistic mean field theory and parallelization of computational code. Finally, we explain the method to obtain the ground state structure of nuclear matte. Especially, here, we introduce the local chemical potential for nucleon and electron. This local chemical potential is the important key in our calculations. In Chapter 3, we show the main results in my PhD course study. First, we explore the pasta structures and properties of low-density charge-neutral nuclear matter with fixed proton number fractions 0.5, 0.3, and 0.1. Secondly, we also explore catalyzed matter relevant to the neutron-star crust, where a significant difference between results with and without the Wigner Seitz approximation can be seen. It is possible to extend our framework to finite temperatures as in the case of proto-neutron star matter, but, in this thesis, we concentrate on the cold neutron-star crust for simplicity. Third is

the application to the neutron star crust matter. Most part of above three results is refered from Ref. [57]. In fourth section, we calculate the rather realistic shear modulus of neutron star crust because we can treat the nuclei with finite volume and screening effect of electron. We introduce the "distorted" periodic boundary condition to describe the deformation of matter. Finally, by expanding the Lagrangian in RMF model, we treat the nuclear matter in the density region about $3 \sim 5\rho_0$. In this region, the reappearance of "pasta" structures with kaon condensation is expected. We apply our calculating method to this density region and show the appearance of "pasta" structures with kaon condensation. Finally, the summary and future work of this study are given in Chapter 4.

Chapter 2

General framework of method

In this chapter, first, we introduce the relativistic mean field model. This model is not only simple for numerical calculation but also quantitatively reliable for the properties of finite nuclei and the saturation property of matter. Thus, we employ this model. Secondly, we explain the parameter set for this model using in this thesis and show the properties of nuclear matter reproduced by this model. Third is the technical method to solve the simultaneous differential equation derived from relativistic mean field theory and parallelization of computational code. Finally, we explain the method to obtain the ground state structure of nuclear matte. Especially, here, we introduce the local chemical potential for nucleon and electron. This local chemical potential is the important key in our calculations.

2.1 Relativistic mean field model

It is well known that we can explain the nuclear main property by two technique that are old basically and historically. Those two are "droplet model" and "shell model". In the shell model, we can treat N-body problem for nucleons as one-body problem changing in the average field by the interaction of the effective nucleon. In droplet model, nucleons strongly interact each other and move as one group such as nucleus. Therefore, nucleus is treated as tight binding droplet of nucleon.

In the 1950s, nuclear theory researchers have begun to explain the different aspect of the nucleon using field theory. In the field theory, the strong interaction between the nucleon results from the combination with various meson fields. A simple model was written by Johnson and Teller in an article titled "Classical Field Theory of Nuclear Forces" in 1955. This is the origin of the relativistic mean field model. They describe the motion of nucleon in heavy atomic nucleus by the model that can be comprehended by the couple of "nucleon and scalar meson" and "nucleon and vector meson". The scalar meson field plays the role of long and middle range attractive force of nucleons to reproduce the binding energy of nuclei. The vector meson takes the repulsive force between the short distances between the nucleon to reproduce the saturated nature of the nuclear matter.

Besides, Johnson and Teller introduce the two electrically neutral mesons. These two are σ and ω mesons. The energy of the nucleon was calculated using the mean field approximation up to the primary of the coupling constant. The mass of σ meson is treated as 600 MeV in

their calculation. This value show the agreement with the value reproduced by realistic NN interaction. ω meson filed is the vector field and play the role of momentum dependence of one particle potential. Serot and Walecka have refined this model and named this model as "$\sigma-\omega$ model". We can reproduce the saturated density of symmetric nuclear matter using their Lagrangian.

However, the equation of state described by "$\sigma-\omega$ model" is too much stiff. The incompressibility of symmetric nuclear matter provided from this model becomes about 500 MeV. Therefore, what Serot and Teller performed is to take into account not only the interaction by the exchange of one particle between nucleons but also the high order interaction by ω meson. As a result, we can reproduce the saturability of symmetric nuclear matter and restrain the incompressibility by 240 MeV. However, it is impossible to expand this study to the explore of asymmetry nuclear matter such as neutron star only by the study of symmetric nuclear matter. Therefore, Walecka and others introduced the ρ meson which is short-lived and an iso-spin triplet whose three states are denoted as ρ^+, ρ^0, ρ^-. Then, the nuclear force depends on the iso-spin caused by the exchange of ρ-mesons. In addition to the role of σ and ω-meson field, ρ-meson field play the role of short range force of nucleons.

Relativistic mean field model has several merits. This model automatically satisfies the causality, whereas the equation of state obtained by Shrödinger-based theories is no more compelled. Secondly, the coupling constants of relativistic mean filed model can be treated algebraically to the bulk properties of nuclear matter. Thus, the theory can be anchored firmly to the only information we have on high-density matter – (1) causality; (2) microscopic stability $dp/d\rho \geq 0$; (3) saturation properties of symmetry nuclear matter; and (4) at high density the asymptotic freedom of quarks.

In this article, we introduce the Lagrangian represented by sigma (σ), omega(ω^μ), and rho ($\boldsymbol{R}^\mu$) mesons, respectively, together with nucleons ψ, electrons ψ_e, and the electromagnetic field A_μ in a Lorentz-invariant as follows:

$$\begin{aligned}
\mathcal{L} &= \bar{\psi}[i\gamma^\mu\partial_\mu - m_N^* - g_{\omega N}\gamma^\mu\omega_\mu - g_{\rho N}\gamma^\mu\boldsymbol{\tau}\cdot\boldsymbol{R}_\mu - e\frac{1+\tau_3}{2}\gamma^\mu A_\mu]\psi \\
&\quad + \frac{1}{2}(\partial_\mu\sigma)^2 - \frac{1}{2}m_\sigma^2\sigma^2 - U(\sigma) \\
&\quad - \frac{1}{4}\Omega_{\mu\nu}\Omega^{\mu\nu} + \frac{1}{2}m_\omega^2\omega_\mu\omega^\mu - \frac{1}{4}\boldsymbol{R}_{\mu\nu}\boldsymbol{R}^{\mu\nu} + \frac{1}{2}m_\rho^2\boldsymbol{R}_\mu\boldsymbol{R}^\mu \\
&\quad + \bar{\psi}_e[i\gamma^\mu\partial_\mu - m_e + e\gamma^\mu A_\mu]\psi_e \\
&\quad - \frac{1}{4}F_{\mu\nu}F^{\mu\nu},
\end{aligned} \tag{2.1}$$

where $U(\sigma) = \frac{1}{3}bm_N\left(g_{\sigma N}\sigma\right)^3 - \frac{1}{4}\left(g_{\sigma N}\sigma\right)^4$ is a nonlinear term for the scalar field, $m_N^* = m_N - g_{\sigma N}\sigma$ represents the effective mass of the nucleon, $\Omega_{\mu\nu} = \partial_\mu\omega_\nu - \partial_\nu\omega_\mu$, $\boldsymbol{R}_{\mu\nu} = \partial_\mu\boldsymbol{R}_\nu - \partial_\nu\boldsymbol{R}_\mu - g_{\rho N}\left(\boldsymbol{R}_\mu \times \boldsymbol{R}_\nu\right)$, $F_{\mu\nu} = \partial_\mu A_\nu - \partial_\nu A_\mu$, and g_{ab} represent the coupling constant between a and b.

Then, giving the variation of L with respect to each field, we can get the equation of motion for each field.

nucleon:

$$\left[i\gamma^\mu\partial_\mu - m_N^* + g_{\omega N}\omega^\mu + g_{\rho N}\gamma^\mu\boldsymbol{\tau}\cdot\boldsymbol{R}_\mu - e\frac{1+\tau_3}{2}\gamma^\mu A_\mu\right]\psi = 0 \tag{2.2}$$

σ meson:

$$\partial_\mu \partial^\mu \sigma - \left(\bar{\psi} g_{\sigma N} \psi - m_\sigma^2 \sigma - \frac{dU}{d\sigma} \right) = 0 \tag{2.3}$$

ω meson:

$$-\partial_\mu \omega^{\mu\nu} - \left(-g_{\omega N} \bar{\psi} \gamma^\nu \psi + m_\omega^2 \omega^\nu \right) = 0 \tag{2.4}$$

ρ meson:

$$-\partial_\mu \boldsymbol{R}^{\mu\nu} - \left(-g_{\rho N} \bar{\psi} \gamma^\mu \boldsymbol{\tau} \psi + m_\rho^2 \boldsymbol{R}^\nu \right) = 0, \tag{2.5}$$

Coulomb equation :

$$\begin{aligned} -\nabla^2 A_0 &= e\left(\rho_p + \rho_e\right) \\ \nabla^2 \left(-eA_0\right) &= e^2 \left(\rho_p + \rho_e\right) \\ \nabla^2 V &= e^2 \left(\rho_p + \rho_e\right) \equiv e^2 \rho_{\mathrm{ch}} \end{aligned} \tag{2.6}$$

where $\rho_e = -\int d^3x \langle \bar{\psi}_e \psi_e \rangle < 0$.

It is necessary to consider the fields appearing in Lagrangian density to be an operator of the quantum mechanics to treat the relativistic system for quantum mechanics. There are consecutive infinite units in the flexibility labelled coordinate $\overrightarrow{x_i}$, and it is necessary to quantize all of them. It is quantum field theory to have formulated the quantization of such system.

In the case of nuclear matter, we can consider the system as many body systems in an unit of A number nucleons with the non-relativistic frame. On the other hand, when we attempt to describe the system relativistically, we must take into account the flexibility of the infinite unit due to the negative energy state to occupy a vacuum state Therefore, it is generally too difficult to treat such problem. As a method to deal with the field theory of such many body systems easily, the mean field method is often employed. In particular, it is effective when we demand the ground state of the system. We apply this method to the Lagrangian in Eq.(2.1). For meson fields, we use the averaged field without quantum mechanical fluctuation. Therefore, we got the simpler form

$$\langle \sigma \rangle = \sigma \tag{2.7}$$

$$\langle \omega^\mu \rangle = \delta^{\mu,0} \omega \tag{2.8}$$

$$\langle \boldsymbol{R}^\mu \rangle = \delta^{\mu,0} \boldsymbol{R}^\mu \tag{2.9}$$

In Eqs.(2.7)–(2.9), bra and ket represent the expectation value of ground state of nuclear matter. Then, we impose space symmetry and the time reversal characteristics that originally nuclear matter possesses more on this state. The space ingredient of the meson field cannot take a finite value out of space symmetry. Note that only the iso-spin 3-component of the $\boldsymbol{R}^0$ field has finite mean value and the Lorentz three-current part must vanish in the static ground state of matter just as for the omega meson and rho meson. Here after, we describe R_3^0 as R_0.

The nucleons move as independent particles in the meson fields. This means that the nucleon field operator can be expanded in terms of single-particle states and the densities become sums over the single particle wave functions. It is clear that we should in principle take into account the negative energy solution for a fully relativistic description; that means

we should evaluate the vacuum polarization effects to all orders. However, since nucleons and mesons are composite particles and not constituent of a basic field theory, we can reasonably neglect those effects, and restrict he sum to the occupied states.

The equations about the meson fields mentioned above are as follows by performing this operation,

$$\begin{aligned} -\nabla^2\sigma + m_\sigma^2\sigma &= -\frac{dU}{d\sigma} + g_{\sigma N}\left(\rho_p^s + \rho_n^s\right) && (2.10)\\ -\nabla^2\omega_0 + m_\omega^2\omega_0 &= g_{\omega N}(\rho_p + \rho_n) && (2.11)\\ -\nabla^2 R_0 + m_\rho^2 R_0 &= g_{\rho N}(\rho_p - \rho_n) && (2.12)\\ \nabla^2 V &= 4\pi^2\rho^{ch} && (2.13)\\ \rho^{ch} &= (\rho^p - \rho^e) && (2.14) \end{aligned}$$

where ρ and ρ_s is defined as follow,

$$\rho \equiv \langle\psi^\dagger\psi\rangle = 4\int_0^{k_F}\frac{d\boldsymbol{k}}{(2\pi)^3} = \frac{2k_F^3}{3\pi^2} \tag{2.15}$$

$$\begin{aligned} \rho_s \equiv \langle\bar{\psi}\psi\rangle &= \frac{2}{\pi^2}\int_0^{k_F} k^2 dk \frac{m - g_{\sigma N}\sigma}{\sqrt{k^2 + (m - g_{\sigma N}\sigma)^2}}\\ &= \frac{2}{\pi^2}\int_0^{k_F} k^2 dk \frac{m^*}{\sqrt{k^2 + m^{*2}}}. \end{aligned} \tag{2.16}$$

The Energy and momentum tensor is described as follow.

$$\begin{aligned} \hat{T}^{\mu\nu} &= -g^{\mu\nu}(L + L_e)\\ &\quad + \frac{\partial L}{\partial(\partial_\mu\psi)}(\partial^\nu\psi) + \frac{\partial L}{\partial(\partial_\mu\omega_\lambda)}(\partial^\nu\omega_\lambda)\\ &\quad + \frac{\partial L}{\partial(\partial_\mu\boldsymbol{R}_\lambda)}\cdot(\partial^\nu\boldsymbol{R}_\lambda) + \frac{\partial L}{\partial(\partial_\mu A_\lambda)}(\partial^\nu A_\lambda)\\ &= -g^{\mu\nu}(L + L_e)\\ &\quad + \imath\bar{\psi}\gamma^\mu\partial^\nu\psi + \imath\bar{\psi}_e\gamma^\mu\partial^\nu\psi_e\\ &\quad + \partial^\mu\sigma\partial^\nu\sigma - \frac{1}{4}\cdot 4\Omega^{\mu\lambda}\partial^\nu\omega_\lambda - \frac{1}{4}\cdot 4\boldsymbol{R}^{\mu\nu}\cdot\partial^\nu\boldsymbol{R}_\lambda - \frac{1}{4}\cdot 4F^{\mu\lambda}\partial^\nu A_\lambda \end{aligned} \tag{2.17}$$

Here, $\Omega^{\mu\lambda}\partial^\nu\omega_\lambda$ is transformed as follow,

$$\begin{aligned} \Omega^{\mu\lambda}\partial^\nu\omega_\lambda &= (\partial^\mu\omega_\lambda - \partial^\lambda\omega^\mu)\partial^\nu\omega_\lambda\\ &= \partial^\mu\omega^\lambda\partial^\nu\omega_\lambda - \left[\partial^\lambda(\omega^\mu\partial^\nu\omega_\lambda) - \omega^\mu\partial^\nu\partial_\lambda\omega^\lambda\right]\\ &= \partial^\mu\omega^\lambda\partial^\nu\omega_\lambda. \end{aligned} \tag{2.18}$$

where the second and third terms in second line are 0 because of the conservation of flow

density. Similarly,

$$\begin{aligned} -\frac{1}{4}\Omega^{\mu\lambda}\Omega_{\mu\lambda} &= -\frac{1}{2}(\partial_\mu\omega_\lambda\partial^\mu\omega^\lambda - \partial_\mu\omega_\lambda\partial^\lambda\omega^\mu) \\ &= -\frac{1}{2}\partial_\mu\omega_\lambda\partial^\mu\omega_\lambda + \frac{1}{2}\left[\partial_\mu(\omega_\lambda\partial^\lambda\omega^\lambda) - \omega_\lambda\partial^\lambda\partial_\mu\omega^\mu\right] \\ &= -\frac{1}{2}\partial_\mu\omega_\lambda\partial^\mu\omega_\lambda \end{aligned} \tag{2.19}$$

From these equations, the energy and momentum tensor is expressed as follow,

$$\begin{aligned} \hat{\hat{T}}^{\mu\nu} &= -g^{\mu\nu}(L+L_e) + \imath\bar{\psi}\gamma^\mu\partial^\nu\psi + \imath\bar{\psi}_e\gamma^\mu\partial^\nu\psi_e \\ &\quad +\partial^\mu\sigma\partial^\nu\sigma - \partial^\mu\omega^\lambda\partial^\nu\omega_\lambda - \partial^\mu\boldsymbol{R}^\lambda\cdot\partial^\nu\boldsymbol{R}_\lambda - \partial^\mu A^\lambda\partial^\nu A_\lambda \\ &= \imath\bar{\psi}\gamma^\mu\partial^\nu\psi + \imath\bar{\psi}_e\gamma^\mu\partial^\nu\psi_e \\ &\quad -\left[\frac{1}{2}(\partial_\mu\sigma)^2 - \frac{1}{2}m_\sigma^2\sigma^2 - U(\sigma)\right]g^{\mu\nu} \\ &\quad +\left[\frac{1}{2}\partial_\sigma\omega_\lambda\partial^\sigma\omega^\lambda - \frac{1}{2}m_\omega^2\omega_\lambda\omega^\lambda\right]g^{\mu\nu} \\ &\quad +\left[\frac{1}{2}\partial_\sigma\boldsymbol{R}_\lambda\cdot\partial^\sigma\boldsymbol{R}^\lambda - \frac{1}{2}m_\rho^2\boldsymbol{R}_\lambda\cdot\boldsymbol{R}^\lambda\right]g^{\mu\nu} \\ &\quad +\frac{1}{2}\partial_\sigma A_\lambda\partial^\sigma A^\lambda g^{\mu\nu} \\ &\quad +\partial^\mu\sigma\partial^\nu\sigma - \partial^\mu\omega^\lambda\partial^\nu\omega_\lambda - \partial^\mu\boldsymbol{R}^\lambda\cdot\boldsymbol{R}^\nu_\partial b_\lambda - \partial^\mu A^\lambda\partial^\nu A_\lambda \end{aligned} \tag{2.20}$$

Then, by taking the mean field approximation for $(\mu,\nu)=(0,0)$, we got

$$\begin{aligned} \hat{T}^{00}_{RMF} &= \psi^\dagger\left[-\imath\alpha\cdot\nabla + \beta m_n^* + g_{\omega N}\omega_0 + g_{\rho N}R_0 + e\frac{1+\tau_3}{2}A_0\right]\psi \\ &\quad +\frac{1}{2}(\nabla\sigma)^2\sigma^2 + \frac{1}{2}m_\sigma^2 + U(\sigma) \\ &\quad -\frac{1}{2}(\nabla\omega_0)^2 - \frac{1}{2}m_\omega^2\omega_0^2 - \frac{1}{2}(\nabla R_0)^2 - \frac{1}{2}m_\rho^2R_0^2 - \frac{1}{2}(\nabla A_0)^2 \\ &\quad +\psi_e^\dagger\left[-\imath\overrightarrow{\alpha}\cdot\overrightarrow{\nabla} + \beta m_e - eA_0\right]\psi_e. \end{aligned} \tag{2.21}$$

Therefore, the total energy $E=\langle\hat{H}\rangle=\int d^3x\langle\hat{T}^{00}_{RMF}\rangle$ is

$$\begin{aligned} E &= 2\sum_{n,p\in F}\sqrt{k^2+m_N^{*2}} + \int d^3x\left(g_{\omega N}\omega_0(\rho_p+\rho_n) + g_{\rho N}R_0(\rho_p-\rho_n) + eA_0\rho_p\right) \\ &\quad +\int d^3x\left[\frac{1}{2}(\nabla\sigma)^2 + \frac{1}{2}m_\sigma^2 + U(\sigma) - \frac{1}{2}(\nabla\omega_0)^2 - \frac{1}{2}m_\omega^2\omega_0^2 + \frac{1}{2}m_\rho^2R_0^2\right] \\ &\quad -\int d^3x\left[\frac{1}{2}(\nabla A_0)^2\right] + E_e' \\ &= 2\sum_{n,p\in F}\sqrt{k^2+m_N^{*2}} - \int d^3xV\rho_p \end{aligned}$$

$$
\begin{aligned}
&+\int d^3x\left[-\omega_0\nabla^2\omega_0+m_\omega^2\sigma^2-R_0\nabla_0^2R_0+m_\rho^2R_0^2\right]\\
&+\int d^3x\left[\frac{1}{2}\left(\nabla\sigma\right)^2+\frac{1}{2}m_\sigma^2\sigma^2+U\left(\sigma\right)-\frac{1}{2}\left(\nabla\omega_0\right)^2-\frac{1}{2}m_\omega^2\omega_0^2-\frac{1}{2}\left(\nabla R_0\right)^2-\frac{1}{2}m_\rho^2R_0^2\right]\\
&-\int d^3x\left[\frac{1}{2}\left(\nabla A_0\right)^2\right]+E_e'\\
=\;& 2\sum_{n,p\in F}\sqrt{k^2+m_N^{*2}}-\int d^3xV\rho_p\\
&+\int d^3x\left[\frac{1}{2}\left(\nabla\sigma\right)^2+\frac{1}{2}m_\sigma^2\sigma^2+U\left(\sigma\right)+\frac{1}{2}\left(\nabla\omega_0\right)^2+\frac{1}{2}m_\omega^2\omega_0^2+\frac{1}{2}\left(\nabla R_0\right)^2+\frac{1}{2}m_\rho^2R_0^2\right]\\
&+\int d^3x\left[-\frac{1}{2}\left(\nabla A_0\right)^2\right]+E_e^{'} \qquad (2.22)\\
E_e'\;=\;& \int d^3x\left[\frac{2}{\left(2\pi\right)^3}\int_0^{k_F^{(e)}}4\pi k^2dk\sqrt{k^2+m_e^2}-eA_0\left(-\rho_e\right)\right]\\
\approx\;& \int d^3x\left[\frac{2}{\left(2\pi\right)^3}\int_0^{k_F^{(e)}}4\pi k^3dk-\left(-eA_0\right)\rho_e\right]\\
=\;& \int d^3x\left[\frac{k_F^{(e)4}}{4\pi^2}-\left(-eA_0\right)\rho_e\right]\\
=\;& \int d^3x\left[\frac{\left(\mu_e-V\right)^4}{4\pi^2}-V\rho_e\right]\qquad\left(\mu_e\approx k_F^{(e)}+V\right). \qquad (2.23)
\end{aligned}
$$

Here, from the relation between electric field and electrostatic potential, we got the following equation.

$$
\int d^3x\left(-V\right)\left(\rho_p+\rho_e\right)=\int d^3x\left(-V\right)\frac{\nabla^2V}{e^2}=\int d^3x\frac{\left(\nabla V\right)^2}{e^2}=\int d^3x\left(\nabla A_0\right)^2 \qquad (2.24)
$$

Then, using Eq.(2.24), the total energy is expressed as follow,

$$
\begin{aligned}
E\;=\;& 2\sum_{n,p\in F}\sqrt{k^2+m_N^{*2}}\\
&+\int d^x\left[\frac{1}{2}\left(\nabla\sigma\right)^2+\frac{1}{2}m_\sigma^2\sigma^2+U\left(\sigma\right)+\frac{1}{2}\left(\nabla\omega_0\right)^2+\frac{1}{2}m_\omega^2\omega_0^2+\frac{1}{2}\left(\nabla R_0\right)^2+\frac{1}{2}m_\rho^2R_0^2\right]\\
&+\int d^3x\left[\frac{1}{2}\left(\nabla A_0\right)^2+\frac{\left(\mu_e-V\right)^4}{4\pi^2}\right]\\
=\;& E_B+E_M+E_e \qquad (2.25)
\end{aligned}
$$

2.2 Parameter set and EOS of uniform nuclear matter

2.2.1 Parameter set

We use the same parameter set of Ref. [55], which reproduces the saturation property of nuclear matter (Fig. 2.2), and the binding energies and the proton mixing ratios of finite nuclei. We list the parameter set in Table. 2.1.

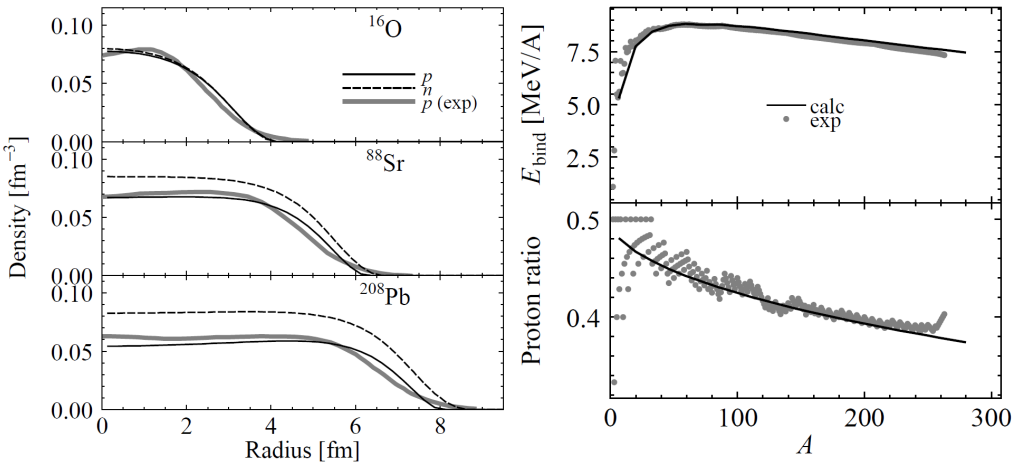

Figure 2.1: Left:the density profiles of typical nuclei. The proton densities (solid curves) are compared with the experiment. Right: the binding energy per nucleon and the proton ration of finite nuclei. These two figures are refereed from Ref. [55]

$g_{\sigma N}$	$g_{\omega N}$	$g_{\rho N}$	b	c	m_σ (MeV)	m_ω (MeV)	m_ρ (MeV)
6.3935	8.7207	4.2696	0.008659	0.002421	400	783	769

Table 2.1: Parameter set

2.2.2 EOS of uniform nuclear matter

With these parameters, we can reproduce the properties of uniform nuclear matter shown in Table. 2.2. The first and second quantities, ρ_0 and ϵ_0, are the saturation density of symmetric nuclear matter ($\sim 0.16\text{fm}^{-3}$) and its energy per nucleon, respectively. The third and forth quantities, K and S_0, are the incompressibility and symmetry energy at ρ_0, respectively. The last one, L, is the slope parameter of symmetry energy at ρ_0. By using these parameters the

binding energy per nucleon around the saturation density is expressed as

$$\frac{E}{A} = \epsilon_0 + \frac{K\left(\rho-\rho_0\right)^2}{18{\rho_0}^2} + \left[S_0 + \frac{L\left(\rho-\rho_0\right)}{3\rho_0}\right]\left(1-2Y_p\right)^2 . \tag{2.26}$$

ρ_0 (fm^{-3})	ϵ_0 (MeV)	K (MeV)	S_0 (MeV)	L (MeV)
0.153	−16.4	240	33.4	84

Table 2.2: EOS of uniform nuclear matter composed by proton and neutron and electron.

Parameters of the RMF model are chosen to reproduce saturation properties of symmetric nuclear matter: the minimum energy per nucleon −16.4 MeV at $\rho = \rho_0$, the incompressibility $K(\rho_0) = 240$ MeV, the effective nucleon mass $m_N^*(\rho_0) = 0.78 m_N$, $m_N = 938$ MeV, and the isospin-asymmetry coefficient $a_{\rm sym} = 33.5$ MeV. Fig. 2.2 shows the binding energy per nucleon of uniform nucleon matter.

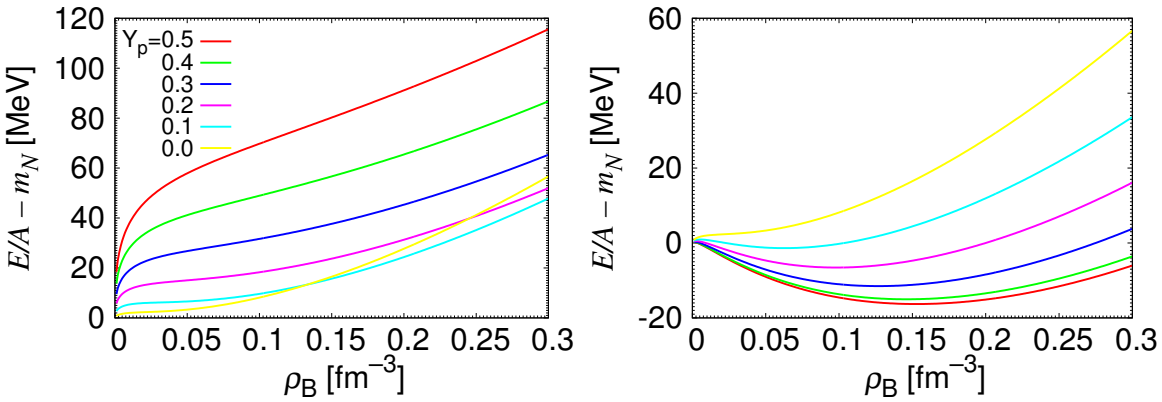

Figure 2.2: EOS of uniform nucleon matter with different number-fraction of proton. Red line indicates symmetric matter (number-fraction of proton $Y_p = 0.5$) and yellow line indicates neutron matter ($Y_p = 0$). Lines with intermediate colors show the case of $Y_p = 0.4$, 0.3, 0.2 and 0.1. Crosses on the lines show the minimum points. Left figure is the case without electron and the Coulomb energy, while the right figure is the case of charge-neutral matter which includes energy of electrons.

The proton mixing ratio Y_p is the ratio of the number of protons (Z) to that of total baryons (A), $Y_p = Z/A$. The saturation property mentioned above is seen for symmetric nuclear matter ($Y_p = 0.5$) in the left panel of Fig. 2.2. Note that if one imposes the charge neutrality by inclusion of electrons, the saturation property cannot be seen (right panel of Fig. 2.2). For the study of non-uniform nuclear matter, the ability to reproduce the bulk properties of finite nuclei should be essential. It was checked how it works to describe finite nuclei in Ref. [55]. In their calculation, for simplicity, the spherical shape of nuclei was assumed. The electron density is set to be zero. Therefore, neither the global charge neutrality condition

nor the local charge-neutrality condition is imposed. In Fig. 2.1 (left panel) we show the density profiles of some typical nuclei. One can see how well our framework may reproduce the density profiles. To get a still better fit, especially around the surface region, we might need to include the derivative terms of the nucleon densities. Fine structures seen in the empirical density profiles, which may come from the shell effects cannot be reproduced by the mean-field theory. The effect of the rearrangement of the proton density distribution is seen in heavy nuclei. Protons repel each other, which enhances their density near the surface of heavy nuclei. This effect is analogous to the charge screening effect for the Coulomb potential in a sense that the proton distribution is now changed not on the scale of the nuclear radius, but on another length scale, which is the proton Debye screening length. It gives rise to important consequences for the pasta structures since the proton Debye screening length is typically less than the lump size. The optimal value of the proton mixing ratio Y_p is obtained by imposing the beta-equilibrium condition for a given baryon number. Fig. 2.1 (right panel) shows the baryon-number dependence of the binding energy per baryon $E_{\rm bind}$ and the proton mixing ratio Y_p. We can see that the bulk properties of finite nuclei (density, binding energy, and proton to baryon number ratio) are satisfactorily reproduced for our present purpose.

Note that in our framework we must use a sigma mass $m_\sigma = 400$ MeV, a slightly smaller value than that one usually uses, to get an appropriate fit. If we used a popular value $m_\sigma = 500$ MeV, finite nuclei would be over-bound by about 3 MeV/A. The actual value of the sigma mass (as well as the omega and rho masses) has little relevance for the case of infinite nucleon matter, since it enters the thermodynamic potential only in the combination e $\tilde{C} = g_{\sigma N}/m_\sigma$. However meson masses are important characteristics of finite nuclei and of other non-uniform nucleon systems, like those in pasta. The effective meson mass characterizes the typical scale for the spatial change of the meson field and consequently it affects the value of the effective surface tension.

2.3 Relaxation method for the density distribution of fermions

To simulate infinite matter, we employ a periodic boundary condition to the calculation cell with a cubic shape. Desirable cell size is large as possible. We divide the cell into grid points. The density distributions and the meson-field profiles are represented by their local values on the grid points. Giving an average densities of protons, neutrons and electrons, but density distributions are randomly provided. The suitable density distributions and fields are searched for. The meson fields and the Coulomb potential are obtained by solving the equations of motion Eqs.(2.10)–(2.13). To obtain the density distributions of nucleons and electrons we introduce local chemical potentials. Accordingly, we also introduce the thermodynamic potential $\Omega = E - \sum_{i=p,n,e} \mu_i \int d^3r \rho_i(\mathbf{r})$ and each chemical potential is obtained by the variation of Ω for each density.

$$\begin{aligned} \mu_p(\mathbf{r}) &= \sqrt{k_{F,p}(\mathbf{r})^2 + m_N^*(\mathbf{r})^2} + g_{\omega N}\omega_0(\mathbf{r}) + g_{\rho N}\rho_0(\mathbf{r}) - V(\mathbf{r}) \\ &= \sqrt{(3\pi^2\rho_p(\mathbf{r}))^{2/3} + m_N^*(\mathbf{r})} + g_{\omega N}\omega_0(\mathbf{r}) + g_{\rho N}R_0(\mathbf{r}) - V(\mathbf{r}) \end{aligned} \tag{2.27}$$

$$\begin{aligned}\mu_n(\mathbf{r}) &= \sqrt{k_{F,n}(\mathbf{r})^2 + m_N^*(\mathbf{r})} + g_{\omega N}\omega_0(\mathbf{r}) - g_{\rho N}\rho_0(\mathbf{r}) \\ &= \sqrt{(3\pi^2\rho_n(\mathbf{r}))^{2/3} + m_N^*(\mathbf{r})} + g_{\omega N}\omega_0(\mathbf{r}) - g_{\rho N}R_0(\mathbf{r}) \qquad (2.28)\\ \mu_e(\mathbf{r}) &= \left(3\pi^2\rho_e(\mathbf{r})\right)^{1/3} + V(\mathbf{r}) \qquad (2.29)\end{aligned}$$

The equilibrium state is determined so that the chemical potentials are independent of the position. An exception is the region with a particle density equals to zero, where the chemical potential of that particle becomes higher.

1. Solve the equation of motion for three meson and Poisson equation in the given proton, neutron and electron density distributions.
2. Calculate the chemical potentials on all of the grid points.
3. Compare chemical potentials on the neighbor six grid points.
4. If the chemical potential of the point under consideration is larger than that of another, give some part of the density to the other grid point.

These processes are repeated until the uniformity of chemical potentials are achieved. To avoid the appearance of different chemical potential regions, the comparison of chemical potentials between separated regions and exchange of densities among them are done adequately.

As mentioned before, we use a cubic cell with a periodic boundary condition. If the cell size is small and includes only one or two units of the structure, the geometrical shape should be affected by the boundary condition and the appearance of some structures is implicitly suppressed. Therefore, the cell size should be so large as to include several units of the pasta structure. We divide the cell into three-dimensional grids. The desirable grid width should be so small as to describe the detailed density distribution, particularly at the nuclear surface. Due to this requirement, we set the grid width to 0.3 fm at the largest. This grid width is small enough to give an energy difference within 2 keV from that with 0.1 fm. More precise information is written in Appendix.

Chapter 3

Results

In this chapter, we show several calculations for nuclear matter with RMF model in three-dimensional way. First, we present some results for fixed proton number-fraction Y_p with 0.5 (symmetric nuclear matter), 0.3, and 0.1 which are roughly relevant to supernova and neutron-star crust. In our calculations, the electrons are slightly polarized around the clusters of protons by self-consistent treatment of the Coulomb potential and the electron density distribution. By comparing with the results assuming the electron density distribution is uniform, we show the screening effect of electrons. Second is the application to the neutron star crust matter. Adding only the beta-equilibrium condition, we can treat the neutron star crust matter. In previous studies with WS approximation, it is believed that boby-centred cubic lattice of droplets is the ground state structure. Performing three-dimensional calculations, we investigate the crystalline structure without any assumption of geometry and whether "pasta" structures appear or not. In third section, we calculate the realistic shear modulus of neutron star crust because we can treat the nuclei with finite volume and screening effect of electron. We introduce the "deformed" periodic boundary condition to describe the deformation on matter with periodicity. Finally, by expanding the Lagrangian in RMF model, we explore the nuclear matter in the density region of $3 \sim 5\rho_0$. In this region, the reappearance of "pasta" structures with kaon condensation is expected. We apply almost same treatment of density distributions of fermion and chemical potentials to this density region and show the appearance of "pasta" structures with kaon condensation.

3.1 Fixed proton-fraction

3.1.1 Y_p=0.5

For $Y_p = 0.5$, we explore the ground state structures in the density region of $\rho_{\rm B} = 0 \sim 0.16{\rm fm}^{-3}$. Shown in Fig. 3.1 are all of the proton and electron density distributions of ground state structure appearing in cold symmetric nuclear matter. Since the bulk density distributions of proton and neutron are almost the same, we pretermit the depiction of neutron density distribution in Fig. 3.1. We can see that the typical pasta phases with rods, slabs, tubes, and bubbles, in addition to spherical nuclei (droplets), are reproduced by our calculation in which no assumption on the structures was used. In Fig. 3.1, from left to right, the average baryon densities increase. Then, the same behavior of phase transition

is also reproduced. Furthermore, these cells include several units and we can specify these lattice structures. The crystalline configuration of droplets and bubbles is fcc; rods and tubes exhibit a honeycomb configuration.

We show the density distribution of fermions and Coulomb potential for Y_p=0.5 at $\rho_{\rm B}$=0.03 fm^{-3} in Fig. 3.2. Here, in the left figure, we show the proton density distribution on a sliced plane in rod structure and depict the two kinds of density profiles of protons, neutrons, and electrons and the Coulomb potential in the right figure. One is along a vertical line (v) which passes through the rods; another is along a horizontal one (h). We can see that the proton density is highest near the surface due to Coulomb repulsion, while the neutron density distribution is flat inside the rods. Electrons are spread over all space but slightly localized around the rods which brings about the charge screening effect.

While the central region of density distribution of protons in rods is different from that of neutrons by Coulomb repulsion, at a glance of the density distribution of proton and neutron, they have almost the same behavior. We can grasp this phenomena as congruence. Since the value of Coulomb repulsion is smaller than the symmetry energy by proton and neutron, this phenomena should occur even if the Coulomb repulsion acts on this system. From this figure, the unique features of three-dimensional calculation can be seen. The proton, neutron, and electron density distributions are almost the same for both cases of (v) and (h). However, a slight difference appears in the Coulomb potential. For convenience, we have set the maximum value of Coulomb potential to be zero. In the rod phase, the points on which the Coulomb potential is zero correspond to the centroid of the triangular lattice. These points are included not on the path (v) but on the path (h). Considering the importance of distinct relation between the Coulomb and surface energies for the pasta structure, we should take into account this anisotropy in a proper way in the case of applying some geometrical assumption.

In Fig. 3.3, we show the energy, total pressure, and baryon partial pressure as functions of density. Baryon partial pressure is given by subtracting the electron contribution from the total pressure. Note that the energy $E/A - m_N$ includes the kinetic energy of electrons, which makes the total pressure positive. The appearance of non-uniform structures would make nuclear matter more stable: the energy per baryon gets lower up to about 15 MeV/A compared to uniform matter and the pressure per baryon gets higher up to about 0.5 MeV/A. The equilibrium structure of nuclear clusters in nuclear matter results from Eq.(1.9). But, from this equilibrium condition, while the transition from spherical droplet to other structures can be comprehended, the mechanism of appearance of "pasta" structure including droplet is obscure. Using Fig. 3.3, we can understand this mechanism as follow. Pressure of charge neutral uniform nuclear matter is positive and increases monotonously by virtue of electron. On the other hand, the baryon partial pressure of uniform nuclear matter is negative in low-density region. Negative pressure means that the system is unstable and phase separation might occur to make the baryon pressure to be zero. This phase separation is exactly the appearance of non-uniform structures. In our calculation, the region which the system has the non-uniform structures is spinodal region. By the existence of surface and separated regions in nuclear matter, the surface tension and Coulomb repulsion are imposed on the system. In some density region, these two added contributions make the non-uniform structure unstable due to the energy loss. Therefore, in accordance with Eq.(1.9), the structure change the

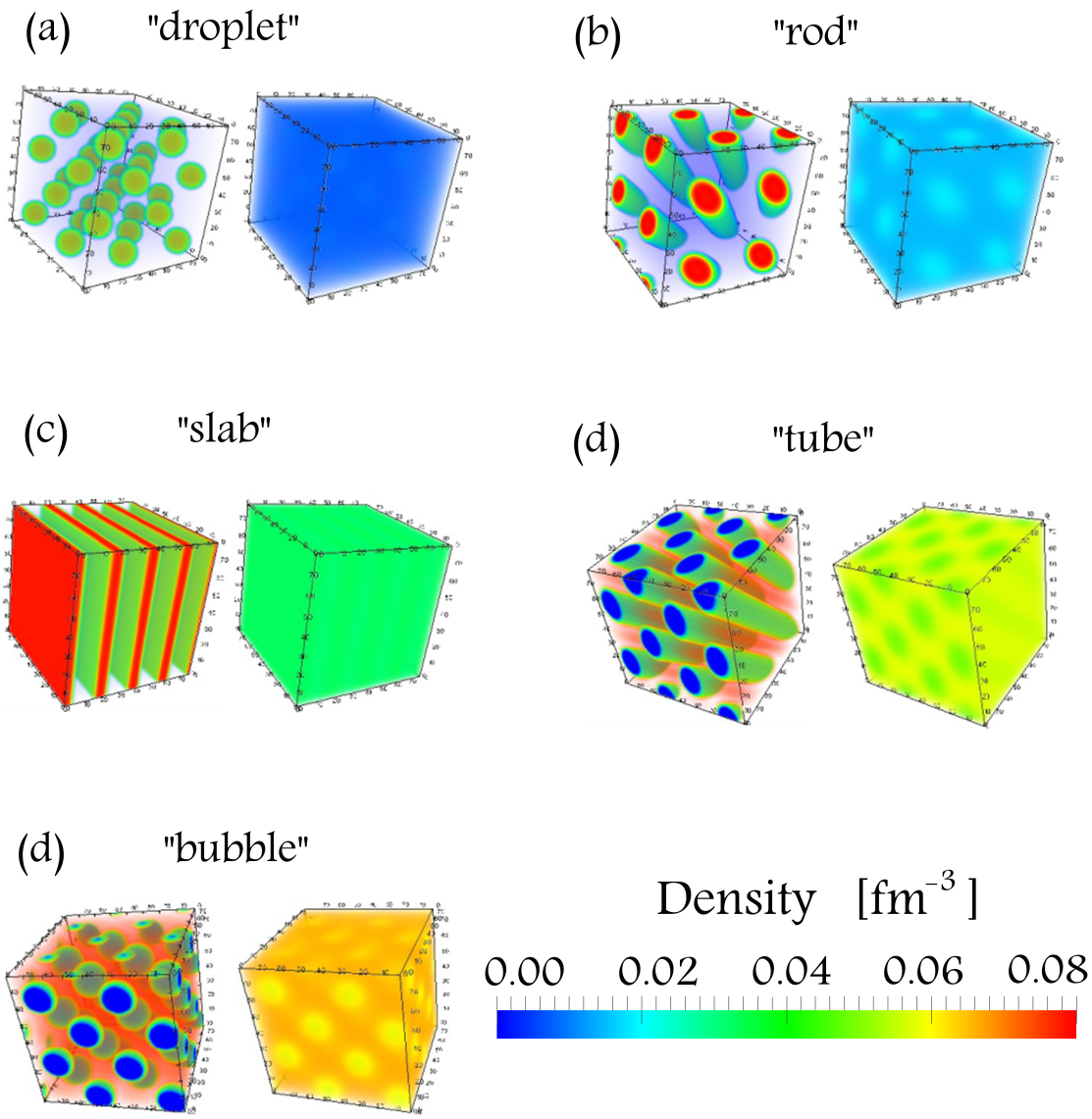

Figure 3.1: Proton density distributions (left part) and electron density distribution (right part) in the ground states of symmetric matter (Y_p =0.5). Typical pasta phases are observed: (a) Spherical droplets with an fcc crystalline configuration at baryon density $\rho_B = 0.01$ fm^{-3}, of 98 fm each side. (b) Cylindrical rods with a honeycomb crystalline configuration at 0.024 fm^{-3}, of 76 fm each side. (c) Slabs at 0.05 fm^{-3}, of 95 fm each side. (d) Cylindrical tubes with a honeycomb crystalline configuration at 0.08 fm^{-3}, of 79 fm each side. (e) Spherical bubbles with a fcc crystalline configuration at 0.09 fm^{-3}, of 97 fm each side.

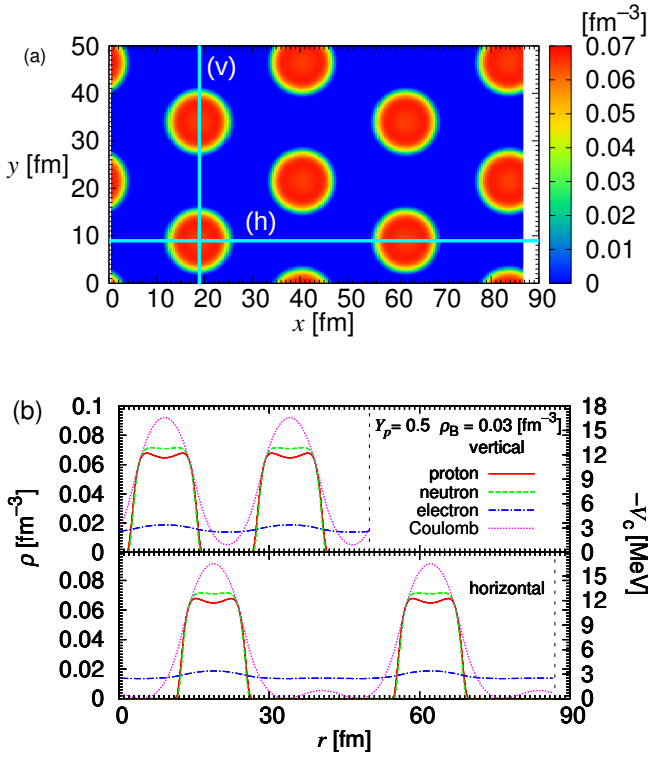

Figure 3.2: (a) Proton density distribution in the rod phase ($\rho_B = 0.03$ fm^{-3} for Y_p =0.5) on the sliced plane. (b) The density distribution along a line (v)(vertical) and (h)(horizontal) in the upper figure. Red (solid line) lines indicate protons, green (dashed) line neutrons, blue (dot-dashed) lines electrons and pink (dotted) lines the Coulomb potential.

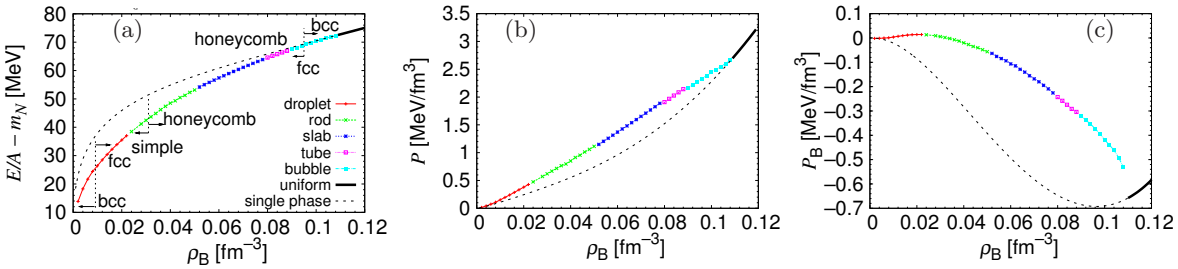

Figure 3.3: From the left, energy (a), pressure (b), and baryon partial pressure(c) of Y_p=0.5. Red lines (with pluses) indicate droplets, green (with crosses) rods, blue (with stars) slabs, magenta (with open squares) tubes, cyan (with full squares) bubbles, and black uniform, respectively. The transition density from bcc droplet to fcc droplet exists around 0.010 fm^{-3} for $Y_p = 0.5$. All the transition densities among different crystalline configurations, including the ones indicated in the figure, have numerical ambiguity of 0.002 fm^{-3}. These figures are reffereed from Ref. [57]

form from droplet to rod, slab, tube and bubble structures. As for the equation of state of nuclear matter, the energy of non-uniform nuclear matter decrease from that of uniform one and the pressure of non-uniform nuclear matter increase. Namely, to avoid the negative baryon partial pressure and to decrease the energy are the true nature of appearance of "pasta" structures. However, near the normal nuclear density, by too large contribution from the Coulomb repulsion and the surface tension, there is the region where uniform structure is energetically stable even if the baryon partial pressure is negative. Whether the system becomes uniform or non-uniform is decided by the negative baryon partial pressure and the balance between the surface tension and Coulomb repulsion.

Structure	droplet	rod	slab	tube	bubble
Density [fm^{-3}]	0.00 – 0.024	0.026 – 0.050	0.052 – 0.078	0.080 – 0.088	0.090 – 0.11

Table 3.1: Density region of each "pasta" structures of $Y_p = 0.5$.

We have obtained almost the same EOS as that given by the WS approximation [55], in which the same RMF model is applied. However, one of the differences between our results and those with the WS approximation appears in the existence region of each pasta structure. The density region of rod phase is wider and the tube narrower in our calculation. Since the energy differences between different structures are quite small, the crystalline configuration might affect the appearance of each pasta structure.

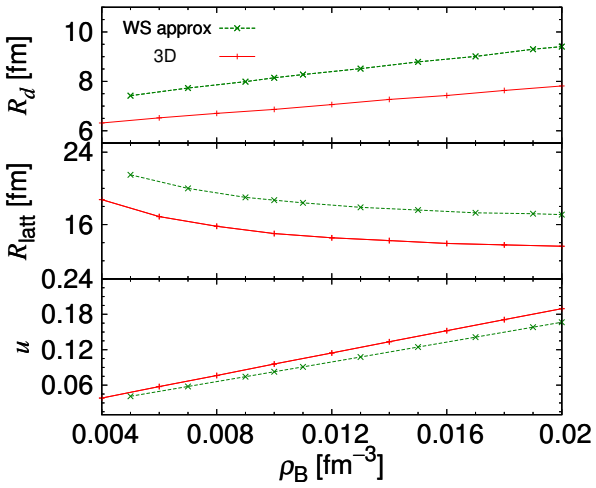

Figure 3.4: Density dependence of the radius, the lattice constant, and the volume fraction. Red lines are our results and green lines are those with the WS approximation.

Fig. 3.4 shows the radii of droplets R_d, the lattice constant $R_{\rm latt}$, and the volume fraction u in the droplet phase. Here, R_d and $R_{\rm latt}$ are defined as follows,

$$\frac{V}{N_d} = \frac{4\pi}{3} R_{\rm latt}^3, \tag{3.1}$$

$$R_d = R_{\rm latt}\left(\frac{\langle\rho_p\rangle^2}{\langle\rho_p^2\rangle}\right)^{1/3}, \tag{3.2}$$

and $u = (R_d/R_{\rm latt})^3$, where V denotes the cell volume, N_d the number of droplets in the cell, and the bracket $\langle ...\rangle$ means the average over the cell volume. Comparing the present results with those using the WS approximation, the volume fraction exhibits the same behavior, but the lattice constant and the radius of the droplet the different behavior. This might be caused by some differences of the treatment of the Coulomb interaction between the present calculation and the one using the WS approximation.

Although any unusual structure does not appear in the ground state, one new feature emerges in the crystalline configuration of droplets. It has been considered within CLDM that a body-centered cubic (bcc) lattice is energetically favored than the face-centered cubic (fcc) lattice by the Coulomb energy [41]. However, in our calculation, the fcc lattice emerges as a ground state at some density region. Crystalline configurations of the bcc and fcc lattices give rise to a subtle difference of the Coulomb energy, which amounts to about 0.2–0.8 MeV. The ratio of the Coulomb energy to the total energy difference is about 22%. In other words, the major contribution to the energy comes from the mean-fields and the kinetic energies of nucleons, i.e., the bulk energy of nuclear matter. Therefore, the ansatz used in the previous studies, e.g., CLDM, should be dangerous since small differences in size and composition of droplets give a significant change in the total energy of the system. Table. 3.2 shows the

ρ_B [fm^{-3}]	0.012	0.014	0.016	0.018	0.020
R_d(fcc) [fm]	6.86	7.04	7.23	7.61	7.79
R_d(bcc) [fm]	6.99	7.18	7.36	7.75	7.92

Table 3.2: Density dependence of the droplet radii for the fcc and bcc lattices for $Y_p = 0.5$.

density dependence of radii of the droplets in the cases of the fcc and bcc lattices. The radius of the droplet is different even if their baryon densities are the same.

Same problem remains in bubble structures. As with the case of droplet structure, there is the region where the fcc lattice is energetically favor than the bcc lattice. For bubble structures, nuclear radius is defined as

$$R_d = R_{\rm latt}\left(1 - \frac{\langle\rho_p\rangle^2}{\langle\rho_p^2\rangle}\right)^{1/3}. \tag{3.3}$$

Table. 3.3 shows the density dependence of radii of bubbles structure in the cases of fcc and bcc lattice. The radii of bubble structure are different between in the fcc and bcc lattice even if their baryon densities are the same.

In Ref. [41], it has been reported that the bcc lattice is realized in the ground state for both cases of droplets and bubble structure, by comparing only the Coulomb energy in bcc and fcc crystalline of droplets and bubbles with same size, while the bcc and fcc lattice have the different size of droplets and bubbles in our calculation even if the same baryon density is applied. In the medium-density region, an fcc lattice is more favored than a bcc lattice.

ρ_B [fm^{-3}]	0.09	0.094	0.098	0.102	0.106
R_d(fcc) [fm]	10.24	9.92	9.62	9.34	9.08
R_d(bcc) [fm]	10.02	9.70	9.40	9.12	8.90

Table 3.3: Density dependence of the bubble radii for the fcc and bcc lattices for $Y_p = 0.5$.

This difference may partially come from the treatment of the size of droplets and bubbles in bcc and fcc lattice.

3.1.2 Y_p=0.3

Next, we show the results for $Y_p = 0.3$. We explore the ground state in the density region of $\rho_{\rm B} = 0 \sim 0.16{\rm fm}^{-3}$. In Fig. 3.5, all of the proton and neutron density distributions of ground state structure appearing in nuclear matter with fixed proton-fraction $Y_p = 0.3$ are shown. Since the amount of electrons is small, it is hard to distinguish the non-uniform distribution of them. Then, unlike in Fig. 3.1, we pretermit the depiction of density distribution of electron and, alternatively, depict the neutron density distribution in Fig. 3.5. As in the case of $Y_p = 0.5$, we can see the typical pasta phases with rods, slabs, tubes, and bubbles, in addition to spherical nuclei (droplets) and typical phase transition of pasta structures.

In Fig. 3.6, we depict the density profiles of proton, neutron, electron and the Coulomb potential for $Y_p = 0.3$ at $\rho_{\rm B} = 0.03$ fm^{-3} of rod structure along a line which passes through the rods in the same way as in Fig. 3.2. We can still see that the proton density is highest near the surface due to Coulomb repulsion, while the neutron density distribution is flat inside the droplet. By the increase of the amount of neutrons, some of them exuded from the droplet, which is almost the same situation of the neutron skin in neutron-rich nuclei. Electron density is spread over all space but slightly localized around the protons distribution which brings about the charge screening effect while the amount of electrons is less than that of $Y_p = 0.5$.

Structure	droplet	rod	slab	tube	bubble
Density [fm^{-3}]	0.00 – 0.022	0.023 – 0.036	0.037 – 0.06	0.061 – 0.07	0.071 – 0.094

Table 3.4: Density region of each "pasta" structures of $Y_p = 0.3$.

In Fig. 3.7 we show the energy, total pressure, and baryon partial pressure as functions of density. Comparing the EOS given by using WS approximation, we have obtained almost the same EOS. However, one of the differences between our results and those with the WS approximation appears in the existence region of each pasta structure. Shown in Table. 3.4 is the density range of each pasta structures. The density region of the rod is wider and the tube narrower in our calculation. Comparing with the case of WS approximation, since the energy differences between different structures are quite small, the crystalline configuration might affect the appearance of each pasta structure.

As with the case for $Y_p = 0.5$, there is the region where the fcc lattice is energetically favor than bcc lattice for droplet structures. Crystalline configurations of the bcc and fcc lattices

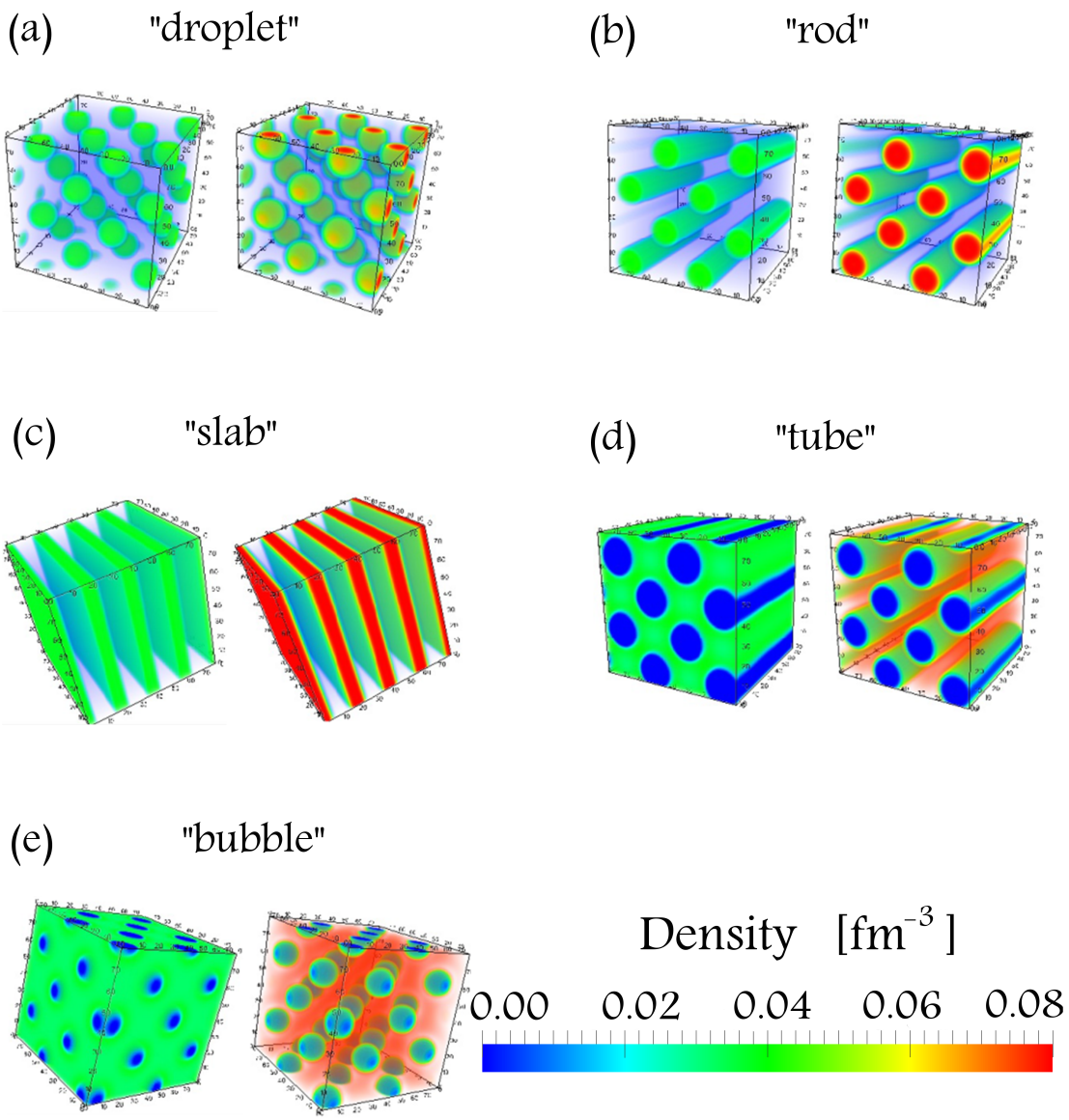

Figure 3.5: Proton and neutron density distributions in the ground states of Y_p =0.3. Typical pasta phases are observed: (a) Spherical droplets with an fcc crystalline configuration at baryon density $\rho_B = 0.01$ fm^{-3}, of 109 fm each side. (b) Cylindrical rods with a honeycomb crystalline configuration at 0.03 fm^{-3}, of 87 fm each side. (c) Slabs at 0.05 fm^{-3}, of 100 fm each side. (d) Cylindrical tubes with a honeycomb crystalline configuration at 0.066 fm^{-3}, of 81 fm each side. (e) Spherical bubbles with a fcc crystalline configuration at 0.094 fm^{-3}, of 99 fm each side.

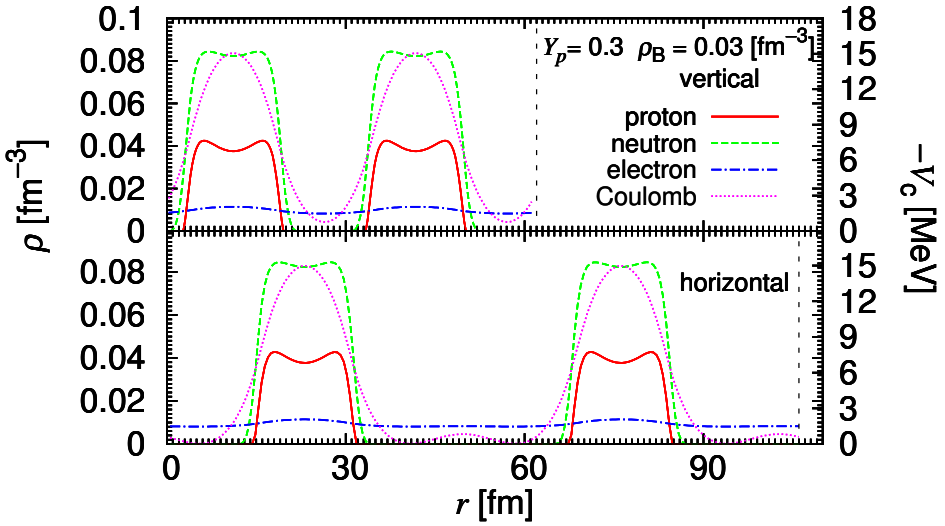

Figure 3.6: Density distribution of protons, neutrons, and electrons and the Coulomb potential of rods in $\rho_B = 0.025$ fm^{-3} of $Y_p = 0.3$. Red (solid) lines indicate protons, green (dashed) lines neutrons, blue (dot-dashed) lines electrons, and pink (dotted) lines the Coulomb potential.

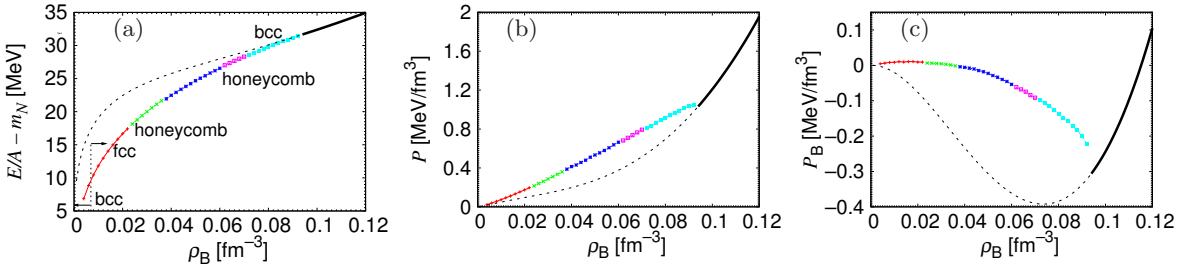

Figure 3.7: From the left, energy (a) pressure (b), and baryon partial pressure(c), of Y_p=0.3. Red lines (with pluses) indicate droplets, green (with crosses) rods, blue (with stars) slabs, magenta (with open squares) tubes, cyan (with full squares) bubbles, and black uniform, respectively. The transition density from bcc droplet to fcc droplet exists around 0.007 fm^{-3}. All the transition densities among different crystalline configurations, including the ones indicated in the figure, have numerical ambiguity of 0.002 fm^{-3}. These figures are reffereed from Ref. [57]

give rise to a subtle difference of the Coulomb energy, which amounts to about 0.1–0.5 MeV. The ratio of the Coulomb energy to the total energy difference is about 15%. Table. 3.5 shows

ρ_B [fm^{-3}]	0.004	0.008	0.012	0.018	0.020
R_d(fcc) [fm]	9.66	9.98	10.32	10.68	11.12
R_d(bcc) [fm]	9.88	10.12	10.58	10.96	11.52

Table 3.5: Density dependence of the droplet radii for the fcc and bcc lattices for $Y_p = 0.3$.

the density dependence of radii of the droplets in the cases of the fcc and bcc lattices. The radii of droplets are different between in fcc and bcc lattice even if their baryon densities are the same one. This difference might contribute the energy difference of fcc and bcc lattice of droplets.

Same problem also remains in bubble structures for $Y_p = 0.3$. But, unlike the case of $Y_p = 0.5$, the lattice structure of bubble of $Y_p = 0.3$ is fcc in all region where bubble structure appear. The radius of the bubble is different even if their baryon densities are the same.

ρ_B [fm^{-3}]	0.08	0.082	0.084	0.086	0.088
R_d(fcc) [fm]	13.56	13.26	12.98	12.70	12.46
R_d(bcc) [fm]	13.42	13.14	12.86	12.60	12.36

Table 3.6: Density dependence of the bubble radii for the fcc and bcc lattices for $Y_p = 0.3$.

3.1.3 Y_p=0.1

In Fig. 3.8, we show all of the proton and neutron density distribution of ground state structures appearing in the density range of $0 < \rho_{\rm B} < 0.1{\rm fm}^{-3}$. As in the case of $Y_p = 0.3$, we pretermit the depiction of density distribution of electron in Fig. 3.8. While in the few amount of proton, all of the typical pasta structures could appear as ground state. In Fig. 3.9, we depict the density profiles of proton, neutron, electron and the Coulomb potential for $Y_p = 0.1$ at $\rho_{\rm B} = 0.03$ fm^{-3} of rid structure along a line which passes through the rods in the same way as in Fig. 3.9. Even in the case of $Y_p = 0.1$, we can see that the proton density is highest around the surface due to Coulomb repulsion. We can also see the specific phenomena different from the case of Y_p=0.5 and 0.3. While, for $Y_p = 0.5$ and 0.3, there appear vacant regions of neutron, the neutron density is finite at any space for Y_p =0.1: the space is filled with dripped neutrons. This phenomenon can be seen in all density region where "pasta" structures appear.

As with the case for $Y_p = 0.5, 0.3$, there is the region where the fcc lattice is energetically favor than bcc lattice for droplet structures. Crystalline configurations of the bcc and fcc lattices give rise to a subtle difference of the Coulomb energy, which amounts to about 0.1–0.5 MeV. The ratio of the Coulomb energy to the total energy difference is about 10%. Table. 3.8

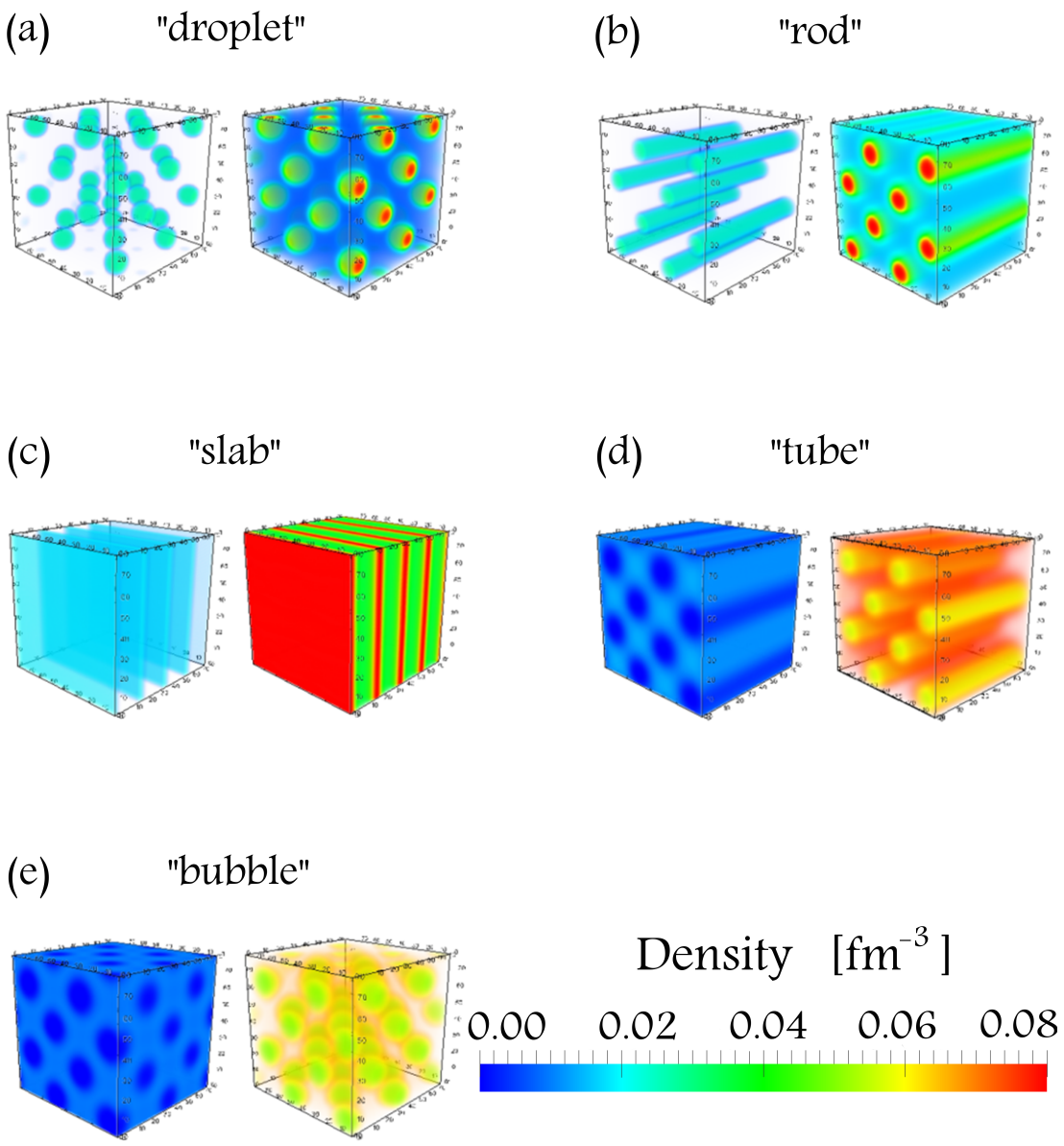

Figure 3.8: Proton and neutron density distributions in the ground states of Y_p =0.1. Typical pasta phases are observed: (a) Spherical droplets with an fcc crystalline configuration at baryon density $\rho_B = 0.024$ fm^{-3}, of 102 fm each side. (b) Cylindrical rods with a honeycomb crystalline configuration at 0.044 fm^{-3}, of 84 fm each side. (c) Slabs at 0.056 fm^{-3}, of 90 fm each side. (d) Cylindrical tubes with a honeycomb crystalline configuration at 0.064 fm^{-3}, of 86 fm each side. (e) Spherical bubbles with a fcc crystalline configuration at 0.068 fm^{-3}, of 91 fm each side.

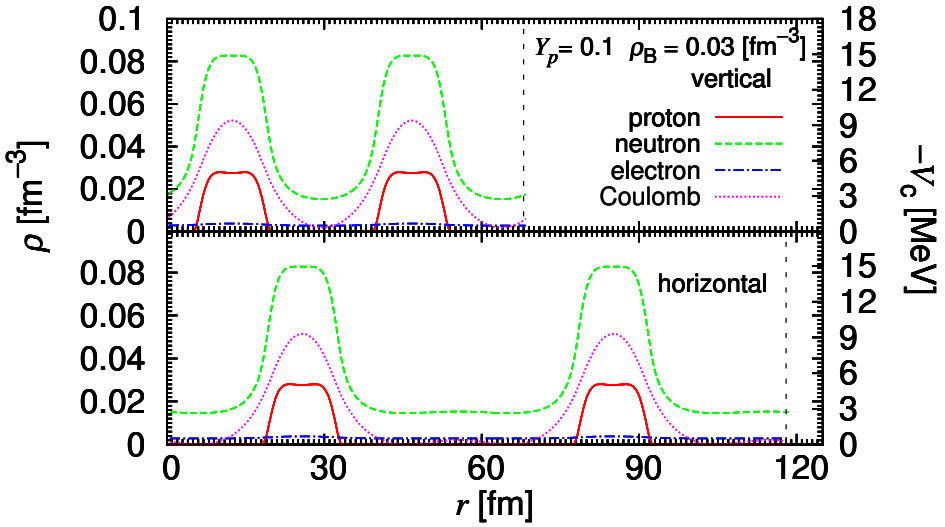

Figure 3.9: Density distribution of protons, neutrons, and electrons and the Coulomb potential of rods in $\rho_B = 0.036$ fm^{-3} of $Y_p = 0.1$. Red (solid) lines indicate protons, green (dashed) lines neutrons, blue (dot-dashed) lines electrons, and pink (dotted) lines the Coulomb potential.

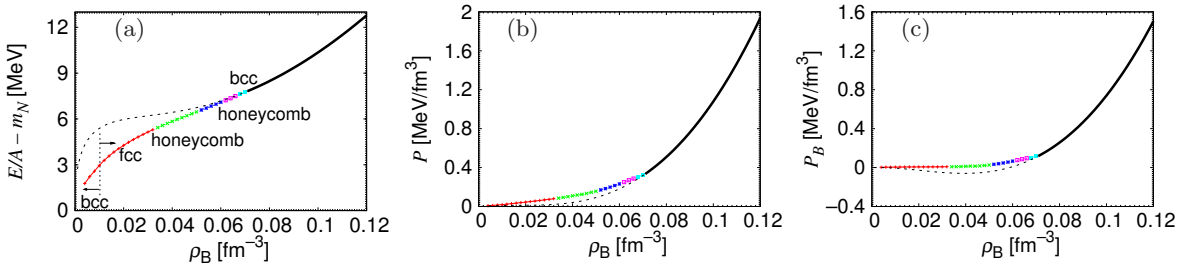

Figure 3.10: From the left, energy (a) pressure (b), and baryon partial pressure(c), of Y_p=0.1. Red lines (with pluses) indicate droplets, green (with crosses) rods, blue (with stars) slabs, magenta (with open squares) tubes, cyan (with full squares) bubbles, and black uniform, respectively. The transition density from bcc droplet to fcc droplet exists around 0.007 fm^{-3}. All the transition densities among different crystalline configurations, including the ones indicated in the figure, have numerical ambiguity of 0.002 fm^{-3}. These figures are reffereed from Ref. [57]

Structure	droplet	rod	slab	tube	bubble
Density [fm^{-3}]	0.00 – 0.032	0.034 – 0.05	0.053 – 0.06	0.062 – 0.064	0.066 – 0.07

Table 3.7: Density region of each "pasta" structures of $Y_p = 0.1$.

ρ_B [fm^{-3}]	0.004	0.008	0.012	0.018	0.020
R_d(fcc) [fm]	9.66	9.98	10.32	10.68	11.12
R_d(bcc) [fm]	9.88	10.12	10.58	10.96	11.52

Table 3.8: Density dependence of the droplet radii for the fcc and bcc lattices for $Y_p = 0.1$.

shows the density dependence of radii of the droplets in the cases of the fcc and bcc lattices. The radius of the droplet is different even if their baryon densities are the same.

3.1.4 Charge screening effect

To see the effects of the electron distribution on the crystalline configuration, let us compare two cases within our framework: one is the full calculation and another is the case for which uniformly distributed electrons are assumed. Full calculation correspond to the mentioned calculation up to this point in this thesis. In the latter calculation, the Coulomb potential $V_{\rm Coul}$ in Eq.(2.29) is replaced by a constant V_0=0 and $\rho_e = (\mu_e - V_0)^3/3\pi^2$. However, in the case of uniformly distributed electrons, gauge invariance is partially violated, since we replace $V_{\rm Coul}$ by V_0 in the equation for the electron chemical potential but retain $V_{\rm Coul}$ in the equation for the proton chemical potential and thus in the expression for the proton number density. We call this calculation as no e-screening calculation in contrast with full-calculation.

We show the results of no e-screening calculation for $Y_p = 0.5, 0.3, 0.1$ in Fig. 3.11. The EOS as a whole do not show any dependence on the treatments of the Coulomb interaction. This agrees with a general statement that the variational functional is always less sensitive to the choice of the trial functions than the quantities linearly depending on them. Nevertheless, the appearance density of each structures especially for tube and bubbles are different. In full calculations, bubble regions are $0.084 - 0.11$fm^{-3} for $Y_p = 0.5$ and $0.071 - 0.094$fm^{-3} for $Y_p = 0.3$, tube regions are $0.078 - 0.083$fm^{-3}, $0.061 - 0.07$fm^{-3}. On the other hands, in no e-screening calculations, bubble regions are $0.086 - 0.099$fm^{-3} for $Y_p = 0.5$ and $0.074 - 0.084$fm^{-3} for $Y_p = 0.3$, tube regions are $0.076 - 0.085$fm^{-3}, $0.065 - 0.073$fm^{-3}. For most of "pasta" structures of Y_p=0.5 and 0.3 in no e-screening calculations, the appearance regions are shorten. Then, in no e-screening calculations, the pasta structures disappear earlier rather than full calculations. For $Y_p = 0.1$ case, the differences between full and no e-screening calculations are completely eliminated.

In the QMD calculations [84] that precede the present calculation without geometrical structures being assumed, droplets form a bcc lattice. This difference might come from the treatment of electrons or the charge screening effect since a uniform electron distribution has been assumed in the QMD calculation. In this case, the droplets have a smaller size compared with that in the full calculation in throughout the density region of the droplet phase. This means that the Coulomb repulsion among protons is slightly weaker in the full calculation due to the screening by electrons. One can see this difference in Table. 3.9.

In the previous study using the WS approximation [55], a similar discussion was presented. We argued that charge screening effect is not so remarkable due to the large Debye screening length. Indeed, the crystalline configuration does not change in our present calculation. Thus, it is confirmed that the charge screening by electrons does not affect the crystalline

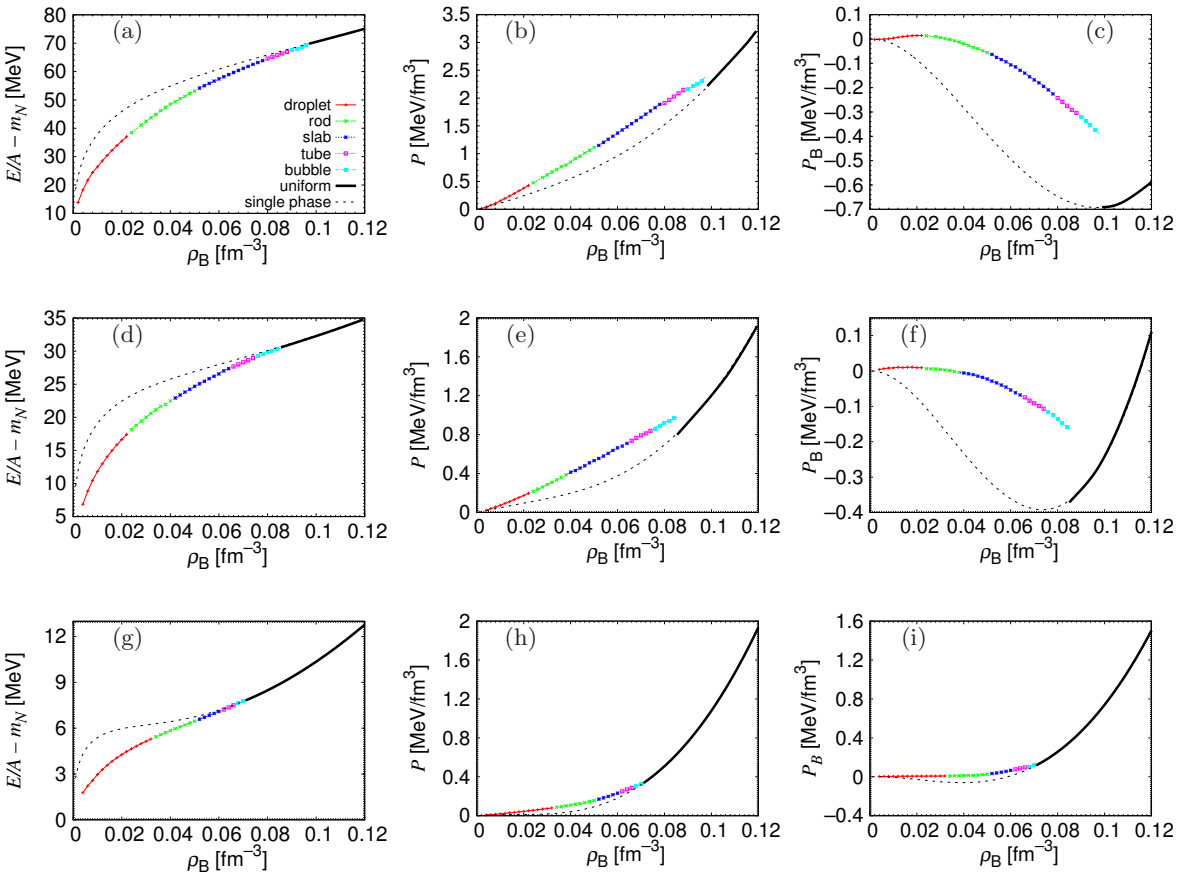

Figure 3.11: EOS of the fixed proton number-fraction nuclear matter with uniform electrons. From the left, energy [(a), (d), and (g)], pressure [(b), (e), and (h)], and baryon partial pressure[(c), (f), and (i)] of Y_p=0.5 [(a), (b), and (c)], 0.3 [(d), (e), and (f)], and 0.1 [(g), (h), and (i)] in this order from the upper panel. Red lines (with pluses) indicate droplets, green (with crosses) rods, blue (with stars) slabs, magenta (with open squares) tubes, cyan (with full squares) bubbles, and black uniform, respectively. All the transition densities among different crystalline configurations, including the ones indicated in the figure, have numerical ambiguity of 0.002 fm^{-3}.

ρ_B (fm^{-3})	0.004	0.01	0.016	0.022
R_d (full calculation) (fm)	6.09	6.67	7.23	7.79
R_d (uniform electron distribution) (fm)	5.91	6.40	7.01	7.64

Table 3.9: The radii of droplets obtained from the full calculation and with uniformly distributed electrons.

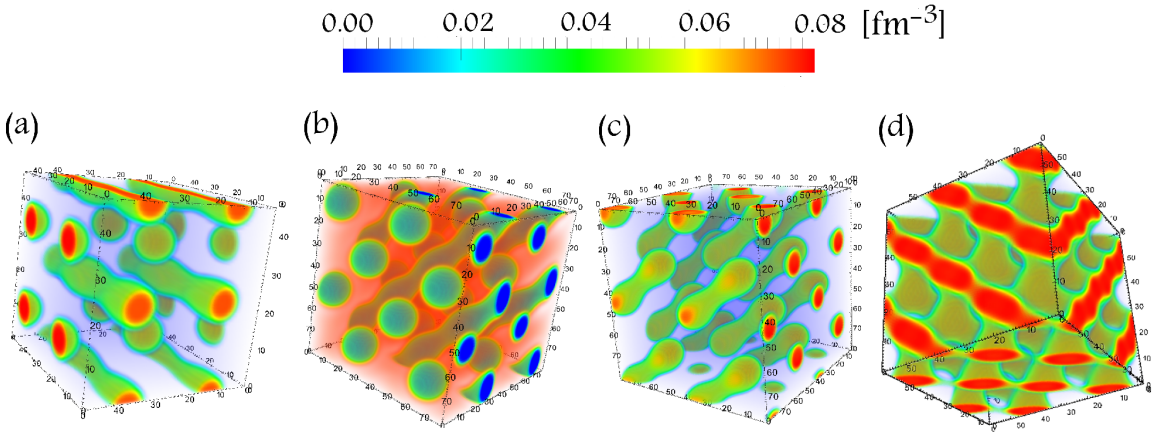

Figure 3.12: Proton density distributions with exotic structures ($Y_p = 0.5$). (a) Mixture of droplet and rod, 0.022fm^{-3}; (b) tube and bubble, 0.088fm^{-3}; (c) dumbbell like structure, 0.018fm^{-3}; (d) diamond like structure, 0.048fm^{-3}

configuration significantly. This difference in crystalline configuration between the QMD calculation and the present calculation remains to be elucidated as a future problem.

3.1.5 Exotic structures

On the way of searching for the ground state structure, we sometimes observe exotic structures which are energetically metastable. In Fig. 3.12, for example, we show the proton density distributions of them appearing in the case of $Y_p = 0.5$. Fig. 3.12 (a) shows a mixed structure of droplet and rod at $\rho_{\rm B} = 0.022{\rm fm}^{-3}$. Similarly, (b) is a mixed structure of tube and bubble at $\rho_{\rm B} = 0.088{\rm fm}^{-3}$. These structures appear around densities where the structures change to other ones; from droplet to rod, and tube to bubble structure. If these structures had appeared as ground states, transition from droplet to rod, and from slab to tube would happen more smoothly by way of those intermediate structures. In fact, the QMD calculations have reported some intermediate structures of droplet and rod, slab and tube as ground states. We have observed more exotic structures: Panel (c) at 0.018 fm^{-3} looks like dumbbells which have been reported to appear in the dynamical compression of matter. Finally, panel (d) at 0.044 fm^{-3} is a diamond structure, which resembles double-diamond structure studied with a compressible liquid drop model. It is difficult to for these structures to be the ground state since they have larger surface area than simple pasta structures. However, at finite temperatures, these structures might contribute to the Boltzmann ensemble.

To avoid the appearance of different local chemical potential region, the density exchange between the distant regions was carried out. Therefore, we could exclude the possibility to be fall into the local minimum point which correspond to the metastable state to a certain degree. However, as shown in Fig.3.12, some metastable states appear. In panel (d), nucleons are distributed continuously in all space without any separated region. In panel (c), all of dumbbell-like structures have same size. These two type structures certainly have the uniformity of chemical potentials. In panel (a) and (b), there are two type structures, droplets

and rods, tubes and bubbles, respectively. Each structures are untouched. Since the shapes of rods and tubes smoothly are changed near the droplets and bubbles, it was avoided to have the different local chemical potentials.

In our framework, these structures are regarded as meta-stable state. From the viewpoint of symmetry, it is reasonable that the typical pasta structures appear as ground state in whole density region where the pasta structures exist. However, the energy differences between typical pastas and exotic ones are small. In other parameter set or framework, these exotic structures might appear in ground state like QMD calculations. As the anisotropy of Coulomb potential make the fcc lattice of droplets ground state, some of exotic structures in Fig. 3.12 appear as in ground state.

3.2 Beta-equilibrium

Cold catalyzed matter requires beta-equilibrium instead of the fixed proton number fraction: $\mu_n = \mu_p + \mu_e$. This situation is correspond to be in the neutron star crust. Shown in Fig. 3.13 are the proton density distributions in the ground states for cold catalyzed nuclear matter. We have obtained the bcc lattice of droplets, fcc lattice of droplets, and honeycomb lattice of rods, depending on density. In Fig. 3.14, the density profiles of fermions in the bcc and fcc lattices of droplets and the Coulomb potential are depicted along a line which passes through the droplets for $\rho_B \approx 0.01$ fm^{-3} and $\rho_B \approx 0.03$ fm^{-3}. The effect of Coulomb repulsion can be seen where the proton density is highest near the surface, while the neutron density distribution is flat inside the droplet. We have observed only those three structures (a), (b), and (c) in Fig. 3.13. This result is consistent with the previous study of the relation between the density region of the pasta structure and the slope parameter L of Eq.(2.26) [85]. The larger the value of L is given, the narrower the pasta region is. In our calculation, L is about 80 MeV, which is close to the critical value ≈ 90 MeV in the CLDM, where the pasta structures do not appear. In the previous calculation using the WS approximation, only the droplet structure appeared as a ground state [55]. However, in our three-dimensional calculation using the same RMF framework, the rod structure also appears.

We show the density dependence of the total energy, the Coulomb energy, and the proton number fraction in Fig. 3.15. To see the difference between droplets in the bcc and fcc lattices, we plot the density dependence of the size of the droplet, the lattice constant, the volume fraction, the proton number in each droplet and the proton number fraction in Fig. 3.16. Here, the meaning of R_d and $R_{\rm latt}$ are the same as in Eqs.(3.1) and (3.2).

The density dependence of the ground-state energy is shown in the left panel of Fig. 3.15. We can see that the ground state configuration changes depending on density. In the lower density region, droplets with the bcc lattice appear. Around $\rho_{\rm B} \approx 0.01$ fm^{-3}, the lattice structure changes from bcc to fcc. A remarkable change occurs around $\rho_{\rm B} \approx 0.052$ fm^{-3}: from the fcc lattice of droplets to the honeycomb lattice of rods. It is hard to see the total energy difference between the bcc and fcc lattices of droplets. That of the proton number fraction at $\rho_{\rm B} < 0.01$ fm^{-3} is also hard to distinguish in the right panel of Fig. 3.15. However, there are significant differences in the proton number fraction at $\rho_{\rm B} > 0.01$ fm^{-3} and the Coulomb energy, as shown in the middle panel of Fig. 3.15.

As in the case of fixed proton number fraction, there emerges an fcc lattice of droplets near

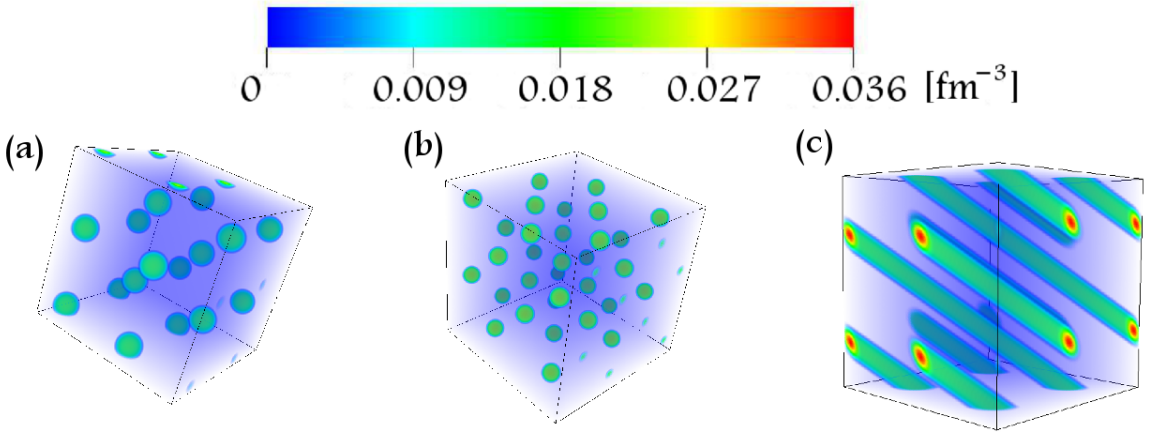

Figure 3.13: Proton density distributions for (a) droplets (bcc) at $\rho_B = 0.01$ fm^{-3}, of 194 fm each side, (b) droplets (fcc) at $\rho_B = 0.03$ fm^{-3}, of 162 fm each side, and (c) rods (honeycomb) at $\rho_B = 0.056$ fm^{-3}, of 144 fm each side. These figures are reffereed from Ref. [57]

the transition density from the droplet phase to another in our calculation, while it has been regarded to take a bcc lattice in the previous studies [41]. Almost the same radii and density distribution of droplet, proton number fraction, and proton number in nuclei are obtained for both crystalline configurations (see the right panel of Fig. 3.16 at $\rho_B < 0.01$ fm^{-3}). The difference between the bcc and fcc lattices may be seen only in the Coulomb energy: the Coulomb energy of the fcc lattice is a little higher than that of the bcc lattice. However, near the transition density from droplet to rod, the radius of droplets and the proton number fraction are different between the bcc and fcc lattices even if their baryon-number densities are the same (see Fig. 3.16 at $\rho_B \approx 0.02$ fm^{-3}): the size of the droplet and the proton number fraction in the fcc lattice are 7.54 fm and 0.016, respectively, while those in the bcc lattice are 7.01 fm and 0.014. Because the size of droplets and the proton number fraction are different, the Coulomb energy alone is no longer the criterion of the ground state. We should take into account the size of droplets and the proton number fraction so as to look for the ground state in a self-consistent way. Roughly speaking, the larger the radius of droplets is, the smaller the surface energy is. While the Coulomb energy of the fcc lattice is larger than that of the bcc lattice in all the region of the droplet phase, the total energy of the fcc lattice is less than that of the bcc lattice by the gain of surface energy.

Because we cannot take into account shell effects [45], the proton number continuously decreases with increase of baryon number density. To compare the density dependence of the proton number within the same interaction for baryons, our model might be similar to type B in Ref. [85]. In our model, the slope parameter of symmetry energy L is a little larger than that in Ref. [85], so that the proton number converges to about 35 in the low-density limit, while it converges to about 40 in Ref. [85]. This result is consistent with the relationship between L and the proton number in the droplet.

The maximum size of the droplet can be estimated by the Bohr-Wheeler condition as $E^{(0)}_{\rm Coul} > 2E_{\rm surf}$ [86]. The "virial" theorem for the pasta structure reads $E_{\rm surf} = 2E_{\rm Coul}$, where $E^{(0)}_{\rm Coul}$ is the Coulomb energy of an isolated nucleus and the Coulomb energy of a nucleus in

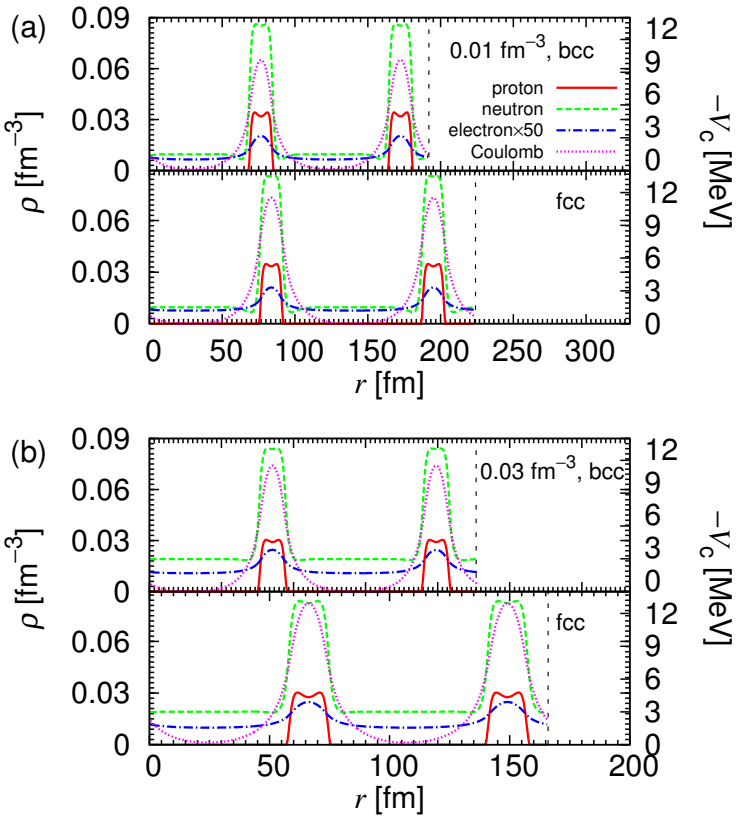

Figure 3.14: Density distributions of protons, neutrons, and electrons and the Coulomb potential in the fcc and bcc lattices [(a) ρ_B=0.01 fm^{-3}; (b) ρ_B=0.03 fm^{-3}]. In each panel (a) and (b), the upper figure shows the case of bcc and the lower the case of fcc. Red (solid) lines indicate the protons, green (dashed) lines neutrons, blue (dot-dashed) lines electrons (multiplied by a factor of 50) density distributions, pink (dotted) lines show the Coulomb potential, and black dashed lines are the lattice constant. These figures are reffereed from Ref. [57]

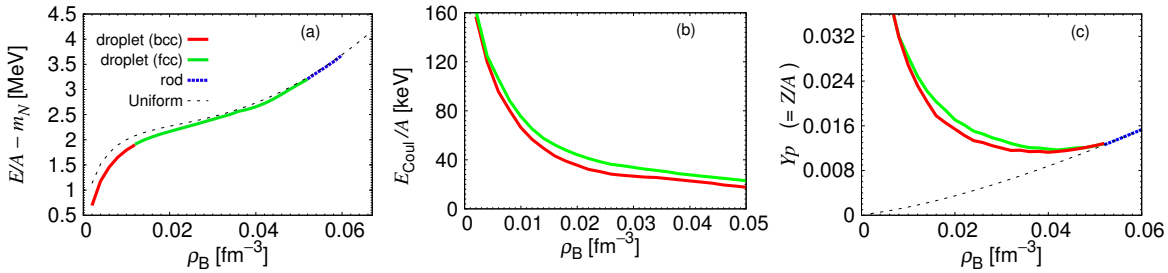

Figure 3.15: From the left, the total energy, the Coulomb energy per nucleon, and proton number fraction. Red (black) lines indicate fcc droplets, green (gray) bcc droplets, blue (short dashed) lines rods, respectively. Dotted lines are for the case of a single phase. These figures are reffereed from Ref. [57]

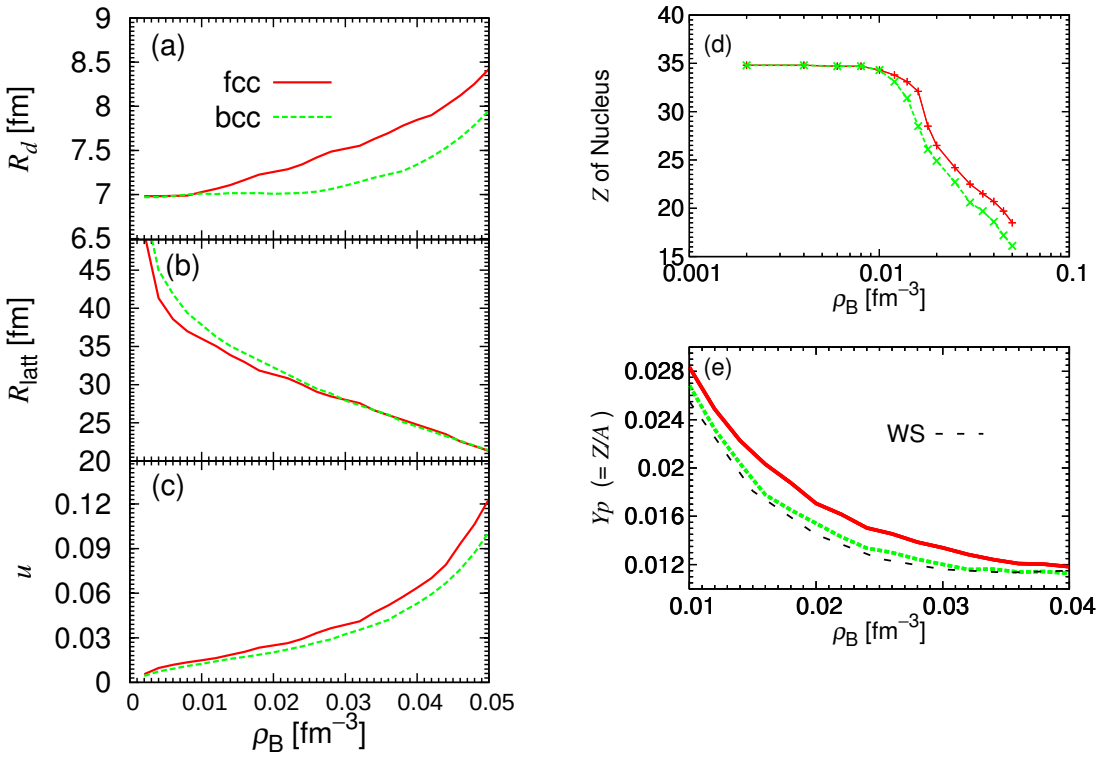

Figure 3.16: (a) The density dependence of radii of nuclei, (b) lattice constants, and (c) the volume fraction. The proton number of nuclei and the proton number fraction are in panels (d) and (e), respectively. The red (solid) lines in each panel indicates fcc and the green (dashed) lines indicate bcc in comparison with results from the WS approximation. These figures are reffereed from Ref. [57]

matter is $E_{\rm Coul} \approx E^{(0)}_{\rm Coul}(1-3u^{1/3}/2)$. From these equations, the appearance of non-spherical nucleus in nuclear matter has been expected for a volume fraction $u > 0.125$. However, in our calculation, the structural change from droplet to rod occurs around $u \approx 0.1$ (see the value at $\rho_B \approx 0.05$ fm^{-3} in Fig. 3.16). This means that considering the non-uniformity of the electrons is worthwhile for "pasta" structures, because the relation between the Coulomb energy of a cell and that of a nucleus has been derived by using a uniform background of electrons and uniform baryon density inside a nucleus. The effect of the screening by charged particles, which is properly included in our calculation, may be one of the origins of this difference. To reach a final conclusion on this issue, we should perform another calculation with uniformly distributed electrons and confirm the effects of electron non-uniformity. Also the difference in the droplet surface may give another reason: the CLDM treated droplets with a sharp surface, while our droplets have a diffuse surface. The same discussion may apply to the QMD calculation for the case of fixed proton number fraction.

At low density, where the volume fraction of droplet is less than 1%, we can regard nuclei as point particles even if there is a broad distribution of neutron. However, near the transition density from droplet to rod, the volume fraction amounts to about 10% and the

distance between the nuclei is very small, which is one reason for the shape transition. In this region, the approximation for each droplet as a point particle is not valid.

3.3 Shear modulus of neutron star

As mentioned in Chapter. 1, the mechanical property of neutron star crust matter is the one of keys for comprehending the mechanisms of QPOs in SGRs and restricting the EOS of neutron star. Ogata *et al.* have calculated shear moduli of neutron star crust matter by first-principle study for Monte-Carlo simulation with one-component plasma model and indicated the useful formula [87]. Almost of astrophysicist rely on the formula for shear modulus. Recently, using Molecular Dynamics simulations, shear moduli are calculated and almost same results are obtained. However, on these calculations, one basically question arises. Can we represent the shear modulus with assumption on which nuclei could be treated as charged point particles? Practically, in the neutron star crust, the nuclei with finite-volume are submerged in dripped neutron and degenerated electron. The total energy change including the nuclear force should be considered for the shear modulus. In the previous section. 3.2, we have obtained not only an EOS of neutron-star crust matter but also the three-dimensional data of these structures by relativistic mean-field model. Therefore, we can treat the nuclei with finite volume filled in degenerated electrons and dripped neutrons. Although the deformation of crystalline structure may not affect the shape of nuclei, the deformation of nuclei is also considered. Then, the realistic shear modulus could be understood by using these benefits. Besides, although the shear modulus of other inhomogeneous structures are treated to be zero in QPOs simulations, it is also possible to estimate the shear modulus of "pasta" structures.

In this section, first, we explain how to treat the deformation in a cubic cell with periodicity which is called "deformed" periodic boundary condition in this thesis and calculate the shear modulus as in the Ref. [87–89]. We performed two type calculations: semi-full calculation and full calculation. In both cases, as initial condition, we use the three-dimensional data of cold catalyzed matter obtained in the section. 3.2 and treat the nuclei with finite volume under the beta-equilibrium condition. In semi-full calculation, all of three equations of motion for meson fields and Poisson equation are solved in deformed periodic boundary condition under the preservation of density distribution of proton and neutron. In this calculation, the forces between nucleons and Coulomb potential are obtained with finite volume of nuclei. According to the treatment of gauge invariance in Coulomb potential, we can treat the screening effect of slightly polarized electron. However, the beta-equilibrium condition is no more held. Then, we could compare with previous studies of Ref. [87–89]. On the other hand, in full calculation, we recover the beta-equilibrium condition by considering the relaxation of density distributions of fermions in relevant periodic boundary condition. Then, due to conservation of the beta-equilibrium, some additional effects of nuclear matter might appear such as the change of proton fraction. Comparing these two calculations, we could investigate the effects of finite volume of nuclei and dripped neutron.

3.3.1 Treatment of deformation

To calculate the shear modulus, we follow the procedure introduced by Ogata *et al.*in Ref. citeogata1. Under the deformation, the coordinates r_i of an droplet get mapped to r_i',

$$r_i' = \sum_{k=1}^{3} (\delta_{ik} + u_{ik})\, r_k \tag{3.4}$$

where u_{ik} describe the deformation strain defined as

$$u_{ik} \equiv \frac{1}{2}\left(\frac{\partial u_i}{\partial x_k} + \frac{\partial u_k}{\partial x_i}\right). \tag{3.5}$$

$\vec{u}$ is an displacement vector of nuclei with deformation. From the general symmery relations, the change in free energy with deformation δF for ideal cubic lattice can be expressed in terms of elastic constants c_{11}, c_{12} and c_{44},

$$\delta F = \frac{1}{2}(c_{11} - c_{12})\, u_{ii}^2 + c_{44} u_{ik} u_{ki} \qquad (i \neq k) \tag{3.6}$$

As the deformation which contribute the estimation of shear modulus, we consider six deformation $D_i (i = 1 \ldots 6)$ that conserves the system volume to order ϵ^2.

$$D_1 \quad : u_{xx} = \epsilon + \frac{3}{4}\epsilon^2, \;\; u_{yy} = u_{zz} = -\frac{\epsilon}{2} \tag{3.7}$$

$$D_2 \quad : u_{yy} = \epsilon + \frac{3}{4}\epsilon^2, \;\; u_{xx} = u_{zz} = -\frac{\epsilon}{2} \tag{3.8}$$

$$D_3 \quad : u_{zz} = \epsilon + \frac{3}{4}\epsilon^2, \;\; u_{xx} = u_{yy} = -\frac{\epsilon}{2} \tag{3.9}$$

$$D_4 \quad : u_{xy} = u_{yx} = \frac{\epsilon}{2}, \;\; u_{zz} = \frac{\epsilon^2}{4} \tag{3.10}$$

$$D_5 \quad : u_{yz} = u_{zy} = \frac{\epsilon}{2}, \;\; u_{xx} = \frac{\epsilon^2}{4} \tag{3.11}$$

$$D_6 \quad : u_{zx} = u_{xz} = \frac{\epsilon}{2}, \;\; u_{yy} = \frac{\epsilon^2}{4}. \tag{3.12}$$

From each deformation D_m, we calculate a value f_m $(m = 1 \ldots 6)$,

$$f_m = \frac{1}{V}\frac{d^2 E_{\mathrm{tot}}}{d\epsilon^2} \tag{3.13}$$

where E_{tot} is the total energy in deformation, V is the system volume.

For a body centred cubic crystal, one has [87]

$$f_1 = f_2 = f_3 = 3b_{11} = 3\,(c_{11} - c_{12}) \tag{3.14}$$

and

$$f_4 = f_5 = f_6 = c_{44} \tag{3.15}$$

In practice, we calculate all of six f_m independently and average to determine b_{11} and c_{44}. The angle averaged shear modulus is [87],

$$\mu_{\text{eff}} = \frac{(2b_{11} + 3c_{44})}{5} \tag{3.16}$$

If the neutron-star crust involves many crystal domains of random orientation, then μ_{eff} is the appropriate elastic constant to determine the speed of shear waves.

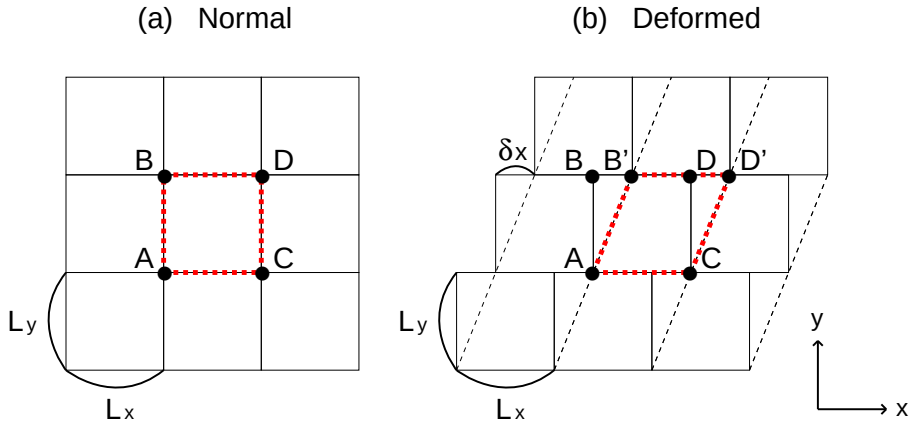

Figure 3.17: Schematic view of two type boundary condition in simplified particular case: (a) "Normal" periodic boundary condition. (b) "Deformed" periodic boundary condition.

To treat the deformation of D_4, D_5, D_6 in a cubic cell, we introduce a "deformed" periodic boundary condition. We show the schematic picture of two type of periodic boundary condition in Fig. 3.17. In the usual way, "normal" periodic boundary condition is defined as follow; For two variables function $F(x, y)$ with periodicity L_x,L_y in each direction,

$$F(x + L_x, y) = F(x - L_x, y) = F(x, y),$$
$$F(x, y + L_y) = F(x, y - L_y) = F(x, y)$$

are held. In Fig. 3.17(a), we consider the squared region ABCD as computational space. Then, for "normal" periodic boundary condition, line AC is connected to line BD and line AB to line CD. On the other hand, for "deformed" periodic boundary condition,

$$F(x + L_x, y) = F(x - L_x, y) = F(x, y),$$
$$F(x, y + L_y) = F(x - \delta_x, y), \quad F(x, y - L_y) = F(x + \delta_x, y)$$

are held in one-directional deformation. In Fig. 3.17 (b), the line AB is still connected to the line CD. However, the line AC is no more connected to the line BD. For "deformed" boundary condition, the line AC is connected to B'D-BB'. Therefore, by obeying the above relation, the one of lattice vectors is changed from $\vec{AB}$ to $\vec{AB'}$ and practically the parallelogram AB'D'C is treated as the primitive lattice while we set the rectangle ABCD as numerical calculation space. While, for simplicity, we treat the one-directional deformation for the explanation

of "deformed" periodic boundary condition, we could straightforwardly expand this periodic boundary condition to two-directional deformation in the same way.

For the deformation of D_1, the following equations are derived from Eqs.(3.4) and (3.8).

$$\begin{aligned} r'_x &= \sum_{k=1}^{3} (\delta_{xk} + u_{xk})\, r_k, \quad r'_y = \sum_{k=1}^{3} (\delta_{yk} + u_{yk})\, r_k, \quad r'_z = \sum_{k=1}^{3} (\delta_{zk} + u_{zk})\, r_k, \\ &= \left(1 + \epsilon + \frac{3}{4}\epsilon^2\right) r_x \qquad = \left(1 - \frac{\epsilon}{2}\right) r_y, \qquad = \left(1 - \frac{\epsilon}{2}\right) r_z \end{aligned} \tag{3.17}$$

Then, the grid widths of each direction dr_x, dr_y, dr_z are changed in deformation as follow,

$$dr'_x = \left(1 + \epsilon + \frac{3}{4}\epsilon^2\right) dr_x, \quad dr'_y = \left(1 - \frac{\epsilon}{2}\right) dr_y, \quad dr'_z = \left(1 - \frac{\epsilon}{2}\right) dr_z. \tag{3.18}$$

Therefore, we can treat the deformation of D_1, D_2, D_3 by increasing and decreasing the grid widths adequately in "normal" periodic boundary condition.

3.3.2 Application to cold catalyzed matter

First, we have performed the semi-full calculation in which we relax all mean fields and Coulomb potential. Therefore, the beta-equilibrium is no more held. But, this situation is almost the same for previous study [87] without the treatment of finite volume of nuclei, nuclear matter and Coulomb screening. Thereupon, we performed the semi-full calculations. For initial condition, we read out the three-dimensional data of density distributions of proton, neutron, and electron, and meson fields and Coulomb potential for each average baryon density. For every possibilities, we add the deformation to these density distributions and Coulomb potential along with the deformation.

In Fig. 3.18 (a), we give three examples of proton density distribution of ground state in "deformed" boundary condition for three value of $\epsilon = 0, 0.05, 0.1$ in D_1 deformation. We can see that nuclei stand in line along with the primitive lattice vectors which are changed in "deformed" boundary condition while, in the case of $\epsilon = 0$, the nuclei form the bcc lattice. Shown in Fig. 3.18 (b) is the dependence of ϵ on the energy difference from the energy in $\epsilon = 0$ at $\rho_{\rm B} = 0.03\text{fm}^{-3}$. From the definition of the strain, we should treat the deformation within the linearity in this thesis. Then, to get the value of Eq.(3.13), we fit the deformation energy in panel (b) of Fig. 3.18 by the function of ϵ^2 using the data of $\epsilon \leq 0.1$ to maintain the linearity and the coefficient of this function represents the value of f_m. We show the fitted-line in Fig. 3.18 by green (dotted) line. For $\epsilon \leq 0.2$ the assumption of linearity on the response to the deformation comport with the results. Green (dotted) line overlap with red (solid) line. For $\epsilon > 0.2$, the green (dotted) line gradually shift from the red (solid) line. This disagreement might come from the effect of non-linearity in deformation and the volume effects of nuclei.

Performing these procedures to several baryon densities, we obtained the shear moduli of nuclear matter in semi-full calculation. Panel (a) in Fig. 3.19 is the shear moduli. We show three lines. Red line indicate the second derivative of the total energy by ϵ, blue one indicates

(a)

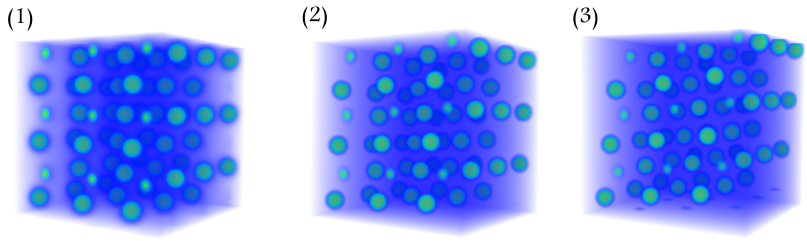

(b)

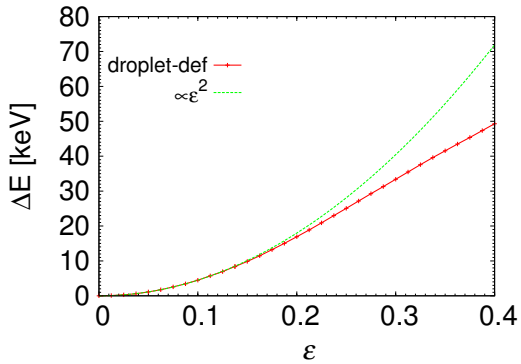

Figure 3.18: (a) Proton density distributions in several ϵ value of deformed boundary condition, $\epsilon = 0, 0.05, 0.1$ for (1), (2), (3) respectively.
(b) The dependence of ϵ for energy difference from the energy in $\epsilon = 0$ at $\rho_{\mathrm{B}} = 0.03\mathrm{fm}^{-3}$ indicated by red line. Green line indicate the fitted-line as a function of ϵ^2.

(a) (b)

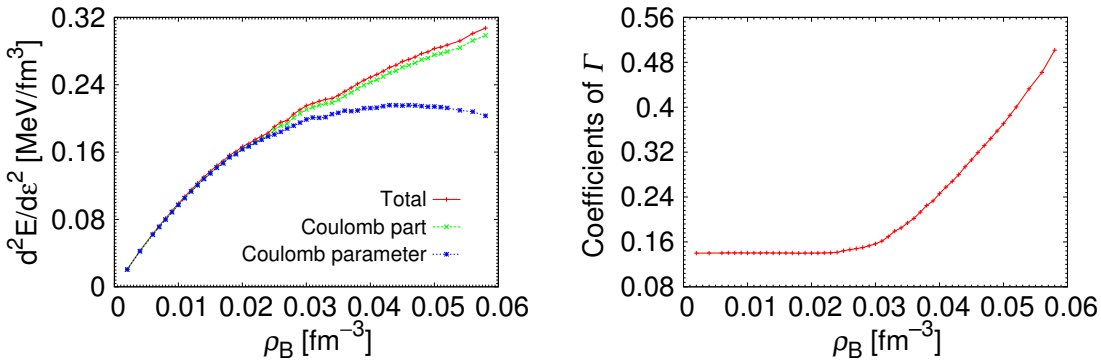

Figure 3.19: (a) Density dependence of shear moduli in the deformation D_1 obtained by semi-full calculation. Red line indicate the shear moduli derived from the total energy change. Green line those derived from the Coulomb energy change. Blue line is the fitted line using Coulomb parameter Γ with one coefficient converged in right figure.
(b) The coefficient of Coulomb parameter Γ

that of the Coulomb energy and green one indicates the fitted-line by Coulomb parameter defined as Eq.(3.19),

$$\Gamma = \frac{n(Ze)^2}{R_{\rm latt}}. \tag{3.19}$$

If we can treat the nuclei as point particle and the effect of nuclear matter such as dripped neutron is negligible, the energy change in deformation would come from only the change in Coulomb energy. Therefore, the fundamental unit of energy change could be represented by Eq.(3.19) with one coefficient.

In semi-full calculation, proton fraction and baryon density are conserved among all deformations. Then, the bulk energy term of nuclear matter do not change in deformation. The surface energy change could be negligible because of the small value of Coulomb energy change. Therefore, the red (solid) and green (with cross) line overlap each other in panel (a) of Fig. 3.19. The coefficient of Coulomb parameter is shown in panel (b) of Fig. 3.19.

In lower density region $\rho_{\rm B} < 0.03{\rm fm}^{-3}$, the coefficients Γ is converged around 0.147. Then, in this region, the assumptions applied in previous studies are proper as in our calculation. Comparing the previous study by Ogata *et al.*, the coefficient of Coulomb parameter is reduced by about 22%. Horowitz *et al.* included the effect of screening effect of slightly polarized electron around nuclei using Yukawa potential. In their calculation, the screening effect reduces the coefficient of Γ by about 10% [88,89]. This difference might come from the treatment of the Coulomb energy. From the agreement of Coulomb parameter represented by one parameter, the effect of finite size of nuclei and nuclear matter might be negligible. However, Horowitz *et al.* estimate the Coulomb energy of charged point particles. On the other hand, in our framework, the finite volume of nuclei and the screening effect of electron are treated consistently. Including these effects, the reduction in the value of coefficient of Γ become larger than that of previous study.

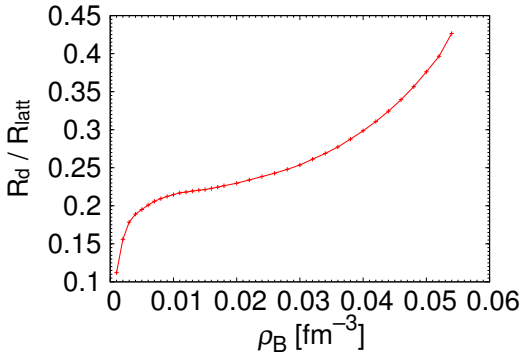

Figure 3.20: Ration of radii of proton density distribution and lattice constant

In the density region of $\rho_{\rm B} > 0.03{\rm fm}^{-3}$, we could not estimate the shear modulus by Coulomb parameter with one coefficient. This means that the treatment of nuclei as point particle is no longer feasible. We show the ratio of radii of proton density distribution and lattice constant. In the density region of $\rho_{\rm B} < 0.03{\rm fm}^{-3}$, the ratio is less than 0.2. Nuclei are separated large enough and feel each other as point particle. However, in the density region of $\rho_{\rm B} > 0.03{\rm fm}^{-3}$, the ratio increase drastically due to the decrease of lattice constant and

increase of nuclei radii. Moreover, in deformation, the nuclei slightly deformed along with the changed primitive lattice vectors. In association with these effects, the change of coulomb energy from the case of $\epsilon = 0$ might be larger than that in $\rho_{\rm B} < 0.03{\rm fm}^{-3}$.

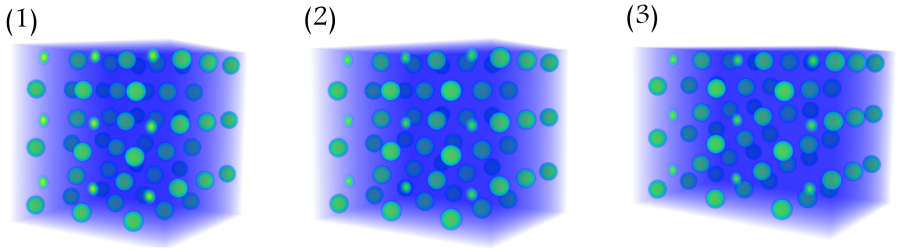

Figure 3.21: (a) Proton density distributions in several ϵ value of distorted boundary condition, $\epsilon = 0, 0.05, 0.1$ for the deformation of D_4 for (1), (2), (3) respectively.

For the deformation of D_4, D_5, D_6, we can treat these deformations by the expansion of the each grid widths as follow,

$$D_4 \quad : dr'_x = \left(1 + \epsilon + \frac{3}{4}\epsilon^2\right) dr_x, \quad dr'_y = \left(1 - \frac{\epsilon}{2}\right) dr_y, \quad dr'_z = \left(1 - \frac{\epsilon}{2}\right) dr_z \quad (3.20)$$

$$D_5 \quad : dr'_x = \left(1 - \frac{\epsilon}{2}\right) dr_x, \quad dr'_y = \left(1 + \epsilon + \frac{3}{4}\epsilon^2\right) dr_y, \quad dr'_z = \left(1 - \frac{\epsilon}{2}\right) dr_z \quad (3.21)$$

$$D_6 \quad : dr'_x = \left(1 - \frac{\epsilon}{2}\right) dr_x, \quad dr'_y = \left(1 - \frac{\epsilon}{2}\right) dr_y, \quad dr'_z = \left(1 + \epsilon + \frac{3}{4}\epsilon^2\right) dr_z \quad (3.22)$$

We show three example of proton density distribution of ground state in "usual" boundary condition for three value of $\epsilon = 0, 0.05, 0.1$ in the deformation of D_4 in Fig. 3.21. While the cubic lattice of droplets change to rectangular solid, the nuclei move along with the deformation keeping the shape of themselves as sphere.

We show the shear moduli of D_4 deformation by semi-full calculation in Fig. 3.22. Red line indicate the seconds derivative of the total energy by ϵ, blue one indicates that of the Coulomb energy and green one indicates the fitted-line by Coulomb parameter Γ. As in the case of D_1, D_2, D_3, the shear modulus is substantially described by Coulomb parameter with one coefficient parameter as about 0.014 in the density region $\rho_{\rm B} < 0.03{\rm fm}^{-3}$, and the coefficient of Γ is no more constant in higher density region. Since the same initial conditions for $\epsilon = 0$ are used with D_1, D_2, D_3, the energy change in deformation commence to be affected by the finite volume of nuclei.

From the above semi-full calculations, the angle averaged shear modulus is,

$$\begin{aligned}
\mu_{\rm eff} &= (2b_{11} + 3c_{44})/5 \\
&= \left(\frac{2}{3} f_1 + 3 f_4\right)/5 \\
&= \left(\frac{2}{3} \times 0.014 \frac{n(Ze)^2}{R_{\rm latt}} + 3 \times 0.147 \frac{n(Ze)^2}{R_{\rm latt}}\right)/5 \\
&\approx 0.0901 \times \frac{(Ze)^2}{R_{\rm latt}}.
\end{aligned}$$

(a) (b)

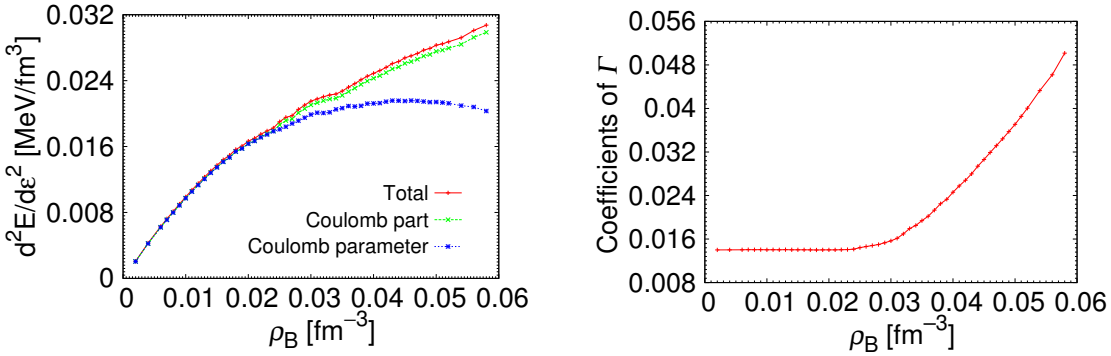

Figure 3.22: (a) Density dependence of shear moduli in the deformation D_4 obtained by semi-full calculation. Red line indicate the shear moduli derived from the total energy change. Green line those derived from the Coulomb energy change. Blue line is the fitted line using Coulomb parameter Γ with one coefficient converged in right figure.
(b) The coefficient of Coulomb parameter Γ

Next, we have performed the full calculation in which we relax all of meson fields, Coulomb potential and the density distributions of fermions under the beta-equilibrium. Since the time scale in the deformation caused by star oscillation (10^{-4} s order) is much larger than that in interaction of hadronic matter (10^{-23} s) and interaction of electrons in atom (10^{-18} s), we could consider that the deformed neutron-star crust matter may be in ground state. Then, for each deformation, the system is relaxed to get the ground state in "deformed" periodic boundary condition and the proton fraction is no more constant.

As with the semi-full calculations, we show the shear modulus in deformation D_4 for Fig. 3.23 (a) and D_1 for Fig. 3.23 (b). Red line indicate the second derivative of the total energy by ϵ, blue one indicates that of the Coulomb energy and green one indicates the fitted-line by Coulomb parameter Γ.

In low-density region $\rho_B < 0.03\text{fm}^{-3}$, while the shear moduli derived from the Coulomb energy is represented by Coulomb parameter with one coefficient parameter, those derived from the total energy is slightly different. Macroscopically, the energy changes of the Coulomb part in deformation is largely determined by the positions of each nuclei in as much as the distances between each nuclei are separated far enough and the drastic change do not occur in the nuclei. Since the same initial condition are applied with the semi-full calculations, any change do not occur in this density region for the distance. Although the proton fraction is no more constant in deformation, the proton number in nuclei could be considered as constant because of the small change of proton number-fraction. Then, the Coulomb parameter is valid to evaluate the shear modulus of Coulomb part. In semi-full calculations, since the proton fraction is constant in deformation, the shear modulus of total energy is almost same as that of Coulomb part. Although the effects of change of proton fraction to the proton number in nuclei is minuscule, we cannot exclude them from the total energy part of nuclear matter. The effective mass of nucleon slightly change while that is almost same in the semi-full calculation. σ, ω, ρ meson fields are changed by not only the deformation but also the small change of proton fraction brought about the beta-equilibrium condition. Therefore,

(a) (b)

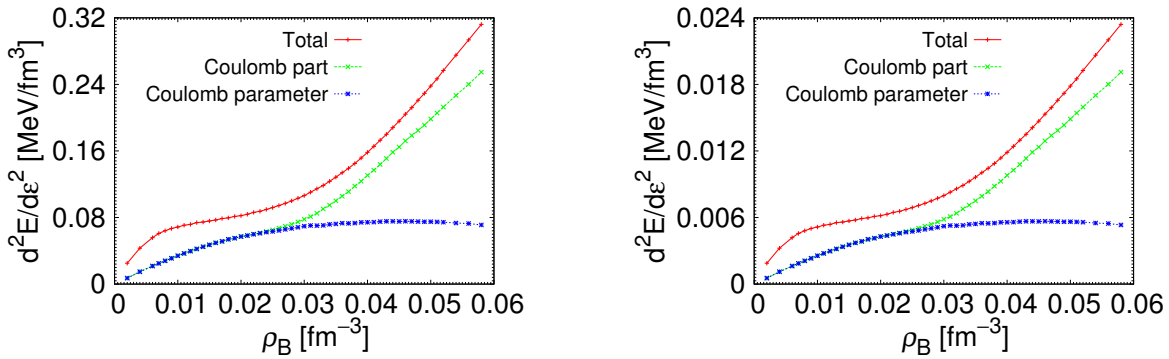

Figure 3.23: (a) Density dependence of shear moduli in the deformation D_1 obtained by full calculation. (b) Density dependence of shear moduli in the deformation D_4 obtained by full calculation. Red line indicate the shear moduli derived from the total energy change. Green line those derived from the Coulomb energy change. Blue line is the fitted line using Coulomb parameter Γ with one coefficient converged in right figure.

the shear modulus of total energy is slightly different from that of Coulomb part due to the addition of these effects. Furthermore, since these effects do not have strong relation with Coulomb energy, the shear modulus of total energy is no more represented by Coulomb parameter with one coefficient parameter even in low-density region $\rho_{\rm B} < 0.03{\rm fm}^{-3}$.

3.4 Expansion to the high density region in neutron star with kaon condensation

In this section, we explore the high-density nuclear matter in beta-equilibrium, which correspond to in the border of outer and inner core region of neutron stars.

In low-density region, the main components of nuclear matter are proton, neutron and electron. Nucleons are composed by three basic quarks and called as baryon with strong interaction. For example, proton is expressed by [uud], neutron is [udd] using up quark (u) and down quark (d). On the other hand, as a same category of nucleon, hyperon have strange quark expressed by "s" besides u and d-quark. s-quark have a larger mass than u and d-quark, and "strangeness" is introduced as a new quantum number. The strangeness quantum number is conserved in the reaction through the strong interaction, but changed in the reaction through the weak interaction. The name of "strangeness" is derived from such specific features. For example of hyperon, there exist Λ (1116) composed by [uds], Σ^- (1197) [dds] and Ξ^- (1321) [dss]. The number in square bracket express the mass of these particles in the unit of MeV. Comparing with the mass of nucleon 940 MeV, hyperons have larger masses. Then, hyperon do not appear in normal nuclei. However, under the highly compressed condition such as neutron star, since, in the same volume, more nucleons are compressed rather than in the normal nuclei, nucleons in the Fermi energy have larger single-particle energy rather in the normal nuclei by the nature of fermion. Then, if the one-particle energy of nucleon is larger than the energy difference between nucleon and hyperon, the appearance

of hyperons is energetically favor and they appear through the process such as $p+e^- \to \Lambda+\nu_e$, $n+e^- \to \Sigma^- + \nu_e$, and $\Lambda + e^- \to \Xi^- + \nu_e$. By the realistic calculation considering the effects of the potential by nucleon and hyperon in nuclear matter, it is suggested that Λ and Σ^- would appear at the density region $(2-3)\rho_0$ in neutron star. The neutron star matter with hyperons is called as hyperon matter.

Thus, the strangeness with large mass appear in the high density nuclear matter. On the other hand, in addition to the hyperon, kaons appear as elementary particle with strangeness which mediates the strong interaction between hyperon and nucleon. Kaons are Nambu-Goldstone bosons accompanying the spontaneous breaking of chiral SU(3)×SU(3) symmetry and the lightest mesons with strangeness. Their effective energy is much reduced by the kaon-nucleon interaction in nuclear medium, which is dictated by chiral symmetry. For low-energy kaons, the s-wave interaction is dominant and attractive in the I = 1 channel, so that negatively charged kaons appear in the neutron-rich matter once the process $n \to p + K^-$ becomes energetically allowed. Since kaons are bosons, they cause the Bose-Einstein condensation at zero momentum. The single-particle energy of kaons is given in a model-independent way.

$$\epsilon_\pm = \sqrt{|\mathbf{p}|^2 + m_K^{*2} + ((\rho_n + 2\rho_p)/4f^2)^2} \pm (\rho_n + 2\rho_p)/4f^2 \tag{3.23}$$

where m_K^{*2} is the effective mass of kaons, $m_K^{*2} = m_K^2 - \Sigma_{KN}(\rho_n^s + \rho_p^s)/f^2$, with the KN sigma term, Σ_{KN}, and the meson decay constant, $f \equiv f_K \sim f_\pi$ Then, the threshold condition reads

$$\mu_K = \epsilon_-(\mathbf{p} = 0) = \mu_n - \mu_p = \mu_e, \tag{3.24}$$

which means the kaon distribution function diverges at $\mathbf{p} = 0$.

If kaon condensation occurs in nuclear matter, it has many implications on compact stars; one of the interesting possibilities may be the delayed collapse of a protoneutron star to a low-mass black hole due to the large softening of EOS, and another one is a fast cooling mechanism of young neutron stars due to the nucleon Urca process under background kaons. Since many studies have shown that kaon condensation is of first order, we must carefully treat the phase change. In the following we discuss the mixed phase in the phase transition in a similar way to nuclear pasta.

For a long time there existed a naive view that not all the Gibbs conditions can be satisfied in a description by the Maxwell construction, because the local charge neutrality is implicitly assumed in it. As the result of previous works, it was suggested that a broad region of kaonic pasta as a mixed phase may occur in neutron stars with various geometrical structures of the kaon condensed phase embedded in usual nuclear matter phase. However, in recent papers it was suggested that both treatments using the Gibbs conditions and the Maxwell construction are actually in agreement with each other, if one properly includes electric field effects. The bare Coulomb field is screened by rearranged charged particles. Thus if the mixed-phase exists, the density region of them should be largely limited.

The physical reason for the possibility of the mixed phases with different geometrical structures is that the charge neutrality may hold only globally rather than locally as in the Maxwell construction. Mechanically, a balance between the Coulomb force and the surface tension is responsible for the occurrence of the spatially non-uniform structures.

3.4.1 Treatment of kaon

We explore high-density nuclear matter with kaon condensation by means of RMF model as in low-density matter. Using the same model we can discuss the non-uniform structure of nuclear matter both at low- and high-density regime in an unified way. To incorporate kaons into our RMF calculation, the thermodynamic potential is modified by the term of kaons such as

$$\Omega_K = \int d^3r\{-\frac{f_K^2\theta^2}{2}\left[-m_K^{*2} + (\mu_K - V + g_{\omega K}\omega_0 + g_{\rho K}R_0)^2\right] + \frac{f_K^2(\nabla\theta)^2}{2}\} \tag{3.25}$$

where $m_K^* = m_K - g_{\sigma K}\sigma$, $\mu_K = \mu_e$ and the kaon field $K = f_K\theta/\sqrt{2}$ (f_K is the kaon decay constant). We, hereafter, neglect a rather unimportant term $\propto \sigma^2\theta^2$. We list here the modified and added ones as follow,

σ meson:

$$\nabla^2\sigma(\mathbf{r}) = m_\sigma^2\sigma(\mathbf{r}) + \frac{dU}{d\sigma} - g_{\sigma B}(\rho_p^s(\mathbf{r}) + \rho_n^s(\mathbf{r})) + 2g_{\sigma K}m_K f_K^2\theta^2(\mathbf{r}) \tag{3.26}$$

ω meson:

$$\begin{aligned}\nabla^2\omega_0(\mathbf{r}) = m_\omega^2\omega_0(\mathbf{r}) - g_{\omega N}(\rho_p(\mathbf{r}) + \rho_n(\mathbf{r})) \\ - f_K^2 g_{\omega K}\theta^2(\mathbf{r})\left[\mu_K - V(\mathbf{r}) + g_{\omega K}\omega_0(\mathbf{r}) + g_{\rho K}R_0(\mathbf{r})\right]\end{aligned} \tag{3.27}$$

ρ meson:

$$\begin{aligned}\nabla^2\rho_0(\mathbf{r}) = m_\rho^2\rho_0(\mathbf{r}) - g_{\rho N}(\rho_p(\mathbf{r}) - \rho_n(\mathbf{r})) \\ - f_K^2 g_{\omega K}\theta^2(\mathbf{r})\left[\mu_K - V(\mathbf{r}) + g_{\omega K}\omega_0(\mathbf{r}) + g_{\rho K}R_0(\mathbf{r})\right]\end{aligned} \tag{3.28}$$

Kaon:

$$\nabla^2\theta(\mathbf{r}) = \left[m_K^*(\mathbf{r})^2 - (\mu_K - V(\mathbf{r}) + g_{\omega K}\omega_0(\mathbf{r}) + g_{\rho K}R_0(\mathbf{r}))^2\right]\theta(\mathbf{r}) \tag{3.29}$$

The charge density now reads

$$\rho_{\rm ch}(\mathbf{r}) = \rho_p(\mathbf{r}) - \rho_e(\mathbf{r}) - \rho_K(\mathbf{r}), \tag{3.30}$$

with the kaon contribution,

$$\rho_K(\mathbf{r}) = f_K^2\theta^2\left[\mu_K - V(\mathbf{r}) + g_{\omega K}\omega_0(\mathbf{r}) + g_{\rho K}R_0(\mathbf{r})\right]. \tag{3.31}$$

The chemical potentials of proton and neutron are described as follow:

$$\mu_n = \mu_{\rm B} = \sqrt{k_{F_n}(\mathbf{r})^2 + m_N(\mathbf{r})^2} + g_{\omega N}\omega_0 - g_{\rho N}R_0(\mathbf{r}), \tag{3.32}$$

$$\mu_p = \mu_{\rm B} - \mu_e = \sqrt{k_{F_p}(\mathbf{r})^2 + m_N(\mathbf{r})^2} + g_{\omega N}\omega_0 + g_{\rho N}R_0(\mathbf{r}) - V_{\rm Coul}(\mathbf{r}). \tag{3.33}$$

The last two equations are the standard relations between the local nucleon densities and chemical potentials. We have assumed that the system is in the chemical equilibrium in respect to the weak, electromagnetic, and strong interactions and we introduced the baryon chemical potential $\mu_{\rm B} = \mu_n$ and the charge chemical potential, i.e., the electron chemical potential, μ_e, according to the corresponding conserved charges. Under the same assumption $\mu_K = \mu_e$.

3.4.2 Parameter set of kaon part

Additional parameters concerning kaons are presented in Table. 3.10. By a lattice QCD calculation, the kaon-nucleon sigma term Σ_{KN} is estimated as 300–400 MeV. Using the above values and the relation

$$\frac{g_{\sigma K} g_{\sigma N}}{m_\sigma^2} = \frac{\Sigma_{KN}}{2 m_K f_K^2}, \tag{3.34}$$

$g_{\sigma K}$ can be 0.85–1.31. On the other hand, the parameter $g_{\sigma K}$ enters the value of the K^- optical potential U_K defined by $U_K = g_{\sigma K}\sigma + g_{\omega K}\omega_0$. There have been many works trying to extract U_K at the saturation density from the data on the kaonic atoms and from calculations, but there is still a controversy about its depth. We take here a somewhat deep potential, as shown in Table. 3.10. The corresponding $g_{\sigma K}$ can be 2.209–2.519, which may be rather large compared to the lattice QCD estimation. In this thesis, the same parameter set is chosen in Ref. [55]

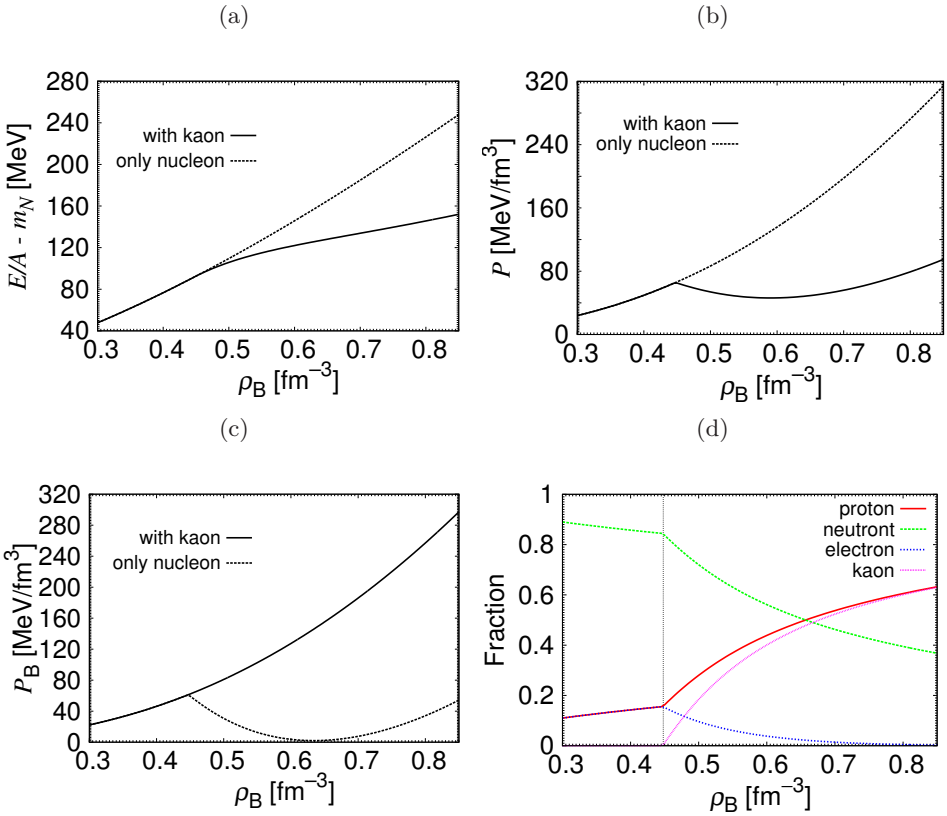

Figure 3.24: From the left, energy (a), pressure (b), baryon partial pressure(c) and fractions of each component of high density nuclear matter. In the figures of (a), (b), (c), the solid line indicate the case with kaon condensation, dotted-line the case of only nucleon. In figure (d), red line indicate the number fraction of proton, green that of neutron, blue that of electron and pink that of kaon. The vertical lines in these figures indicate the appearance of kaon at $\rho_{\rm B} = 0.45 {\rm fm}^{-3}$.

f_K [MeV]	m_K [MeV]	$g_{\omega K}$	$g_{\rho K}$	$U_K(\rho_0)$ [MeV]
93	494	$g_{\omega N}/3$	$g_{\rho N}$	-120

Table 3.10: Additional parameters used in our RMF model with kaon terms. The kaon optical potential U_K is defined by $U_K = g_{\sigma K}\sigma + g_{\omega K}\omega_0$.

Shown in Fig. 3.24 is an EOS of high density nuclear matter by using the parameter set in Table. 3.10. The solid line indicate an EOS considering the kaon condensation. As a comparison, an EOS composed by only nucleon matter is described by dotted line. As mentioned above, since the single-particle energy of nucleon become higher with increasing the density, the energy and pressure per baryon monotonously increase. On the other hand, in the case of considering the kaon condensation, the behavior of EOS completely coincide on that of nucleon, since kaons do not appear until the baryon density reaches to $\rho_{\rm B} = 0.45{\rm fm}^{-3}$. Above the density region of $\rho_{\rm B} > 0.45{\rm fm}^{-3}$, the appearance of kaon is energetically favor and decrease the energy. Although the pressure is decreased indeed, the unstable region where $dP/d\rho < 0$ also appear. This suggests the appearance of non-uniform structures.

3.4.3 Kaonic pastas

We show the equation of state of uniform high density nuclear matter considering with kaon field in Fig. 3.24. The vertical lines in these figures indicate the appearance of kaon at $\rho_{\rm B} = 0.45{\rm fm}^{-3}$. We can also see this phenomena in Fig. 3.24 (d). The lines in this figure indicate the number-fraction of each components. The red line indicates the number-fraction of proton, the green one that of neutron, the blue one that of electron and the pink one that of kaon, respectively. According to the process of $n \to p + K^-$, the fraction of neutron decrease rather rapidly while the fractions of proton and kaon increase. Since the process of $n \to p + e^-$ do not proceed, the number-fraction of electron decrease relatively.

From the behavior of pressure, the appearance of non-uniform structure could be expected indeed as in low-density nuclear matter. Then, we explored the existence of non-uniform structure in the density region $0.3{\rm fm}^{-3} < \rho_{\rm B} < 0.9{\rm fm}^{-3}$. Shown in Fig. 3.25 are all of the proton density and kaon field distributions of ground state structure. We can see that the typical pasta phases with droplets, rods, slabs, tubes, and bubbles, are reproduced by our calculation in which no assumption on the structures was used. Furthermore, these cells include several units and we can specify these lattice structures. The crystalline configuration of droplets and bubbles is bcc; rods and tubes exhibit a honeycomb configuration.

We show the density distribution of fermions, Coulomb potential and kaon field distribution at $\rho_{\rm B} = 0.5$ fm^{-3} in Fig. 3.26. Here, in the left figure, we show the proton density distribution on a sliced plane and depict the two kinds of density profiles of protons, neutrons, and electrons and the Coulomb potential and kaon field distribution in the right figure. One is along a vertical line (v) which passes through the rods; another is along a horizontal one (h). Unlike the case of low-density nuclear matter, not only neutron and electron but also the proton distribute in all space. The proton distribution is strongly correlated with the kaon distribution, which means that the Coulomb interaction is crucial. On the other hands, the neutron distribution proves to be rather flat. Electron density is spread over all space but slightly localized around the proton distribution which brings about the charge

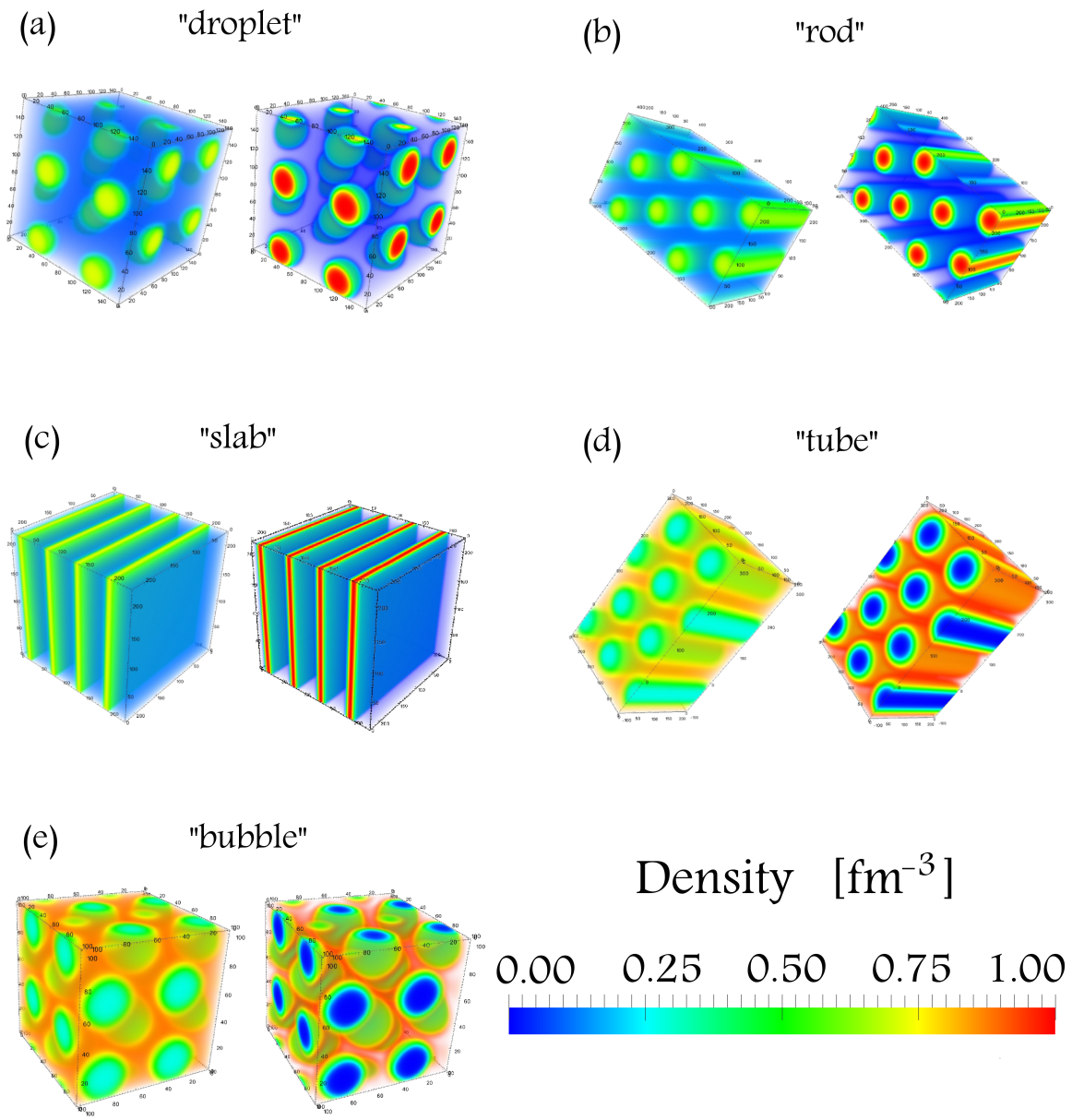

Figure 3.25: Proton density distributions and K^- meson distribution for (a) droplets at $\rho_B = 0.45$ fm^{-3}, of 76.8 fm each side, rods (honeycomb) at $\rho_B = 0.6$ fm^{-3}, of 49.96×94.8 fm^2 each side, and (c) slabs at $\rho_B = 0.66$ fm^{-3}, of 147 fm each side, and (d) tubes (honeycomb) at $\rho_B = 0.72$ fm^{-3}, of 47.0×81.4 fm^2 each side, and (e) bubbles at $\rho_B = 0.78$ fm^{-3}, of 71.2 fm each side

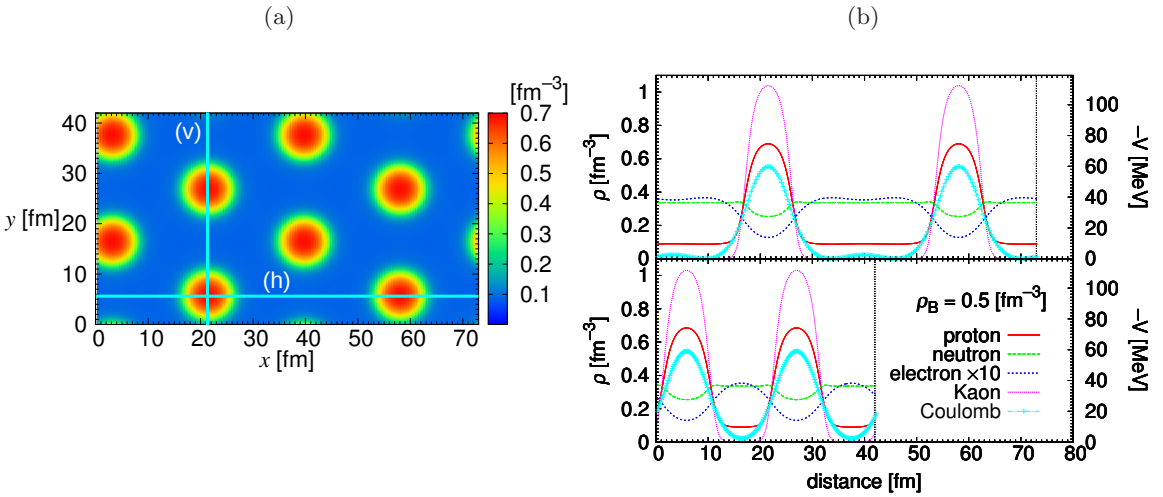

Figure 3.26: (a) Proton density distribution in the rod phase ($\rho_B = 0.5$ fm^{-3}) on the sliced plane. (b) The density distribution along a line (v)(vertical) and (h)(horizontal) in the upper figure. Red (solid line) lines indicate protons, green (dashed) line neutrons, blue (dot-dashed) lines electrons, pink (dotted) lines the kaon field and cyan lines with cross Coulomb potentials.

screening effect. Also in this figure, the advantage of the three-dimensional calculation can be seen. The proton, neutron, and electron density distributions are almost the same around kaon condensation for both the cases of (v) and (h). However, a slight difference appears in the electron density distribution and Coulomb potential. In the case of the rod phase, that point corresponds to the centroid of the triangular lattice. These points are included not on the path (v) but on the path (h). We can see these points around 9, 34, 45, 69 fm in upper figure of Fig. 3.26 (b). Between 34 and 45 fm, there are local maximum point. These points correspond to the local minimums in lower figure of Fig. 3.26 (b). Considering the large contribution of Coulomb energy due to the increase of charged components and the importance of the distinct relation between the Coulomb and surface energies for the pasta structure, we should take into account this anisotropy in a proper way in the case of applying the geometrical approximation.

In Fig. 3.27 we show the energy, total pressure, baryon partial pressure and fractions of each component as functions of density. Baryon partial pressure is given by subtracting the electron and kaon contribution from the total pressure. The appearance of non-uniform structures make nuclear matter more stable and the energy per baryon gets lower up to about 8 MeV/A compared to uniform matter. By the appearance of pasta structures, the pressure roughly monotonically increases to avoid the spinodal region which exists in uniform nuclear matter. This behavior do not corresponds to neither Maxwell construction nor Gibbs condition. However, taking into account that the pressure line represented by non-uniform matter seems to be delineated to divide into the two equal areas, this calculation is rather similar to the one given by the Maxwell construction. Droplets begin to appear for $\rho_{\rm B} > 0.41 {\rm fm}^{-3}$ smoothly decreasing the energy of the system. The mixed phase disappears for $\rho_{\rm B} > 0.786 {\rm fm}^{-3}$. We show the density region where each structures appear in Table. 3.11. The occurrence of the kaonic pasta structures results in a softening of the matter.

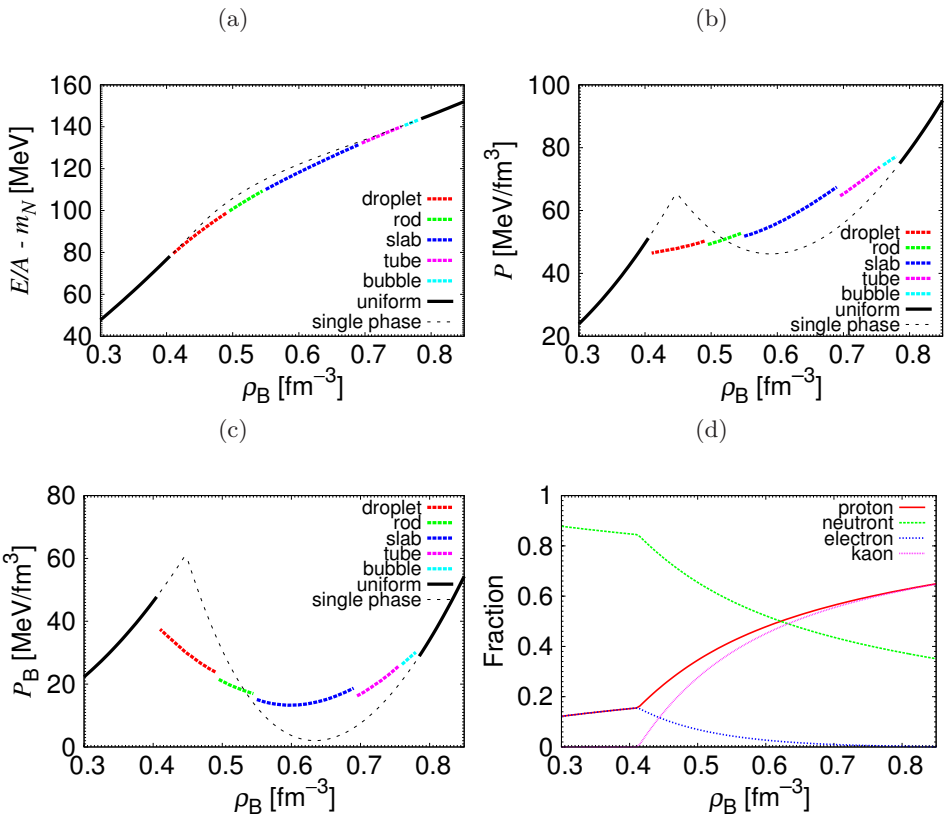

Figure 3.27: From the left, energy (a), pressure (b), baryon partial pressure (c) and number-fractions of each component (d) in high density nuclear matter. Red lines (with pluses) indicate droplets, green (with crosses) rods, blue (with stars) slabs, magenta (with open squares) tubes, cyan (with full squares) bubbles, and black uniform, respectively. All the transition densities among different crystalline configurations, including the ones indicated in the figure, have numerical ambiguity of 0.005 fm^{-3}.

Structure	droplet	rod	slab	tube	bubble
Density [fm^{-3}]	0.41 – 0.49	0.495 – 0.545	0.55 – 0.685	0.69 – 0.75	0.755 – 0.785

Table 3.11: Density region of each "pasta" structures in $0.3\mathrm{fm}^3 < \rho_B < 0.9\mathrm{fm}^{-3}$ with kaon condensation.

3.4.4 Charge screening effect of electron

The number-fraction of electron is much less than that in fixed number-fraction and beta-equilibrium cases due to the appearance of kaon. The charge screening effect of slightly polarized electron might be small and the Coulomb potential might be determined practically proton density distribution and kaon field distribution. However, since the equilibrium condition of "pasta" is determined by the balance of surface and Coulomb energy, we should confirm how much the pasta structures would be affected by the charge screening of electron. In the same way of the fixed number-fraction cases, we performed no e-screening calculation.

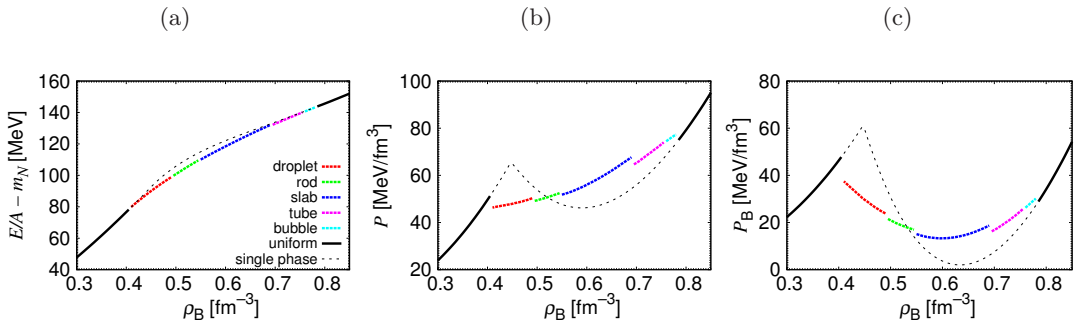

Figure 3.28: From the left, energy (a), pressure (b), and baryon partial pressure (c) in high density nuclear matter with uniformly distributed electron. Red lines (with pluses) indicate droplets, green (with crosses) rods, blue (with stars) slabs, magenta (with open squares) tubes, cyan (with full squares) bubbles, and black uniform, respectively. All the transition densities among different crystalline configurations, including the ones indicated in the figure, have numerical ambiguity of 0.005 fm^{-3}.

Structure	droplet	rod	slab	tube	bubble
Density [fm^{-3}]	0.41 – 0.49	0.495 – 0.55	0.555 – 0.68	0.685 – 0.74	0.745 – 0.775

Table 3.12: Density region of each "pasta" structures in 0.3fm^3 $< \rho_B <$ 0.9fm^{-3} with kaon condensation by no e-screening calculation.

Shown in Fig. 3.28 are the energy, pressure and baryon partial pressure of high density nuclear matter with uniformly distributed electron. The difference between full and no e-screening calculations are invisibly small. The energy from no e-screening calculation is slightly larger than that from full calculation. We show the density region of each "pasta" structures in no e-screening calculation. Comparing with Table. 3.11, any change do not occur in the region of droplet, rod and slab structures. The regions of tube and bubble structures are shorten rather than those in full calculation. Then, in no e-screening calculations, the pasta structures disappear earlier rather than full calculations.

According to the equilibrium condition of pasta structures, the most sensitive part to the treatment of Coulomb is the size of structures. We show the dependence of lattice constants in bcc lattice of droplets on the treatment of Coulomb in Table. 3.13. The lattice constant is

defined as Eq.(3.1). Since the Coulomb energy in no e-screening calculation is larger than that in full calculation, the equilibrium point by Coulomb and surface energy is shifted toward the small size region in no e-screening calculation. Then, the lattice constants in no e-screening calculation are small rather than those in full-calculation.

ρ_B (fm^{-3})	0.41	0.43	0.45	0.47
$R_{\rm latt}$ (full calculation) (fm)	25.31	20.35	18.24	17.00
$R_{\rm latt}$ (uniform electron distribution) (fm)	23.57	18.73	16.87	15.63

Table 3.13: The lattice constants in bcc lattice of droplets obtained from the full calculation and no e-screening calculation.

Chapter 4

Summary

We have numerically explored non-uniform structures and discussed the properties of low-density nuclear matter with charge neutrality and cold catalyzed matter, using the RMF model under the Thomas-Fermi approximation. Without any assumption about the geometric structure, we have carried out fully three-dimensional calculations in large cubic cells with a periodic boundary condition. Using the result of cold catalyzed matter, we explored the shear modulus of neutron star. In our calculations, to deal with the deformation in the system with periodicity, we introduce the "deformed" periodic boundary condition. For the expansion of "pasta" structures, we applied our method to the high density nuclear matter with kaon condensation such as outer core of neutron star.

In Chapter 3, first, we explored low-density nuclear matter with fixed proton number fractions of $Y_p = 0.5$, 0.3, and 0.1 (section 3.1), which may be relevant to supernova explosions and newly born protoneutron stars. The parameter set we have used gives the incompressibility of matter $K = 240$MeV and the symmetry energy coefficient of 32.5MeV at the saturation density of symmetric nuclear matter, and can well reproduce the bulk properties of finite systems (nuclei). We have observed the nuclear pasta: with increase of density the favorable structure changes from nuclear droplet, rod, slab, tube, and to bubble. Near the saturation density (normal nuclear density), nuclear pasta dissolved to uniform matter. The appearance of the pasta structures lowers the energy, while the energy differences between various geometrical structures are very small. By the appearance of such non-uniform structure, the equation of state of the system becomes significantly soft (the energy gets lower up to 15 MeV/A). In our previous study, we applied the grid width up to 0.8 fm [56]. As mentioned before, large meshes affect the density regions of each pasta structure and the EOS. By calculating at about twice the resolution, we got almost the same results but a smoother EOS. In the case of $Y_p = 0.5$, the system sometimes settled on the local minimum in the way of searching for the ground state structure. In these points, some exotic structures appeared. At finite temperatures, these structures might contribute to the Boltzmann ensemble. Assuming the electron density distribution is uniform, we explore the charge screening effect of electron. The EOS as a whole shows almost no dependence on the treatments of the Coulomb interaction. Nevertheless, the appearance density of each structure especially for tube and bubbles are different.

Second, we extended our calculations to cold catalyzed matter which corresponds to the

neutron-star crust in section 3.2. In this case, with and increase of density, which ranges from well below to half of the normal nuclear density, we have observed that the ground state of matter shows two types of pasta structures, droplets and rods. For the crystalline configuration of droplets, near the transition density to rod, the fcc lattice is more favorable than the bcc lattice, which is different from the results of previous studies. We have discussed some reasons for the difference, but more elaborate studies are needed to clarify it. We found that the ground state of low-density nuclear matter changes its crystalline configuration from a bcc to an fcc lattice near half the normal nuclear density within the RMF model. This conclusion arises from including the smooth surface of nuclei and a self-consistent calculation of the Coulomb interaction. There are, however, several other forms of lattice structures (e.g., hexagonal closest packing and tetrahedral). The hexagonal lattice has the same filling factor as the fcc one. There are many possibilities, but there is no specific interpretation for the crystalline configuration in the ground state.

Third is the estimation of realistic shear modulus of neutron star crust in section 3.3. In previous studies, shear modulus of neutron star crust matter is obtained by one-component plasma model and molecular dynamics simulations. These calculations regard the role of nuclei as charged point particles and do not take into account the role of neutron. By using the three-dimensional data of catalyzed nuclear matter obtained in section 3.2, we can treat the nuclei with finite volume under the beta-equilibrium condition. These are the advantages in our calculation. We introduced "deformed" boundary condition to treat the deformation in the system with periodicity. To estimate the shear modulus, we performed two type calculations. One is the semi-full calculation in which all of the equations of motion of meson field and Poisson equation are solved in deformed boundary condition under the preservation of density distribution of proton and neutron. In this calculation, the forces between nucleons and Coulomb potential are obtained with finite volume of nuclei. According to the treatment of gauge invariance in Coulomb potential, we can treat the screening effect of slightly polarized electron. But, the beta-equilibrium condition is no more held. Then, we could compare with previous studies. In this calculations, the shear modulus in low-density region $\rho_{\mathrm{B}} < 0.03\mathrm{fm}^{-3}$ is about 0.09 in the unit of Coulomb parameter Γ. This value is reduced about 22% from that of Horowitz *et al.*. For the density region of $\rho_{\mathrm{B}} > 0.03\mathrm{fm}^{-3}$, we could not estimate the shear moduli in the unit of Coulomb parameter with one coefficient parameter because of the finite volume of nuclei. Another is the full calculation which include the beta-equilibrium condition. While the density distribution of proton and neutron is modified in deformed boundary condition, the shapes of nuclei is mostly conserved. Then, the shear modulus of Coulomb part can be estimated in the unit of Coulomb parameter with one coefficient parameter. However, to conserve the beta-equilibrium, the additional effects of nuclear matter appear such as the change of proton fraction. Therefore, the shear modulus derived from the total energy could not be evaluate with the unit of Coulomb parameter in all density range of $\rho_{\mathrm{B}} < 0.06 fm^{-3}$ and slightly larger than that of Coulomb part.

The last one is the expansion to the higher density region with kaon condensation in section 3.4. The reappearances of "pasta" in high density region of neutron star have been expected after the disappearance in low-density region, such as "kaonic pasta" and "quark pasta". In our framework, we can explore the high density nuclear matter by adding the component which appear in such density region to the Lagrangian. As an example, we

explored the "kaonic pasta" structures in high density nuclear matter. Searching for the density region of $3 - 5\rho_0$, we obtained the "kaonic pasta" structures in $0.41 - 0.785\text{fm}^{-3}$. As with low-density nuclear matter, with increase of density the favorable structure changes from droplet, rod, slab, tube, and to bubble. The appearance of "kaonic pasta" structures lowers the energy, while the energy differences between various geometrical structures are small. By the appearance of "kaonic pasta" structures, the equation of state of the system becomes significantly soft (the energy gets lower up to 8 MeV/A).

An important advantage of our framework is the consistent treatment of the Coulomb interaction and charged particle distribution: we have included the Coulomb potential in the thermodynamic potential in a gauge-independent way and solved the Poisson equation consistently with the charged particle densities. If we take uniform charge densities as in the bulk calculations, we overestimate the potential energy due to the neglect of the charge screening effect. In fact, we have seen the importance of the charge screening for the properties of the mixed phases; the region of the mixed phase is largely modified, and it may cause a mechanical instability of the geometrical structure in some cases. As an important consequence of the charge screening effect, the EOS becomes more or less similar to that given by the Maxwell construction which is irrelevant for multiple particle composition. Actually the electron chemical potential should be different in the absence of the Coulomb potential because of the different electron number in two phases. However, we have emphasized that charge chemical potential is only defined after the gauge fixing of the Coulomb potential, so that number densities are not solely given by the chemical potential but by the linear combination of the chemical potential and the Coulomb potential. The different strength of the Coulomb potential in two phases can give the different particle densities, which can resolve an apparent contradiction in the Maxwell construction.

So far, we have explored only nuclear matter in the ground state (zero temperature). However, for example, supernova matter should be as hot as several MeV. It is naturally expected that the pasta structure will be modified and dissolved at around the critical temperature. Our model is also applicable for not-very-high temperature by modifying the baryon momentum distribution. The structural phase diagram in density-temperature plane should be useful for the discussion of supernova explosion as QMD simulations [84].

In CLMD calculations, the value of L of nuclear matter is related to the appearance region of "pasta" structures in low-density nuclear matter. The larger the value of L is given, the narrower the pasta region is. L relate with the pressure of pure neutron matter at ρ_0. Then, although the properties of neutron crust matter is slightly different from those of pure neutron matter, the large pressure might restrict to make the proton clustering in uniform neutron crust matter. In our framework, the asymmetry of proton and neutron only depends on ρ meson. Then, the value of L is tend to large to reproduce the properties of nuclear matter and finite nuclei. Recently it have been stressed to include the scalar isovector virtual $\delta(a_0(980))$ field in hadronic effective field theories when asymmetric nuclear matter is studied. Its presence introduces in the isovector channel the structure of relativistic interactions, where a balance between a scalar (attractive) and a vector (repulsive) potential exists. The δ, and ρ mesons give rise to the corresponding attractive and repulsive potentials in the iso-vector channel. Therefore, we can reproduce the EOS of different value of L while other properties remain as these stand. Introducing the δ meson, we can examine the dependence of L on the

appearance region of “pasta” structures in low-density nuclear matter.

In this thesis, we estimated the shear modulus of neutron star crust matter. According to the definition of the strain, we restricted the deformation in small range. If the energy change against a large deformation is known, the breaking strain of neutron-star crust can be obtained. Then, this breaking strain could determine the possible size of mountains on the neutron-star crust, which may radiate gravitational waves strongly under rapid rotation. These waves may be detected by large-scale interferometers and could limit the spin frequencies of accreting stars. Furthermore, the breaking strain may be important for the “star quake” model of giant flares in magnetars.

Acknowledgement

I would like to express my gratitude to Prof. T. Maruyama and Prof. K. Yabana for patient guidance, supports and encouragements during my study. I especially would like to express my deepest appreciation to Prof. T. Tatsumi for his discussion as one of my collaborators. I am very grateful to Dr. N. Yasutake and Dr. H. Sotani for their valuable cooperation. I want to express my deep appreciation to my colleagues of Theoretical Nuclear Group in University of Tsukuba, and Hadron Physics Group in Japan Atomic Energy Agency. The numerical calculations have been performed on the supercomputer PRIMERGY BX900 of Japan Atomic Energy Agency and the computers in Theoretical Nuclear Group of University of Tsukuba. Finally but not least, I would like to extend my indebtedness to my families for their understanding, supports and encouragements throughout my study.

Appendix A

General remarks about the treatment of the mixed phases

A.1 Bulk calculation and the finite-size effects in mixed phases

Consider the mixed phase composed of two different phases denoted by I and II. Then the Gibbs conditions require the pressure balance and the equality of the chemical potentials between two phases for phase equilibrium. For a multi-component system with more than one chemical potential, as is common in neutron-star matter, we must impose the equality condition for each chemical potential in order to fulfill the condition of the physico-chemical equilibrium. More definitely, we hereafter consider the charge chemical potential ($\mu_{\rm Q}$ and the baryon-number chemical potential ($\mu_{\rm B}$) respecting two conservation laws in neutron-star matter: $\mu_{\rm Q}^{\rm I} = \mu_{\rm Q}^{\rm II}$ and $\mu_{\rm B}^{\rm I} = \mu_{\rm B}^{\rm II}$. On the other hand, the first condition is not fulfilled in the Maxwell construction, since the local charge neutrality is implicitly imposed, while only the global charge neutrality must be satisfied.

A naive application of the Gibbs conditions to the mixed phase composed of two semi-infinite matter, when one ignores the surface and Coulomb interaction, demonstrates a broad region of the structured mixed phase (SMP). However the charge screening effect (caused by the non-uniform charged particle distributions) should be very important when the typical structure size is of the order of the minimal Debye screening length in the problem. It may largely affect the stability condition of the geometrical structures in the mixed phases.

We shall see that the Debye screening effects greatly modify the mechanical stability of SMP, and consequently largely limit the density region of the mixed phase. In the absence of SMP we effectively recover the picture of phase equilibrium given by the Maxwell construction where two bulk phases are separated without spoiling the Gibbs conditions.

Consider SMP consisting of two phases I and II, where we assume spherical droplets of phase I with a radius R to be embedded in the matter of phase II and two phases are clearly separated by sharp boundaries. We divide the whole space into the equivalent Wigner-Seitz cells with a radius R_W. The volume of the cell is $V_W = 4\pi R_W^3/3$ and that of the droplet is $V = 4\pi R^3/3$.

A bulk calculation proceeds as follows. First, consider two semi-infinite matter with a

volume fraction f_V, separated by a sharp boundary. By applying the global charge-neutrality condition and the pressure balance condition under the chemical equilibrium, we can get f_V for each density. Then we use the volume fraction thus determined to describe the geometrical structure in each Wigner-Seitz cell. For a given volume fraction $f_=(R/R_W)^3$, the total energy E may be written as the sum of the volume energy E_V, the Coulomb energy E_C and the surface energy E_S,

$$E = E_V + E_C + E_S \tag{A.1}$$

We further assume, for simplicity, that baryon number ($\rho_{\rm B}^\alpha$) and charge ($\rho_{\rm ch}^\alpha$) densities are uniform in each phase α, α= I, II as in semi-infinite matter. Then, E_V can be written as $E_V/V_W = f_V\epsilon^{\rm I}(\rho_{\rm B}^{\rm I}) + (1-f_V)\epsilon^{\rm II}(\rho_{\rm B}^{\rm II})$ in terms of the energy densities ϵ^α, α= I, II. The surface energy E_S may be represented as $E_S/V_W = f_V \times 3\tau/R$ in terms of the surface tension τ. The Coulomb energy E_C is given by

$$E_C/V_W = f_V \times \frac{16\pi^2}{15}\left(\rho_{\rm ch}^{\rm I} - \rho_{\rm ch}^{\rm II}\right)^2 R^2. \tag{A.2}$$

The optimal value of R, which we call R_D, is determined by the minimum condition,

$$\left.\frac{\partial\left(E/V_W\right)}{\partial R}\right|_{R=R_D}, \tag{A.3}$$

for a given f_V. Since E_V does not depend on R, we can always find a minimum as a result of the competition between the Coulomb and the surface energies, satisfying the well-known relation, $E_S = 2E_C$. However, such bulk calculations have been proved to be too crude for the discussions of SMP. Instead, a careful consideration of the interface of two phases is required. As a defect of the bulk calculations they ignore the finite-size effects. In particular, they have the inconsistent treatment of the Coulomb potential; they do not use the Poisson equation, so that the charge density profiles are assumed ab initio to be uniform and the Coulomb potential is assumed to be $1/r$. If one properly solves the Poisson equation, one should have the screening effect as a result of the rearrangement of the charge-density distribution. Hence, the radius R_D should be not too large compared with the Debye screening length λ_D,

$$\lambda_D^{-2} = \sum_i \left(\lambda_D^i\right)^{-2}, \tag{A.4}$$

$$1/\lambda_D^{-2} = 4\pi\frac{\partial\rho_{\rm Q}}{\partial\mu_i}, \tag{A.5}$$

in order the above treatment to be justified, the suffix i runs over the particle species. Otherwise, the Coulomb energy is reduced by the charge screening effect, which should lead to a mechanical instability of SMP in some cases.

A.2 Chemical potential and density distribution

In general, particles tend to move from a higher chemical potential to a lower one. A simple example is a system of dilute molecules diffusing in a homogeneous environment. Inthis system, the molecules tend to move from areas with high concentration to low concentration,

until the concentration is the same everywhere. Invoking this idea of chemical potential, we introduce a local chemical potential as a criterion of convergence to search the ground state. In this Appendix, we first verify the relation between the ground state and uniform distribution of the local chemical potential. Then, the numerical procedures concerning the local chemical potential are explained. We start by defining a local chemical potential as

$$\mu(r) = \frac{d\epsilon(r)}{d\rho(r)}, \tag{A.6}$$

where $\rho(r)$ and $\epsilon(r)$ denote the density and energy density, respectively. Let us consider an exchange of material between two small-volume components ΔV at r_1 and r_2 conserving the total amount of material as

$$\begin{aligned} \Delta\rho(r_1)\Delta V &= -\Delta\rho(r_2)\Delta V & \text{(A.7)} \\ &\equiv -\Delta\rho\Delta V. & \text{(A.8)} \end{aligned}$$

Then, the change of total energy is described as

$$\begin{aligned} \Delta E &= [\Delta\epsilon(r_1) + \Delta\epsilon(r_2)]\,\Delta V & \text{(A.9)} \\ &= \left(\frac{d\epsilon(r_1)}{d\rho(r_1)}\Delta\rho(r_1) + \frac{d\epsilon(r_2)}{d\rho(r_2)}\Delta\rho(r_2)\right)\Delta V & \text{(A.10)} \\ &= [\mu(r_1)\Delta\rho(r_1) + \mu(r_2)\Delta\rho(r_2)]\,\Delta V & \text{(A.11)} \\ &= [\mu(r_1) - \mu(r_2)]\,\Delta\rho\Delta V & \text{(A.12)} \end{aligned}$$

If the system is in its ground state, the energy should be stationary against any small density change $\Delta\rho$,

$$\frac{\Delta E}{\Delta\rho\Delta V} = 0, \tag{A.13}$$

which reads

$$\mu(r_1) = \mu(r_2) \tag{A.14}$$

From the above discussion, it is clear that uniform local chemical potential reflects that the system is in its ground state.

Next, we show the numerical procedure to get the ground state with the local chemical potential and avoid metastable states. Giving the average baryon-number density ρ_B, initial density distributions of fermions are randomly prepared on each grid point. Then proper density distributions and the meson mean-fields are searched for. We introduce the local chemical potentials $\mu_a(\mathbf{r})$ $(a = p, n, e)$ to obtain the density distributions of baryons and electrons. The equilibrium state is eventually determined so that the chemical potentials are independent of the position. An exception is the region with no particle density, where the chemical potential of that particle can be higher [see Fig. A.1(a) for more explanation]. Note that if the local density is zero, Eq. (A.10) does not apply and there is no contradiction between this explanation and the present paragraph. We repeat the following procedures to attain uniformity of the chemical potentials. A chemical potential $\mu_i(\mathbf{r})$ of a baryon $i = p, n$ on a grid point $\mathbf{r}$ is compared with those on the six neighboring grids $\mathbf{r}' = \mathbf{r} + d\mathbf{r}$, $(d\mathbf{r} = \pm d\mathbf{x}, \pm d\mathbf{y}, \pm d\mathbf{z})$. If the chemical potential at the point under consideration is larger

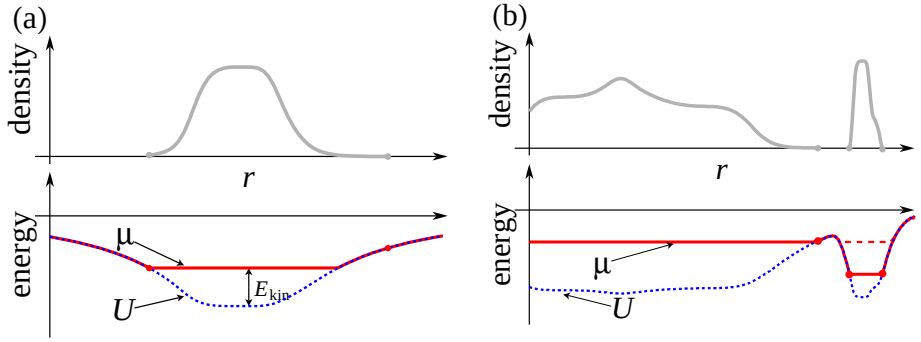

Figure A.1: (a) Schematic figure of density distribution and the chemical potential with a constant mass subtracted. In the region with zero density, where the kinetic energy is zero, the chemical potential $\mu(\mathbf{r})$ is identical to the potential $U(\mathbf{r})$, while the chemical potential in the region with finite particle density is constant.
(b) Schematic figure of nonuniform matter with an isolated matter region, where the chemical potential is different from that of the global one. By using the procedure to adjust densities between only the neighboring grids, such unphysical regions of isolated matter may appear.

than that of another $\mu_i(\mathbf{r}) > \mu_i(\mathbf{r}')$, some part of the density will be transferred to the other grid point. This adjustment of the density distribution is simultaneously done on all the grid points. In addition to the above process, we adjust the particle densities between distant grid points chosen randomly in order to eliminate regions with different μ_i which can happen to isolated matter regions as Fig. A.1(b). The meson mean-fields and the Coulomb potential are obtained by solving the equations of motion of mesons using the baryon density distributions $\rho_i(\mathbf{r})$ $(i = p, n)$ and the charge density distribution $\rho_p(\mathbf{r}) - \rho_e(\mathbf{r})$. The electron density $\rho_e(\mathbf{r})$ is directly calculated from the Coulomb potential $V_{\rm Coul}(\mathbf{r})$ and the electron chemical potential μ_e as $\rho_e(\mathbf{r}) = (\mu_e - V_{\rm Coul})^3/(3\pi^2)$. Global charge neutrality is then achieved by adjusting μ_e. The above processes are repeated many times until we get convergence.

A.3 Gauge invariance and the meaning of chemical potentials

When we use the idea of the density functional theory, the thermodynamic potential is given as a functional of the particle densities $\rho_i(\mathbf{r})$,

$$\Omega(\rho_i(\mathbf{r})) = \int d^3r \epsilon_{\rm kin+str}(\rho_i(\mathbf{r})) + E_V - \sum_i \mu_i \int d^3r \rho_i(\mathbf{r}), \tag{A.15}$$

where μ_i are the chemical potentials and $\epsilon_{\rm kin+str}$ stands for the contributions of the kinetic energy and the strong interaction energy. The Coulomb interaction energy E_V is also expressed in terms of particle densities,

$$E_V = \frac{1}{2} \sum_{i,j} \int d^3r d^3r' \frac{Q_i \rho_i(\mathbf{r}) Q_j \rho_j(\mathbf{r}')}{|\mathbf{r} - \mathbf{r}'|}, \tag{A.16}$$

with Q_i being the particle charge ($Q = -e < 0$ for the electron). Then the chemical potentials are given as

$$\mu_i = \frac{\partial \epsilon_{\rm kin+str}}{\partial \rho_i} - N_i^{\rm ch} V(\mathbf{r}), \qquad N_i^{\rm ch} = Q_i/e, \tag{A.17}$$

with the electron potentail $V(\mathbf{r})$:

$$V(\mathbf{r}) = -\sum_i \int d^3r' \frac{eQ_i\rho_i(\mathbf{r}')}{|\mathbf{r}-\mathbf{r}'|} \tag{A.18}$$

generated by the particle distributions.

We must keep the gauge invariance through the calculation: V can be arbitrarily shifted by a constant V_0, $V(\mathbf{r}) \to V(\mathbf{r}) - V_0$. Formally varying Eq. (A.17) with respect to $V(\mathbf{r})$ or μ_i we have the matrix form relation,

$$A_{ij}\frac{\partial \rho_j}{\partial V} = N_i^{ch}, \qquad A_{ij}B_{jk} = \delta_{ik}, \tag{A.19}$$

where matrices A and B are defined as

$$A_ij \equiv \frac{\delta^2 E_{\rm kin+str}}{\delta\rho_i \delta\rho_j}, \qquad B_ij \equiv \frac{\partial \rho_i}{\partial \mu_j}. \tag{A.20}$$

Eqs. (A.19) and (A.20) reproduce the gauge-invariance relation,

$$\frac{\partial \rho_i}{\partial V} = N_j^{\rm ch}\frac{\partial \rho_j}{\partial \mu_i}, \tag{A.21}$$

clearly showing that constant-shift of the chemical potential is compensated by the gauge transformation of $V(\mathbf{r})$: $\mu_i \to \mu_i + N_i^{ch}V_0$, as $V(\mathbf{r}) \to V(\mathbf{r}) - V_0$. Hence chemical potential μ_i acquires physical meaning only after fixing the gauge of $V(\mathbf{r})$.

We reconsider the relation between the Gibbs conditions and the Maxwell construction from this view point. Consider a schematic situation for simplicity, where two semi-infinite matter denoted by I and II are separated by a sharp boundary. As has been mentioned, at first glance the Maxwell construction apparently violates the Gibbs conditions, especially the equilibrium condition for the charge chemical potential $\mu_Q = (= \mu_e)$ in our context. However, correctly speaking, when we say $\mu_e^{\rm I} \neq \mu_e^{\rm II}$ within the Maxwell construction, it means nothing but the difference in the electron number density $\rho_e$in two phases, $\rho_e^{\rm I} \neq \rho_e^{\rm II}$; this is simply because $\rho_e = \mu_e^3/(3\pi^2)$, if the Coulomb potential is absent. Once the Coulomb potential is taken into account, using Eq. (A.17), ρ_e can be written as

$$\rho_e = \frac{(\mu_e - V)^3}{3\pi^2} \tag{A.22}$$

Thus we may have $\mu_e^{\rm I} = \mu_e^{\rm II}$ and $\rho_e^{\rm I} \neq \rho_e^{\rm II}$ siultaneously, with the different values of $V, V^{\rm I} \neq V^{\rm II}$. We shall see that if the Coulomb interaction is properly taken into account, the resultant EOS looks similar to that given by the Maxwell construction.

Appendix B

Elastic properties of neutron star crust

B.1 General remarks

In contrast to the liquid core, the solid crust can sustain an elastic strain. As neutron stars are relative objects, a relativistic theory of elastic media in a curved space-time should be used. Such a theory of elasticity was developed by Carter and Quintana [90]. However, for the sake of simplicity, we will restrict ourselves to the Newtonian version of the theory of elasticity [91]. This approximation can be used to obtain the elastic moduli of the crust which are the same as those appearing in the general relativistic formulation.

The state of thermodynamic equilibrium of a matter element correspond to equilibrium positions of nuclei, which will be denoted by $\mathbf{r}$. Neutron star evolution such as spin-down and accretion or some outer effects may deform the crust. In what follows, we neglect the thermal contributions to thermodynamic quantities.

A deformation of a crust element implies a displacement of the nuclei into their new positions $\mathbf{r}' = \mathbf{r} + \mathbf{u}$, where $\mathbf{u} = \mathbf{u}(\mathbf{r})$ is the displacement vector. In the continuum-medium limit, relevant for macroscopic phenomena, both $\mathbf{r}$ und $\mathbf{u}$ are treated as continuous fields. The displacement $\mathbf{u}$ produces an elastic strain and determines the deformation energy $\varepsilon_{\rm def} = \varepsilon(\mathbf{u}) - \varepsilon_0$. A uniform translation does not contribute to $\varepsilon_{\rm def}$. The deformation is described by the symmetric strain tensor as Eq.(3.5). This expression is valid as long as the displacement $\mathbf{u}$ is small and terms quadratic in $\mathbf{u}$ can be neglected.

Any deformation can be decomposed into the compression adn shear components,

$$u_{ik} = u_{ik}^{\mathbf{comp}} + u_{ik}^{\mathbf{shear}} \tag{B.1}$$

where $u_{ik}^{\mathbf{comp}} = \frac{1}{3}\delta_{ik}\nabla\cdot\mathbf{u}$ and $u_{ik}^{\mathbf{shear}} = u_{ik} - u_{ik}^{\mathbf{shear}}$. The deformation chages the volume of a matter element according to $\mathrm{d}V' = (1+\nabla\cdot\mathbf{u})\mathrm{d}V$. A pure compression, which does not affect the shape of the matter element, is described by $u_{ik} = a\delta_{ik}$. A pure shear deformation keeps the volume of the matter element constant. so that $\nabla\cdot\mathbf{u} = 0$.

To the lowest order, the deformation energy is quadratic in the deformation tensor,

$$\varepsilon_{\rm def} = \frac{1}{2}\lambda_{iklm}u_{ik}u_{lm}, \tag{B.2}$$

where summation is over repeated indices. Since $\varepsilon_{\rm def}$ is a scalar, λ_{iklm} are components of a rank-four tensor. While the total number of these components is 81, general symmetry relations reduce the maximum number of linearly independent components to 21. The number of independent elastic moduli with increasing symmetry of elastic mudeium and becomes as small as three for a bcc crystal, and two for an isotropic solid. The elastic stress tensor σ_{ik} is derived from the deformation energy via $\sigma_{ik} = \partial\varepsilon_{\rm def}/\partial u_{ik}$.

Although microspically the ground state of the neutron star crust at $\rho \leq 10^{14} g\ cm^{-3}$ correspond to bcc or fcc lattice, one usually assumes that its macroscopic properties, relevant for neutron star models, are those of an isotropic polycrystal. This simplifying assumption is made, because it is likely that te crustal matter is better approximated by a polycrystal than a monocrystal. The elastic properties of an isotropic solid are described by two elastic moduli,

$$\varepsilon_{\rm def} = \frac{1}{2}K\left(\nabla\cdot\mathbf{u}\right)^2 + \mu\left(u_{ik} - \frac{1}{3}\delta_{ik}\nabla\cdot\mathbf{u}\right)^2. \tag{B.3}$$

Here, μ is the shear modulus and K is the compression modulus. Then, the stress tensor is

$$\sigma_{ik} = \frac{\partial\varepsilon_{\rm def}}{\partial u_{ik}} = K\delta_{ik}\nabla\cdot\mathbf{u} + 2\mu\left(u_{ik} - \frac{1}{3}\delta_{ik}\nabla\cdot\mathbf{u}\right) \tag{B.4}$$

For a pure uniform compression

$$K = n_{\rm B}\frac{\partial P}{\partial n_{\rm B}} = \gamma P, \tag{B.5}$$

where γ is the adiabatic index.

B.2 Exotic nuclei

The plate phase has rotational symmetry about any axis perpendicular to the plates. Therefore, it is similar to the smectics A phase in the nomenclature of liquid crystals physics. Let the z-axis coincide with the symmetry axis of the equilibrium configulation. Only a displacement in the z-direction can be opposed by a restrong force, so that we can set $\mathbf{u} = (0, 0, u)$. Then, the deformation energy of a unit volume can be written as

$$\varepsilon_{\rm def} = \frac{1}{2}B\left[\frac{\partial u}{\partial z} - \frac{1}{2}\left(\nabla_\perp u\right)^2\right]^2 \frac{1}{2}K_1\left(\nabla_\perp^2 u\right)^2, \tag{B.6}$$

where $\nabla_\perp \equiv \left(\frac{\partial}{\partial x}, \frac{\partial}{\partial y}, 0\right)$ [70]. By considering appropriate types of deformations and calculating corresponding $\varepsilon_{\rm def}$ within the generalized Liquid drop model found [70]

$$B = 6\varepsilon_{\rm Coul}, \qquad K_1 = \frac{2}{15}r_C^2\varepsilon_{\rm Coul}\left(1 = 2\omega - 2\omega^2\right). \tag{B.7}$$

Here, $\varepsilon_{\rm Coul}$ is the Coulomb energy in equilibrium and represented as

$$\text{plates} - \text{equilibrium}: \varepsilon_{\rm def} = \frac{2\pi}{3}\left(en_{p,i}r_C\right)^2\left(1-\omega\right)^2\omega^2, \tag{B.8}$$

where r_C is the half-distance between the plates and $n_{p,i}$ is the proton number density in the nuclear matter, while ω is the volume fraction occupied by the nuclear matter. All quantities are calculated for the relaxed system.

Next, we consider the rod phase. The basic parameters describing the ground relaxed state are the rod radius r_p and the unit cell radius r_C. The number of rods per unit area perpendicular to them is $1/\pi r_C^2$. The ground state configration forms a two-dimensional triangular lattice. The Coulomb energy in equilibrium reads

$$\text{rods} - \text{equilibrium} : \varepsilon_{\text{def}} = \frac{\pi}{2} \left(e n_{p,i} r_C\right)^2 \omega^2 \left[\ln\left(\frac{1}{\omega}\right) - 1 + \omega\right]. \tag{B.9}$$

The displacements which affect the elastic energy are of the form $\mathrm{u} = (u_x, u_y, 0)$. Then

$$\begin{aligned} \varepsilon_{\text{def}} &= \frac{1}{2} B \left(\frac{\partial u_x}{\partial x} + \frac{\partial u_y}{\partial y}\right)^2 + \frac{1}{2} C \left[\left(\frac{\partial u_x}{\partial x} - \frac{\partial u_y}{\partial y}\right)^2 + \left(\frac{\partial u_x}{\partial y} + \frac{\partial u_y}{\partial x}\right)^2\right] \\ &+ \frac{1}{2} K_3 \left(\frac{\partial^2 \mathbf{u}}{\partial x^2}\right)^2 + B' \left(\frac{\partial u_x}{\partial x} + \frac{\partial u_y}{\partial y}\right) \left(\frac{\partial \mathbf{u}}{\partial z}\right)^2 + \frac{1}{2} B'' \left(\frac{\partial \mathbf{u}}{\partial z}\right)^4 \end{aligned} \tag{B.10}$$

‘ The elasticity constant B is associated with a uniform transverse compression or dilatation, while the elasticity moduli C and K_3 are associated with transverse shearing and bending of the rod lattice, respectively. The second line of Eq.(B.10) contains higher-order terms, which may be important for large longitudinal deformations.

Appendix C

Kaon interactions within the chiral model

We have used the meson exchange model (MEM) to describe kaon condensation. When we use the chiral model instead, the thermodynamic potential is given as follows:

$$\begin{aligned}
\Omega &= \Omega_B + \Omega_K + \Omega_M + \Omega_e, \\
\Omega_B &= \sum_{a=p,n} \int d^3r \left[\int_0^{f_{\mathrm{F},a}} \frac{d^3k}{4\pi^3} \sqrt{m_N^{*2} + k^2} - \rho_a \nu_a \right], \\
\Omega_K &= \int d^3r \left[-f^2(\cos\theta - 1)(m_K{*}2 - 2(\mu - V)X_0) - \frac{1}{2}(\mu - V)^2 f - 2\sin^2\theta + \frac{f^2}{2}(\nabla\theta)^2 \right], \\
\Omega_M &= \int d^3r \left[\frac{1}{2}(\nabla\sigma)^2 + \frac{1}{2}m_\sigma^2\sigma^2 + U(\sigma) - \frac{1}{2}(\nabla\omega_0)^2 + \frac{1}{2}m_{\omega_0}^2\omega_0^2 - \frac{1}{2}(\nabla R_0)^2 + \frac{1}{2}m_\rho^2 R_0^2 \right], \\
\Omega_e &= \int d^3r \left[-\frac{1}{8\pi e^2}(\nabla V)^2 - \frac{(V-\mu)^4}{12\pi^2} \right], \qquad \text{(C.1)}
\end{aligned}$$

where the kaon field is defined as $K = \frac{f}{\sqrt{2}}\sin\theta$ and $X_0 = g_{\omega K}\omega_0 + g_{\rho K}R_0$, $\mu_p + V = \nu_p + g_{\omega N}\omega_0 + g_{\rho N}R_0$, $\mu_n = \nu_n + g_{\omega N}\omega_0 - g_{\rho N}R_0$, $m_K^* = m_K^2 - 2g_{\sigma K}m_K\sigma$, $m_N^* = m_N - g_{\sigma N}\sigma$. Then the equation of motion can be eqsily written down,

$$\begin{aligned}
-\nabla^2\sigma + m_\sigma^2\sigma &= -\frac{dU}{d\sigma} + g_{\sigma B}(\rho_n^s\rho_p^s) - 2g_{\sigma K}m_K f^2(\cos\theta - 1), \\
-\nabla^2\omega_0 + m_{\omega_0}^2\omega_0 &= g_{\omega N}(\rho_n + \rho_p) + 2f^2 f_{\omega K}(\cos\theta - 1)(\mu - V), \\
-\nabla^2 R_0 + m_\rho - 2R_0 &= g_{\rho N}(\rho_p - \rho_n) + 2f^2 g_{\rho K}(\cos\theta - 1)(\mu - V), \\
\nabla^2 V &= 4\pi e^2 \rho^{\mathrm{ch}}, \\
\nabla^2\theta &= \sin\theta \left[m_K^{*2} - 2(\mu - V)X_0 - (\mu - V)^2\cos\theta \right], \qquad \text{(C.2)}
\end{aligned}$$

where $\rho^{\mathrm{ch}} = \left[\rho_p - \rho_k - \frac{(\mu-V)^3}{3\pi-2} \right]$, $\rho_K = (\mu - V)f^2\sin^2\theta + 2f^2(\cos\theta - 1)X_0$. We can see how the thermodynamic potential (C.1) or the equations of motion (C.2) can recover the previous

formulae used in the studies of kaon condensation in uniform matter. The K-N interaction terms are easily extracted from Eq. (C.2). Discarding V, the kaon source terms for the mean-fields σ, ω, ρ and the nonlinear potential for σ, $U(\sigma)$, we have $\sigma = \frac{g_{\sigma N}(\rho_n^s+\rho_p^s)}{m_\sigma^2}, omega_0 = \frac{g_{\omega N}(\rho_n+\rho_p)}{m_\omega^2}, R_0 = \frac{g_{\rho N}(\rho_p-\rho_n)}{m_\rho^2}$, amd $X_0 = \frac{g_{\omega N}g_{\omega K}}{m_\omega^2}(\rho_n+\rho_p) + \frac{g_{\rho N}g_{\omega K}}{m_\rho^2}(\rho_p-\rho_n)$, $m_K^{*2} = m_K^2 - 2m_K\frac{g_{\sigma N}g_{\sigma K}}{m_\sigma^2}(\rho_n^s+\rho_p^s)$, for soft kaons. If we impose the following relations among the coupling constants:

$$\begin{aligned}
\frac{g_{\sigma N}g_{\sigma K}}{m_\sigma^2} &= \frac{\Sigma_{KN}}{2m_K f^2}, \\
\frac{g_{\omega N}g_{\omega K}}{m_\omega^2} &= \frac{3}{8f^2}, \\
\frac{g_{\rho N}g_{\rho K}}{m_\rho^2} &= \frac{1}{8f^2},
\end{aligned} \tag{C.3}$$

we can recover the K-N interaction terms dictated by chiral symmetry, $X_0 = \frac{1}{4f^2}(\rho_n + 2\rho_p), m_K^{*2} = m_K^2 - \frac{\Sigma_{KN}}{f^2}(\rho_n^s+\rho_p^s)$. Thus we can derive the previous formulae for kaon condensation within the chiral model. To get MEM, we linearize Eqs. (C.1) and (C.2) with respect to θ and further add the non-linear terms, $X_0^2\theta^2$ and $\sigma^2\theta^2$, in Ω_K.

Appendix D

Confirmation of numerical simulation

D.1 Grid width

In the numerical simulation of non-uniform structures, the fineness of grid width is one of general problems. Especially, since the equilibrium structure of "pasta" is strongly related to the surface of structures, the precise representation of surface is improtant. The more accurate grid width is, the better we can get the solution. However, in three-dimensional calculation, twice fineness of grid width demand the eight times of original grid number. In the limitted computatilan resources, we should limit the maximum grid width and confirm the convergence in energy. In this section, we mention the dependence of grid width on energy.

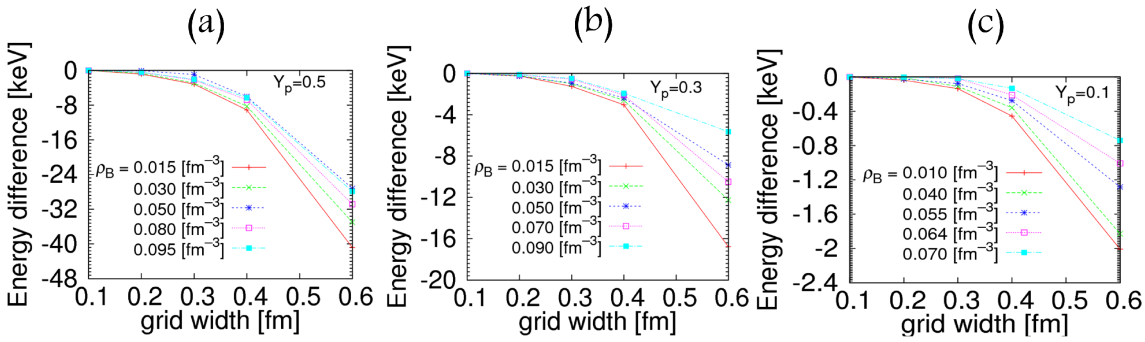

Figure D.1: Grid width dependence on energy. (a) the case of Y_p=0.5 (b) Y_p=0.3 and (c) Y_p=0.1. Red lines indicate the density which "drolet" appear. Green lines for "rod". Blue lines for "slab". Pink lines for "tube". Cyan lines for "bubble".

In Fig.D.1, we show the energy dependence on grid width in several densities. The vertical axes show the energy difference from the energy of grid width 0.1 fm. (a), (b) and (c) are the cases of $Y_p = 0.5, 0.3, 0.1$, respectively. From all figures in Fig. D.1, the energy difference increase rapidly around grid width 0.6 fm. For $Y_p = 0.5$, below the 0.4 fm, the energy

differences fall in 10 keV amoung all densities. For $Y_p = 0.3$, the energy differences fall in 4 keV and 1 keV for $Y_p = 0.1$. The density distributions of proton and nuerton rapidly change around the surfase region rather than for $Y_p = 0.3$ and 0.1. Then, the energy changes in $Y_p = 0.5$ are slightly larger than those in 0.3 and 0.1. Therefore, in this thesis, the maximum grid width is decided as 0.4 fm for all calculations.

D.2 "Deformed" boundary condition in 2D calculation

In section 3.3.1, to treat the deformation with periodicity, we introduce the "deformed" boundary condition. Althogh the outline of this boundary condition and application to obtain the shear modulus was mentioned, the validity of this boundary condition was left. In this section, applyin in two-demenstional calculations, we verify the application of "deformed" boundary condition for one-dimentional deformation.

For initial condition, we set the single lattice of rods of beta-equilibrium nuclear matter in two-dimentional plane. To treat the one-dimensional deformation, we apply the "deformed" boundary condition to this initial condition as follow,

$$F(x + L_x, y) = F(x - L_x, y) = F(x, y),$$
$$F(x, y + L_y) = F(x - \epsilon, y), \quad F(x, y - L_y) = F(x + \epsilon, y)$$

where ϵ means the strain defined in Eq.(3.5). Under the deformation, the coordinates r_i of an rod get mapped to r'_i

$$r'_x = (1 + \epsilon)r_x, \quad r'_y = r_y$$

After getting the shifted density distribution of nuclear matter, we perform the full-calculation defined under the "deformed" boundary condition in section 3.3.1.

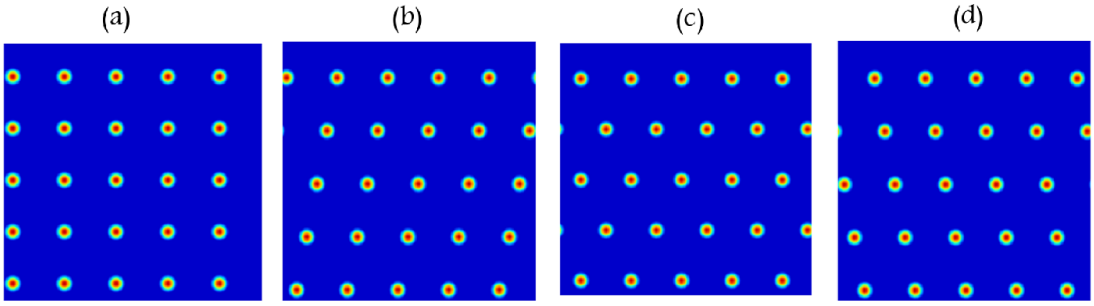

Figure D.2: Proton density distributions in the value of ϵ=0, 0.2, 0.5, 0.8 for (a), (b), (c) and (d), respectively

Shown in Fig. D.2 are the proton desity distribution in each deformation. From the left figure, the value of ϵ correspond to 0, 0.2, 0.5 and 0.8, respectively. To make the shit of rods in deformation clearly, we marked one rod as "P". We can see that the rod marked P move to right following the deformation.

The energy differences from the case of $\epsilon = 0$ are shown in Fig. D.3. From Eq.(B.3), if the system is unstable for deformation, the energy of system should decrese in accordance with

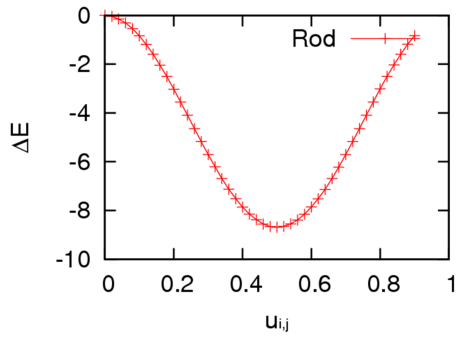

Figure D.3: Strain dependence on energy in one-demensional deformation for rod lattice.

the deformation. Then, the value of μ in Eq.(B.3) would be negative. In two-dimensional system, the honey-comb lattice is favorable energetically rather than single one. As mentioned before, in this calculation, we set the single lattice as initial condition. Therefore, the energy decrease indeed in Fig. D.3 until ϵ reach to 0.5. After $\epsilon = 0.5$, the energy deferences diminish. We can see, from the figure (c) in Fig. D.2, the crystalline structure was changed from single lattice to honye-comb like lattice. Strictly speaking, owing to the initial condition, the system could not form the honey-com lattice completely in deformation. Nevertheless, the system favor the honey-comb like lattice rather than single lattice.

The behavior of energy differences have an inversion symmetry at $\epsilon = 0.5$. The crystalline structure at $\epsilon = 0.5$ correspond to the honey-comb like lattice in "normal" periodic boundary condision. If this structure is applied as initial codition, figure (b) and (c) in Fig. D.2 would correspond to $\epsilon = -0.3$ and 0.3, respectively. While the directions of deformation are contrary to each other, the magnitude of strain is same. The energy differences from the case of $\epsilon = 0$ are also same at $\epsilon = 0.3 \text{and} -0.3$. Therefore, in two-dimensional calculation for one-direction deformation, the energy difference as a function of the deformation strain ϵ have a periodicity with period 1. If initial condition is in ground state, energy difference curve have a maximun value at ϵ=0.5.

Bibliography

[1] L. C. Gones, J. D. Walecka and V. F. Weiskopf, Ann. Phys. (New York) **3** (1958).

[2] M. A. Preston, *Physics of the Nucleus Structure* (Addison-Wesley, Reading, 1962).

[3] A. deShalit and H. Feshbach, *Theoretical Nuclear Physics* (John Wiley & Sons, New York, 1974).

[4] P. Möller, W. D. Myers, W. J. Swiatecki and J. Treiner, Atomic Data and Nuclear Data Tables **39** (1988) 225.

[5] P. Möller and J. R. Nix, Nucl. Phys. **A361** (1981) 17.

[6] J. P. Blaizot, D. Gogny and B. Grammiticos, Nucl. Phys. **A265** (1976) 315.

[7] H. Krivine, J. Treiner and O. Bohigas, Nucl. Phys. **A336** (1980) 155.

[8] N. K. Glendenning, Phys. Rev. Lett. **57** (1986) 1120.

[9] N. K. Glendenning, Phys. Rev. C **37** (1988) 2733.

[10] M. M. Sharma, W. T. Borghols, S. Brandenburg, S. Crona, A. van der Woude and M. N. Harakeh, Phys. Rev. C **38** (1988) 2562.

[11] M. Jaminon and C. Mahaux, Phys. Rev. C **40** (1989) 354.

[12] J. M. Lattimer, M. Prakash, Astrophys. J. **550**, 426 (2001)

[13] W. Baade and F. Zwicky, Phys. Rev. **45** (1934) 138.

[14] W. Baade and F. Zwicky, Phys. Rev. **46** (1934) 76.

[15] J. R. Oppenheimer and G. M. Volkoff, Phys. Rev. **55**, 374 (1939)

[16] A. Hewish, Rev. Mod. Phys. **47** (1975) 567.

[17] T. Gold, Nature **218** (1968) 731.

[18] D. C. Backer, S. R. Kulkarni and S. R. Heiles, Nature, **300**, 615 (1982)

[19] C. Thompson, Mem. Soc. Astron. Ital. **73**, 477 (2002)

[20] T. E. Strohmayer, AIP Conf. Proc. **714**, 245 (2004)

[21] R. N. Manchester, A. G. Lyne, F. Camilo, J. F. Bell, V. M. Kaspi, N. D'Amico, N. P. F. Mckey, F. Crawford, I. H. Stairs, A. Possenti, M. Kramer, D. C. Sheppard, Mon. Not. R. Astron. Soc. **328**, 17 (2001)

[22] M. A. Livingstone, V. M. Kaspi, E. V. Gotthelf and L. Kuiper, Astrophys. J. **647**, 1286 (2006)

[23] A. G. Lyne, R. S. Pritchard and F. G. Smith, Mon. Not. R. Astron. Soc. **233**, 667 (1988)

[24] J. Pons, S. Reddy, M. Prakash, J. M. Lattimer and J. A. Miralles, Astrophys. J. **513** 780 (1999).

[25] J. Pons, J. A. Miralles, M. Prakash and J. M. Lattimer, Astrophys. J. **553**, 382 (2001)

[26] D. G. Ravenhall, C. J. Pethick and J. R. Wilson, Phys. Rev. Lett. **50** 2066 (1983).

[27] T. Takatsuka and R. Tamagaki, Prog. Theor. Phys. Suppl **112** 107 (1993).

[28] S. Tsuruta and A. G. W. Cameron, Canadian J. Phys. **43** (1965) 2056.

[29] D. G. Yakovlev, C. J. Pethick, Annu. Rev. Astron. Astrophys. **42**, 169 (2004)

[30] T. Takatsuka and R. Tamagaki, Nucl. Phys. A **478** 785c (1988).

[31] K. -I. Kondo, Phys. Rev. D **82**, 065024 (2010).

[32] C. Ratti, M. A. Thaler and W. Weise, Phys. Rev. D **73**, 014019 (2006).

[33] G. Baym and G. Grinstein, Phys. Rev. D **15**, 2897 (1977).

[34] K. Fukushima, Phys. Rev. D **86**, 054002 (2012).

[35] N. Bohr and J. A. Wheeler, Phys. Rev. **56** 426 (1939).

[36] C. J. Pethick and D. G. Ravenhall, Annu. Rev. Nucl. Part. Sci. **45** 429 (1995).

[37] G. Baym, H. A. Bethe and C. J. Pethick, Nucl. Phys. **A175** (1971) 221.

[38] S. Furusawa, K. Sumiyoshi, S. Yamada, H. Suzuki, Astrophys. J. **772**, 95 (2013)

[39] M. Hashimoto, H. Seki and M. Yamada, Prog. Theor. Phys. **71**, 320 (1984).

[40] K. Oyamatsu, M. Hashimoto, M. Yamada, Prog. Theor. Phys. **72**, 373 (1984).

[41] K. Oyamatsu, Nucl. Phys. **A561**, 431 (1993).

[42] G. Watanabe, K. Iidai and K. Sato, Nucl. Phys. **A 676** 455 (2000).

[43] G. Watanabe, K. Iida and K. Sato, Nucl. Phys. **A 726** 357 (2003).

[44] H. Sonoda, G. Watanabe, K. Sato, T. Takiwaki, K. Yasuoka and T. Ebisuzaki, Phys. Rev. C **75** 042801 (2007).

[45] J. W. Negel and D. Vautherin, Nucl. Phys. **A207** (1973) 298.

[46] W. G. Newton, J. R. Stone, Phys. Rev. C **79**, 055801 (2009).

[47] H. Pais and J. R. Stone, Phys. Rev. Lett. **109** 151101 (2012).

[48] P. Magierski, A. Bulgac, P. -H. Heenen, Nucl. Phys. A **719** 217c (2003).

[49] P. Magierski, P. -H. Heenen, Phys. Rev. C **65** 045804 (2002).

[50] B. Schuetrumpf, M. A. Klatt, K. Iida, J. Maruhn, K. Mecke, P. -G. Reinhard, Phys. Rev. C **87**, 055805 (2013) .

[51] R. Ogasawara and K. Sato, Prog. Theor. Phys. **68** 222 (1982).

[52] R. D. Williams, S. E. Koonin, Nucl. Phys. **A435** 844 (1985)

[53] H. M**ü**ller and B. D. Serot, Phys. Rev. C **52**, 2072 (1995).

[54] S. S. Avancini, D. P. Menezes, M. D. Alloy, J. R. Marinelli, M. M. W. Moraes, and C. Providencia, Phys. Rev. C **78**, 015802 (2008).

[55] T. Maruyama, T. Tatsumi, D. N. Voskresensky, T. Tanigawa and S. Chiba, Phys. Rev. C **72** 015802 (2005).

[56] M. Okamoto, T. Maruyama, K. Yabana, T. Tatsumi, Phys. Lett. B **713** 284 (2012).

[57] M. Okamoto, T. Maruyama, K. Yabana, T. Tatsumi, Phys. Rev. C **88**, 025801 (2013).

[58] C. P. Lorentz, D. G. Ravenhall and C. J. Pethick, Phys. Rev. Lett. **70** 379 (1993).

[59] K. S. Cheng, C. C. Yao and Z. G. Dai, Phys. Rev. C **55** 2092 (1997).

[60] F. Douchin, P. Haensel and J. Mayer, Nucl. Phys. **A665** 419 (2000).

[61] F. Douchin and P. Haensel, Phys. Lett. B **485** 107 (2000).

[62] Y. Mochizuki, T. Izuyama and I. Tanihata, Astrophys. J. **521** 281 (1999).

[63] M. Matsuzaki, Phys. Rev. C **73** 028801 (2006).

[64] K. Nakazato, K. Iida and K. Oyamatsu, Phys. Rev. C **83** 065811 (2011).

[65] C. K. Horowitz, M. A. Pérez-García, D. K. Berry and J. Piekarewicz, Phys. Rev. C **72** 035801 (2005).

[66] M. E. Gusakov, D. G. Yakovlev, P. Haensel and O. Y. Gnedin, Astron. Astrophys. **421** 1143 (2004).

[67] F. V. de Blasio and G. Lazzari, Phys. Rev. C **52** 418 (1995).

[68] F. V. de Blasio and G. Lazzari, Phys. Lett. B **384** 1 (1996).

[69] Ø. Elgarøy, L. Engvik, E. Osnes, F. V. de Blasio, M. Hjorth-Jensen and G. Lazzari, Phys. Rev. D **54** 1848 (1996).

[70] C. J. Pethick and A. Y. Potekhin, Phys. Lett. B **427** 7 (1998).

[71] P. B. Demorest, T. Penucci, S. M. Ransom, M. S. E. Roberts and J. W. T. Hessels, Nature **467** 1081 (2010).

[72] G. Baym, E. Flowers, Nucl. Phys. A **222** 29 (1974).

[73] E. E. Kolomeitsev and D. N. Voskresensky, Nucl. Phys. A **759** 373 (2005).

[74] R. Knorren, M. Prakash, P. J. Ellis, Phys. Rev. C **52** 3470 (1995).

[75] N. K. Glendenning, Phys. Lett. B **114**, 392 (1982).

[76] N. K. Glendenning, S. A. Moszkowski, Phys. Rev. L **67**, (1991) 2414.

[77] C. Ishizuka, A. Ohnishi, K. Tsubakihara, K. Sumiyoshi S. Yamada, Jour. Phys. **G35**, (2008).

[78] K. Tsubakihara, H. Maekawa, H. Matsumiya, A. Ohnishi, Phys. Rev. C **81**, 065206 (2010).

[79] N. K. Glendenning and S. Pei , Phys. Rev. C **52**, 2250 (1995).

[80] G. F. Burgio, M. Baldo, P. K. Sahu, and H. -J. Schulze, Phys. Rev. C **66**, 025802 (2002).

[81] T. E. Strohmayer and A. L. Watts, Astrophys. J. **653**, 593 (2006).

[82] A. L. Watts, Ann. Rev. Astron. Astrophys. **50**, 609 (2012).

[83] H. Sotani, Mon. Not. Roy. Astron. Soc. **417**, L70 (2011).

[84] G. Watanabe, K. Sato, K. Yasuoka, T. Ebisuzaki, Phys. Rev. C **68** 035806 (2003).

[85] K. Oyamatsu, K. Iida, Phys. Rev. C **75** 015801 (2007).

[86] M. A. Preston, R. Bhaduri, *Structure of the Nucleus* (Addison-Wesley, Reading, MA, 1975).

[87] S. Ogata and S. Ichimaru, Phys. Rev. A **42**, 4867 (1990).

[88] C. J. Horowitz, Phys. Rev. D **81** 103001 (2010).

[89] C. J. Horowitz and K. Kadau, Phys. Rev. Lett. **102**, 191102 (2009).

[90] B. Carter and H. Quintana, Proc. R. Soc. London, Ser. A, **331**, 57 (1972).

[91] L. D. Landau and E. M. Lifshitz, *Theory of Elasticity*, Pergamon Press, Oxford, U.K. (1986).